Investigation of plasma transport across magnetic filter in low temperature plasmas using 2D-3V PIC-MCC simulations: application to negative ion sources

by

MIRAL SHAH
201621007

A Thesis Submitted in Partial Fulfilment of the Requirements for the Degree of

DOCTOR OF PHILOSOPHY
to

DHIRUBHAI AMBANI INSTITUTE OF INFORMATION AND COMMUNICATION TECHNOLOGY

February, 2021

Declaration

I hereby declare that

i) the thesis comprises of my original work towards the degree of Doctor of Philosophy at Dhirubhai Ambani Institute of Information and Communication Technology and has not been submitted elsewhere for a degree,

ii) due acknowledgment has been made in the text to all the reference material used.

Miral Shah

Certificate

This is to certify that the thesis work entitled INVESTIGATION OF PLASMA TRANSPORT ACROSS MAGNETIC FILTER IN LOW TEMPERATURE PLASMAS USING 2D-3V PIC-MCC SIMULATIONS: APPLICATION TO NEGATIVE ION SOURCES has been carried out by MIRAL SHAH for the degree of Doctor of Philosophy at *Dhirubhai Ambani Institute of Information and Communication Technology* under my supervision.

Prof. Bhaskar Chaudhury
Thesis Supervisor

Acknowledgments

First and foremost, praises and thanks to God, the Almighty, for His showers of blessings throughout my research work to complete the research successfully.

I want to express my deep and sincere gratitude to my guide, Prof. Bhaskar Chaudhury, for giving me the opportunity to do research and providing invaluable guidance throughout this research. His dynamism, vision, sincerity, and motivation have deeply inspired me. He has taught me the methodology to carry out the research and present the research works as clearly as possible. It was a great privilege and honor to work and study under his guidance. Without him, this might not be possible. Who encourages me each time when I feel low or confused. Who is always ready to correct me, guide me, discuss with me even on holidays.

I am very grateful to Distinguished scientist Dr. Mainak Bandyopadhyay, Institute of Plasma Research (IPR), for giving me continuous attention and guidance. Thank you for always being ready for fruitful discussion and suggestions. My sincere thanks also go to Dr. Arunkumar Chakraborty and ROBIN team for giving experiment data. I also like to thank my thesis committee, Prof. Arnab Ray and Prof. Sanjay Srivastav, for their encouragement, insightful comments, and challenging questions.

I would like to thank the Department of Atomic Energy, Govt. of India for the research fellowship received under the BRNS project.

I am very thankful to DA-IICT help desk staff, Rajendra Shah, Gyanesh Pandya, and Ramesh Prajapati. I also like to thank CS B-tech Students Harshil, Suddharth, Riddhesh, Mihir, Keval, Hasnain, Unnati, Paramjeet, and Anusha for helping me in the development of parallel PIC code.

With all, I never forget to thank my Ph.D. friends; Dr. Vandana Ravindran, Dr. Sarita Agrawal, Dr. Ramnaresh Vangala, Dr. Milind Padalkar, Dr. Pankaj Chaudhury, Dr. Nupur Jain, Dr. Nidhi Desai, Dr. Sujata, Dr. Archana, Dr. Prashant, Dr. Purvi Koringa, Pratik Ghosh, Pranav Verma, Purvi Patel, who makes my Ph.D. journey more interesting, and helping me whenever I need them. I also like to thank Teja Vardhan Reddy for helping me to review my thesis.

I am extremely grateful to my parents for their love, prayers, caring, and sacrifices for educating and preparing me for my future. I am very much thankful to my husband Axay, mother-in-law, and son Vrudant, for their love, understanding, prayers, and continuous support to complete this research work. Also, I express my thanks to my sisters Henari and Krishna, Drishti, my sister-in-laws Mitaldidi and Jitikshadidi for their support and valuable prayers.

Contents

Abstract

The LTP (hydrogen) based negative ion source plays an important role in the neutral beam injection system - one of the primary means of plasma heating in magnetic fusion. In this thesis, we have performed PIC-MCC based simulations of such plasmas wherein the ROBIN negative ion source (consisting of an LTP source with a magnetic filter) installed at IPR, Gandhinagar is taken as a testbed problem for the validation of the model. ROBIN has a driver, an expansion chamber, a magnetic filter, and extraction system consisting of 3 different grids. Plasma is generated in the RF driver region, and that expands in the expansion chamber before encountering the magnetic filter field. A magnetic filter is a localized magnetic field (few tens of gauss) perpendicular to the plasma flow (diffusion flux or transport) and controls the plasma flux flowing from the expansion chamber to the extraction system. As a first step, we have performed 1D-3V PIC-MCC simulations, and we observe a good qualitative match between the simulation and experimental results in terms of plasma density and electron temperature. The quantitative mismatch between the ROBIN experiment and 1D-simulation results is due to the fact that the effect of drifts and instabilities (present in real experiments) are not captured properly in the 1D model. However, even with several limitations, we find that 1D-3V PIC-MCC simulations can predict plasma behavior in such LTP experiments with acceptable accuracy.

As a second step in this direction, we have developed an in-house serial 2D-3V PIC-MCC code and also validated it with results available in the literature. However, stringent numerical constraints associated with a 2D PIC code make it computationally prohibitive on CPUs in the case of real experimental geometry (total number of particles, number of grid points and simulation time-scale). Therefore, we parallelized our 2D-3V PIC-MCC codes for shared

as well as distributed memory systems consisting of multi-core and many-core architectures (GPUs). We have also proposed a hybrid parallel scheme (OpenMP+MPI) which can be used to perform such expensive simulations on an HPC cluster with several nodes. One of the novel contribution towards the PIC-MCC code development has been made in terms of using different particle sorting strategies which significantly improved the memory access time leading to a remarkable enhancement in speedup compared to traditional strategies used for PIC-MCC implementation.

The parallel 2D-3V PIC-MCC code have been used to simulate ROBIN experiment with real physical dimensions to understand the plasma transport across magnetic filter. Most of the previous works in this area used a scaled geometry as well as relaxed the stringent numerical criteria for such simulations due to computational requirements, however we performed simulations by satisfying all the strict numerical constraints such as time step, grid spacing and PPC required for kinetic modelling of such LTP experiments. Plasma density and electron temperature profiles from our 2D-3V PIC simulations follow similar trends (qualitative as well as quantitative) as seen in experimental results. This immensely helped us to understand the role of instabilities as well as different diffusion and collisional processes, and subsequently quantifying the plasma transport accurately. Even with certain limitations present in our model, simulation results show a reasonably good match with the phase-1 ROBIN experimental results. Particularly the simulations are showing similar important patterns in plasma characteristics as seen in the experiments. Comparison of the simulation and experimental results from ROBIN gives us sufficient confidence to do further case studies for future ROBIN experiments. Several case studies have been performed to understand the role of the magnetic filter profile on plasma transport, which will help in planning future experiments by using the magnetic filter as a switching mechanism to achieve the required density and electron temperature profiles for efficient operation of negative ion source.

Various collision dependent physical phenomena, having different time scales and length scales are studied using 2D-3V PIC-MCC simulations. We have reported instabilities, observed near the filter field region. It is also observed

that the frequencies of those instabilities are close to some of the electronic and ionic collision frequencies which may create resonant phenomena in the magnetic filter region and influence the cross-field transport, and heating. From our investigations, we find that the application of a bias voltage (applied to the extraction boundary) changes the potential profile and thereby plays an important role in controlling the ion temperature near the extraction boundary. The nature of the instabilities also depend on the bias voltage. We are anticipating an ion heating due to instabilities originating in the filter field region. 2D snapshots clearly shows discrete band structure which corresponds to drifts and instabilities, and the frequencies of the instabilities are identified using Fast Fourier Transform (FFT) analysis. The instability corresponding to 10^5 Hz is identified as $E \times B$ drift instability whereas, 10^6 Hz still requires further investigation. In this study, we have shown these instabilities are one of the causes for ion heating.

Drifts and instabilities observed in our simulations may lead to double layer (DL) formation which has not been studied yet in the context of negative ion sources. This motivated us to perform detailed analysis with different magnetic field values and different bias voltages. Plasma profiles (such as potential, electron and ion temperature, and ion velocities) are studied to understand the formation of DL and its effect on plasma transport. Ion acceleration is found near both source and extraction boundaries either due to sheath, instabilities, or DL. We observe DL formation under specific conditions (magnetic field and bias voltage). Two velocities components (one due to the free ions and the other due to the trapped ions) are visible in our simulations. We found that DL depends on both the magnetic field and the difference between bias voltage and plasma potential. DL does not occur when the bias voltage is more or equal to the plasma potential. When the bias voltage is greater than plasma potential, electron sheath forms and reflects ions from the extraction boundary.

A detailed investigation of Energy Distribution Functions (EDFs) helps in interpreting the complex physics involved in such LTP problems. We have studied the temporal and spatial evolution of EDFs using our PIC-MCC code. We have observed that EEDF is Maxwellian in nature, but IEDF is

non-Maxwellian in nature. Our detailed Spatio-temporal analysis of EDFs revealed that IEDF is more sensitive to changes in the filter field and bias voltage compared to EEDF. All the past studies have focused on understanding electron transport, however, our simulations suggest that to completely understand the physics of plasma transport in such low-temperature sources, ion transport is equally important and needs to be investigated in more detail.

Efficient negative ion generation in the negative ion source is a critical step in the neutral beam injection (NBI) system of the future fusion reactor ITER. Achieving few tens of Amperes of H^- current in the negative ion source is technically challenging and needs more understanding of the physics of the plasma transport in such sources. The important contributions of this thesis such as identification of instabilities, double layer formation and understanding of EDFs in the context of negative ion sources using comprehensive kinetic simulations will further improve our understanding of physics of plasma transport and help in enhancing the efficiency of negative ion generation process in such sources. The results are also relevant for similar kinds of different LTP based applications involving magnetic field such as Hall thrusters, ECR source, end-Hall source and magnetron discharge.

List of Principal Symbols and Acronyms

Principal Symbols

m	mass of particle	m_e and m_i	electron and ion mass
n	plasma density	n_e and n_i	electron & ion plasma density
n_o	neutral density	N_D	plasma parameter
$\bigtriangledown$P	pressure gradient	$\bigtriangledown n$	density gradient
e	electron charge	ϵ_0	permittivity of free space
t	time	q	charge of particle
E	electric field	E_x and E_y	electric field in X & Y direction
B	magnetic field	B_z	magnetic field in Z direction
ϕ	potential	ρ	charge density
k	Boltzmann constant	T	temperature
T_{heat}	heating temperature	T_e and T_i	electron and ion temperature
N_{eh}	number of heated electrons	N_T	number of electrons present in the *driver* in time $t + \Delta t$
v	average velocity (in m/s)	v_x and v_y	velocities in X and Y direction
$v_\perp$	cross-field velocity	v_E	E $\times$ B drift velocity
v_D	diamagnetic drift velocity	v_B	Bohm velocity
r	position	$f(r, v, t)$	distribution function
$\vec{F}$	Lorents force	$(\frac{\delta f}{\delta t})_{colli}$	changing in distribution function f with time due to collision
V_{pp}	plasma potential	γ	scale factor
V_{bias}	Bias potential	V_{sdrop}	Voltage drop due to sheath
J_e	electron current density	P_e	electron pressure
GX	number of grids in X	NX	Number of grids in X
NY	Number of grids in Y	LX	total length of the simulation domain

Mobility & Diffusion

μ	mobitily ($\frac{e}{m\nu}$)	μ_e and μ_i	electron and ion mobility
$\mu_\perp$	cross-field mobility	D_e and D_i	electron and ion diffusion co-efficient
D	diffusion co-efficient ($\frac{kT}{m\nu}$)	$D_\perp$	cross-field diffusion
D_{Bohm}	Bohm diffusion	D_{class}	classical diffusion co-efficient
D_a	ambipolar diffusion		

Length scales:

λ_D	Debye length	R_{Le}	electron Larmor radius
R_{Li}	ion Larmor radius	r	position
ΔX	grid spacing in X	ΔY	grid spacing in Y

Time scales:

Δt	time step	τ	collision time period
ν_h	heating frequency	ω_{ce}	electron cyclotron frequency
ω_{ci}	ion cyclotron frequency	ω_p	plasma frequency
ν	collision frequency	ν_{ei}	electron-ion Coulomb collision frequency
ν_{en}	electron-neutral collision frequency	ν_{in}	ion-neutral collision frequency
h_e	electron Hall parameter	h_i	ion Hall parameter
σ_{en}	electron-neutral collision cross-section	σ_{in}	ion-neutral collision cross-section

Acronyms

API	Application Programming Interface
BATMAN	BAvaran Test MAchine for Negative ions
CFL	Courant-Friedrichs-Lewy
CPU	Central Processing Unit
CUDA	Compute Unified Device Architecture
DA	Dissociative Attachment
DAT	Data acquisition system
ED	Electron Detachment
EG	Extraction Grid
EM	ElectroMagnetic
ES	ElectroStatic
FLOPS	Floating point operations per second
GG	Ground Grid
GPU	Graphics Processing Unit
ITER	International Thermonuclear experiment reactor
LTP	Low Temperature Plasma
MPI	Message Passing Interface
NBI	Neutral Beam Injection
NI	Negative Ions
OpenMP	Open Multi-Processing
PG	Plasma Grid
PPC	Particle Per Cell
RAM	Random Access Memory
RF	Radio Frequency
RID	Residual Ion Dump
ROBIN	RF Operated Beam source in INdia
TMF	Transverse Magnetic Filter

DL	Double Layer
EDFs	Energy Distribution Functions
EEDFs	Electron energy distribution functions
EF	Electric Field
GB	GigaByte
GLOPS	GigaFLOPS (One Billion Floating Point Operations Per Second)
GSL	Gradient scale length
GW	Gaussian width
HDLT	Helicon double layer thruster
HPC	High Performance Computing
MB	MegaByte
MF	Magnetic Field
PO	Total power given to the system
SHFL	Shuffle
SIMD	Single Instruction Multiple Data
TFLOPS	TeraFLOPS (One Trillion Floating Point Operations Per Second)
IEDFs	Ion energy distribution functions
PIC-MCC	Particle In Cell Monte Carlo Collision

List of Tables

List of Figures

CHAPTER 1

Introduction and Literature survey

1.1 Introduction

High energy consumption due to rapid urbanization and population growth in the world is creating a global energy crisis. Considering the limitations of other sources such as fossil fuels, solar, wind, nuclear fission, etc.; nuclear fusion is emerging as one of the reasonable solutions to meet such a high energy demand, and it is also carbon emission-free. The concept of nuclear fusion, where the two lighter nuclei fuse to form a heavy nucleus while liberating an enormous amount of energy, offers itself as a future source of power with almost unlimited raw material. In a nuclear fusion reactor, hot fusion fuel in the form of plasma is confined using a magnetic field and is known as the magnetic confinement fusion approach [89, 119]. It is used in Tokamak magnetic confinement device, invented by Igor Tamm and Andrei Sakharov in the 1950s. First, Tokamak T1 was built at Kurchatov Institute in Moscow using the above design [6]. Several decades of research on nuclear fusion by different research groups across the world and international collaboration have resulted in ITER (International Thermonuclear Experiment Reactor) experiment. ITER will be the largest of more than 100 fusion reactors built since the 1950s and is being constructed in France. It is a joint collaboration among the European Union (EU), China, India, Japan, South Korea, Russia, and the United States of America [82]. At ITER, the plasma will be heated to 150 million degrees centigrade (about ten times the temperature at the core of the Sun). In an ITER-like big nuclear fusion reactor, desired temperature to sustain the plasma will be achieved by using different kinds of heating mechanisms such as ohmic

heating, wave heating, and Neutral Beam Injection (NBI) heating.

The NBI system, to heat the magnetically confined tokamak plasmas to desired temperatures, requires a hydrogen ion source to generate a high-energy neutral beam. The NBI penetration depth in the plasma depends on the energy of the neutral beam in eV, and beam energies in the range of MeV are required to penetrate to the core and heat plasmas in an ITER-like machine. Two types of NBI systems are available, one based on a positive hydrogen ion source while the other is based on a negative hydrogen ion source. However, for such high beam energies (of the order of MeV), the negative hydrogen ion sources are much better than the positive hydrogen ion sources in terms of neutralization efficiency. This has lead to a great deal of research interest towards the development of high current negative ion sources. The most important prerequisite for the development of a high current negative ion source is a uniform high density hydrogen plasma source. ITER has two NBIs, which provide a 33 MW supply of total power with 1 MeV beam energy during a pulse length of 3600 s [82, 112].

NBI system consists of four main parts: an ion source, acceleration grids, neutralizer, and Residual Ion Dump (RID) [109]. Negative ions are generated in a Low Temperature Plasma (LTP) based negative ion source and extracted through a large number of small apertures in the extraction grids. The negative ion beam is accelerated with energies in MeV order through the acceleration grids and reaches the neutralizer. Negative ions are converted into the neutral via collision with D_2 gas. All other charged particles from the beam are extracted using an electrostatic RID system. The efficient operation of the NBI systems depends on the effective functioning of the negative ion sources and a proper understanding of the physics of such systems.

In our studies, we have considered ROBIN (RF-Operated Beam source in INdia) negative ion source, which is installed at the Institute of Plasma Research (IPR), Gandhinagar, India [12, 13, 140]. The experimental program is being divided into two phases. In the first phase, plasma production has been carried out without negative ions by inductive coupling of RF power through a matching network. In the second phase, negative ion is being generated in volume mode and then surface mode with cesium vapour

evaporation in the ion source [12]. In such negative ion source, transverse magnetic filter (TMF) is used that controls plasma flux [54]. Magnetic filter helps in reducing the electron temperature and works as a cooler for high energy electrons [99, 137]. These low-energy electrons help to produce negative ions in the extraction region through dissociative attachment (DA) [4, 47]. There are two major drawbacks that lead to a reduction in negative ion yields. Firstly, high energy ($>$ 3.75 eV) electrons in the extraction region destroy negative ions due to electron detachment (ED) process [5], and secondly, the magnetic filter reduces the electron density (along with electron temperature) beyond desirable practical limits [23, 61]. A detailed understanding of the plasma transport across magnetic filter can help us to address the above-mentioned issues [135, 137]. Classical diffusion across the magnetic field is very well understood; however, there are instabilities inside plasma due to a non-uniform magnetic field, which gives rise to anomalous diffusion [23, 128]. Quantifying the role and contribution of classical diffusion, E$\times$B drifts, diamagnetic and anomalous diffusion towards plasma transport is very crucial for improving the efficiency of negative ion sources. In addition to theoretical investigations, some experiments have been also carried out to understand which diffusion (collisional or anomalous) dominates in cross-field diffusion of charged particles [42, 65, 149]. However, further investigations are required for a complete understanding of the physics associated with such a system.

To aid experimental investigation, several kinetic and fluid simulation models have been applied to study the physics of plasma transport across the magnetic field. Different aspects of cross-field diffusion mechanisms have been studied using fluid models such as electron mobility reduction, diffusion with Coulomb and electron-neutral collisions, E$\times$B and diamagnetic drifts [87, 100]. Fluid models do not capture the particle kinetics accurately. Therefore kinetic models are necessary [40] in this scenario. Different particle models have been successfully applied for LTP discharges which has provided important insights about LTP sources [146, 157, 158]. Particle-In-Cell based kinetic models have been applied by different groups for a better understanding of the plasma cross-field diffusion [23, 96, 99, 98, 112, 149, 160]. Few

researchers have suggested purely collisional transport whereas others have suggested anomalous transport, however, there is no quantitative data on the contribution of each based on kinetic modeling. Modeling of such negative ion sources with the above-mentioned challenges needs to address several critical issues such as: plasma production, gas chemistry and kinetics, plasma dynamics [27, 152], plasma transport across the filter [23, 24, 98, 100] and negative ion production and extraction [9, 153]. The primary objective of this thesis is to understand the physics of plasma transport across magnetic filter using 2D-3V PIC-MCC simulations and to conduct a direct comparison of the simulation results with experimental observations therby recognizing the primary factors responsible for anomalous transport reported in such plasmas.

1.2 Negative hydrogen ion sources for fusion

In the early 1970s, the use of a negative ion source in the NBI system for nuclear fusion experiments was proposed [15]. Due to high neutralization efficiency of $\approx$ 60 % even at beam energies of MeV, negative ion source has replaced positive ion source in big nuclear fusion reactor [81]. The negative ion source consists of a driver region, an expansion chamber, the magnetic filter, and the extraction system. The schematic of negative ion source is shown in Fig. (1.1). Hydrogen gas is feed inside the system in the pressure range of 0.4 Pa - 1.0 Pa. Plasma generated in the driver region expands into the expansion region. The Gaussian shaped magnetic field is used in the magnetic filter region, which is perpendicular to the plasma flow. Electrons get magnetized and gets trapped in the magnetic filter region, while ions remain unmagnetized. The goal of the magnetic filter is to cool down electrons below 2 eV for the prevention of NI loss through destruction processes. NIs are extracted through the extraction system. The extraction system consists of different grids: a plasma grid (PG), a ground grid (GG), and an extraction grid (EG).

Negative ions are generated through volume and surface modes. In volume mode, negative ions are generated in the expansion region through dissociative attachment of vibrationally excited ($\nu \geq 5$) hydrogen molecules ($H_2(\nu) + e \rightarrow H + H^-$) [52]. However, the mean free path of the NI is few

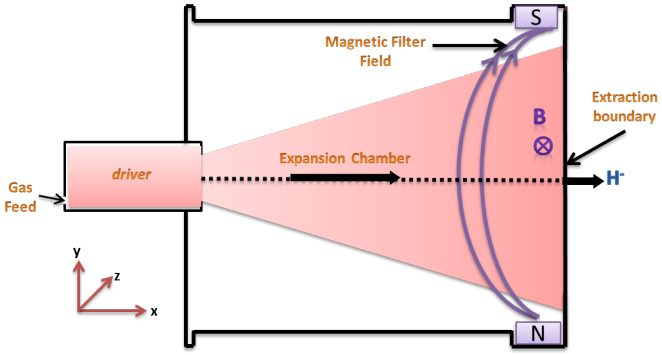

Figure 1.1: Schematic of the negative ion source.

centimeters because of the different NI destruction processes (such as mutual neutralization ($H^+ + H^- \rightarrow H + H$), associative detachment ($H + H^- \rightarrow H + H + e$ or $H_2 + e$), electron stripping ($e + H^- \rightarrow 2e + H$)) [52]. Destruction process occurs for electron with $\geq$ 2eV energy. In the surface mode, NIs are generated by striking hydrogen particles (H or H_2^+ or H^+) on the surface with low work function and absorbs electron near the grids. A low work function surface is achieved by covering the surface with a thin layer of caesium. In summary, the ion source comprises of a plasma generation chamber and an ion extraction acceleration system where a high voltage is applied to create a desired electrostatic electric field to accelerate the extracted ions from the plasma chamber.

The use of a magnetic filter in the negative ion source with a positive bias potential at the plasma grid to control plasma parameters was proposed by [42, 103]. As mentioned earlier, the weak magnetic filter is used in such negative ion source to enhance negative ion production near the extraction side by reducing the negative ion destruction probability through dissociative electron attachment due to cold electrons (electrons having energies less than 1.5 eV). The magnetic filter in the negative ion source leads to creation of two regions: one with hot plasma and another with cold plasma [3, 48]. A magnetic filter was used experimentally [87, 103] and decrements in electron temperature was observed which lead to enhancement in negative ion yield. Similar observations are also mentioned in [2, 48, 63, 70, 128]. Decremented electron temperature in the magnetic filter is explained using different mechanisms. A well established explanation is in terms of collisions. Electrons are strongly magnetized in the magnetic filter and the electron Larmor radius

is considerably smaller than magnetic filter size. Therefore, electrons go through many collisions in the magnetic filter region and lose energy. Due to the high diffusion coefficient of low energetic electrons, electrons with low energies diffuse faster across the magnetic filter than electrons with high energies [23, 70, 87, 88, 99]. The temperature gradient, the potential gradients and a plasma density gradient created by the in-homogeneous magnetic filter gives rise to various instabilities, and makes negative ion source operation complicated and difficult to understand [23, 77, 99].

1.3 Physics of plasma transport across magnetic filter

Plasma transport occurs mostly due to diffusion of particles from high density to the low density regions. Presence of electric and magnetic fields cause different diffusion phenomena (such as classical diffusion, ambipolar diffusion, anomalous diffusion etc.) which not only depends on density gradient, but also on the strength and direction of electric and magnetic fields, and the role of different collisional processes [40]. Diffusion can be described using fluid equation,

$$mn\frac{dv}{dt} = \pm en(E + v \times B) - \bigtriangledown P - mnvv \tag{1.1}$$

where, m-mass of particle, n-plasma density, e-electron charge, v-average particles velocity, ν-collision frequency, $\pm$-indicates sign of the charge, E-electric field, B-magnetic field, and $\bigtriangledown P$ -pressure gradient. In the steady state condition without magnetic field (B=0, $dv/dt = 0$), v can be expressed as,

$$v = \frac{1}{mn\nu}(\pm enE - kT \bigtriangledown n) \tag{1.2}$$

$$v = \pm\mu E - D\frac{\bigtriangledown n}{n} \tag{1.3}$$

where, k-Boltzmann constant, T-temperature in Kelvin, $\mu = \frac{e}{m\nu}$ is the mobility, $\bigtriangledown n$ is the density gradient and $D = \frac{kT}{m\nu}$ is the diffusion co-efficient.

In plasma, diffusion of electrons and ions are dependent on each other due

to collective behaviour and therefore even a slight deviation from the charge neutrality creates a large electric field. This new electric field, accelerates slower particles and retard faster particles. These leads to combined diffusion of oppositely charged particles, known as ambipolar diffusion [40]. It is expressed as:

$$D_a = \frac{\mu_i D_e + \mu_e D_i}{\mu_i + \mu_e} \tag{1.4}$$

where, D_a-ambipolar diffusion co-efficient, μ_i-ion mobility, μ_e-electron mobility, $D_i = \frac{kT_i}{m\nu_i}$-ion diffusion co-efficient, $D_e = \frac{kT_e}{m\nu_e}$-electron diffusion co-efficient, T_e-electron temperature, and T_i-ion temperature. Ambipolar diffusion is in the same direction for both negative and positive charges. Considering diffusion across B (in accordance with the coordinate system shown in Fig. (1.1 and 1.3)), Eq. (1.1) can be rewritten by using perpendicular components and neglecting nonlinear terms ,

$$v_x = \pm\frac{eE_x}{m\nu} - \frac{kT}{m\nu}\frac{1}{n}\frac{\partial n}{\partial x} \pm \frac{eB}{m\nu}v_y = \pm\mu E_x - \frac{D}{n}\frac{\partial n}{\partial x} \pm \frac{\omega_c}{\nu}v_y \tag{1.5}$$

$$v_y = \pm\frac{eE_y}{m\nu} - \frac{kT}{m\nu}\frac{1}{n}\frac{\partial n}{\partial y} \mp \frac{eB}{m\nu}v_x = \pm\mu E_y - \frac{D}{n}\frac{\partial n}{\partial y} \mp \frac{\omega_c}{\nu}v_x \tag{1.6}$$

where, $\omega_c = \frac{eB}{m}$-the cyclotron frequency, v_x and v_y-velocities are in X and Y directions, E_x and E_y-electric fields in X and Y directions. Replacing ν by $1/\tau$,where τ is collision time period, we can rewrite the above equations as follows.

$$v_y(1+\omega_c^2\tau^2) = \pm\mu E_y - \frac{D}{n}\frac{\partial n}{\partial y} - \omega_c^2\tau^2\frac{E_x}{B} \pm \omega_c^2\tau^2\frac{kT}{eB}\frac{1}{n}\frac{\partial n}{\partial x} \tag{1.7}$$

$$v_x(1+\omega_c^2\tau^2) = \pm\mu E_x - \frac{D}{n}\frac{\partial n}{\partial x} + \omega_c^2\tau^2\frac{E_y}{B} \mp \omega_c^2\tau^2\frac{kT}{eB}\frac{1}{n}\frac{\partial n}{\partial y} \tag{1.8}$$

The $\omega_c\tau$ term is useful to understand magnetic field trapping. If $\omega_c\tau >> 1$, particles are trapped effectively in magnetic filter. If not, then collision destroys the cyclotron orbits and cross-field diffusion take place. In general form, the cross-field velocity $v_\perp$ for either species can be written as,

$$v_\perp = \pm\mu_\perp E - D_\perp\frac{\bigtriangledown n}{n} + \frac{v_E + v_D}{1+(v^2/\omega_c^2)} \tag{1.9}$$

The cross-field velocity can be described by using cross-field mobility $\mu_\perp$, cross-field diffusion $D_\perp$, (E×B) drift velocity v_E and diamagnetic drift v_D [40].

These are expressed as,

$$\mu_\perp = \frac{\mu}{1+\omega_c^2\tau^2}, D_\perp = \frac{D}{1+\omega_c^2\tau^2}, \tag{1.10}$$

$$v_E = \frac{E\times B}{B^2}, v_D = \pm\frac{B\times\bigtriangledown p}{enB^2} \tag{1.11}$$

$D_\perp$ is classical diffusion which varies as a $1/B^2$. If $\omega_c^2\tau^2 >> 1$, then classical diffusion can be written as,

$$D_\perp = \frac{D}{\omega_c^2\tau^2} = \frac{kT_e m_e \nu}{e^2B^2} \tag{1.12}$$

Parallel diffusion from $D = \frac{kT}{m\nu}$ depends on ν^{-1}, whereas, perpendicular diffusion depends on ν as seen in Eq. (1.12).

In most low temperature experiments involving magnetic field, diffusion across magnetic field is non-classical. As shown above, classical diffusion strongly depends on magnetic field ($\sim 1/B^2$), however experimental results reveal a dependency of the form ($\sim$1/B). This was first noticed by Bohm, Burhop and Massey in 1946 and is known as Bohm diffusion [18, 37]. This type of anomalous diffusion has been reported in many low temerature experiments [22, 23, 38, 40]. Bohm diffusion (D_{Bohm}), expressed as eq. 1.13 can explain such experimental observations.

$$D_{Bohm} = \frac{1}{16}\frac{kT_e}{eB} \tag{1.13}$$

It represents the maximum diffusion rate in plasma perpendicular to the magnetic field lines and can be explained by plasma instabilities observed in such systems.

As mentioned in earlier section 1.1, different fluid, as well as kinetic models, have been applied to understand the physics of the plasma transport across the magnetic filter. Initially, plasma chemistry of the H_2/D_2 was studied in detail using the 0D model [32]. Afterwards, global models are used to understand complex plasma chemistry [115, 162, 163]. 1D model was developed for negative ion sources in the context of fusion [70, 163]. Subsequently, various models are being developed to investigate different aspects of plasma

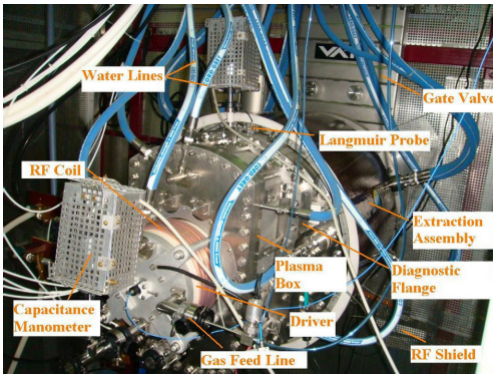

Figure 1.2: Negative ion source mounted on the vacuum vessel in ROBIN test bed at IPR, Gandhinagar, India [12].

transport across the magnetic filter in the negative ion source; such as background plasma transport across magnetic filter [99, 100], H_2 gas kinetics and dynamics in the expansion region [152], negative ion transport and extraction process [64, 75], and surface production of negative ions [148]. All these models are not self-consistent and do not describe the complete source (driver to the extraction regions). A self-consistent 2D fluid model was developed to understand properties of background plasma [27, 71]. Recently, many research groups have been reporting about the 1D, 2D and 3D PIC model based simulations of negative ion sources [58, 66, 101, 110, 116, 151, 159, 160].

1.4 ROBIN negative ion source

ROBIN negative ion source (Fig. 1.2) is a replica of BATMAN negative ion source (at IPP, Garching, Germany) [145]. The schematic of the ROBIN is shown in Fig. (1.3) [8, 12, 13, 41]. Hydrogen gas is injected inside the system by using gas feeding system with mass controller. Plasma ignition is done by primary electrons generated using a thoriated tungsten filament. Plasma is produced inside the *driver* using RF inductive coupling through matching network. The maximum extraction voltage between PG and EG is 10 kV. Bias plate is situated between the magnetic filter and PG in the extraction system and it is positively biased with respect to the source chamber. This bias potential is nearly equal or more than plasma potential. It is set according to the requirement of the extraction current. Gaussian shaped magnetic field with a peak value of 7 mT is applied between expansion chamber and extraction

region. Low temperature plasma is generated inside the chamber with electron temperature between 1-10 eV and electron density $n_e \approx 2 \times 10^{18}\ m^{-3}$ [13, 12].

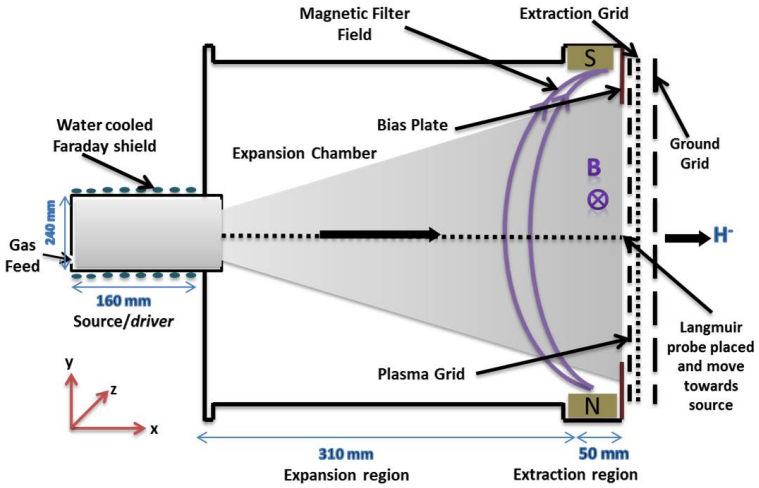

Figure 1.3: Schematic diagram of ROBIN. Movable Langmuir probe is placed near the central Y-axis, and it can be moved between *driver* and extraction region.

Parameter	**Value**	**Remarks**
X-dimension	0.52 m	Operational parameter
Y-dimension	0.25 m	
Z-dimension	0.40 m	
Gas pressure	0.6 Pa	
Power	60 kW	
Bias Voltage	0-25 V	
Magnetic field	7×10^{-3} T	
Gaussian width of B	0.29 m	
Peak of Gaussian B	94 % of length	
Gas temperature	1000 K	Experimental output
Charge species	electrons, ions	
RF source frequency	1 MHz	
Electron temperature	1-10 eV	
Plasma density	$2 \times 10^{18}\ m^{-3}$	

Table 1.1: Important parameters from ROBIN experiments.

In the first phase of ROBIN experiments, plasma production has been carried out without negative ion generation and different plasma parameters have been measured [12]. Charged species in the experiment are electrons and ions [12]. Power given to the system is around 60 kW - 100 kW. The basic experimental parameters are given in Table 1.1. Different Langmuir probes and emission spectrometer have been installed for purpose of diagnosis.

Figure (1.4) shows plasma density and electron temperature at different input

RF power from first phase ROBIN experiments [12]. Data are collected using Langmuir probes mounted on top and bottom of the diagnostic flange (diagnostic flange shown in Fig. (1.2)). Till 50 kW power, plasma density increases, but beyond that, it starts saturating (shown in Fig. (1.4-a)). Electron temperature is higher than expected (shown in Fig. (1.4-b)); this may be attributed to the RF uncompensated Langmuir probe. The plasma density and electron temperature from the top and bottom probes are different, that is due to asymmetry caused by drifts in the source [12]. Plasma non-uniformity is observed in the vertical plane of ROBIN [14]. More details related to experimental diagnostics used in the ROBIN experiments can be found in [12].

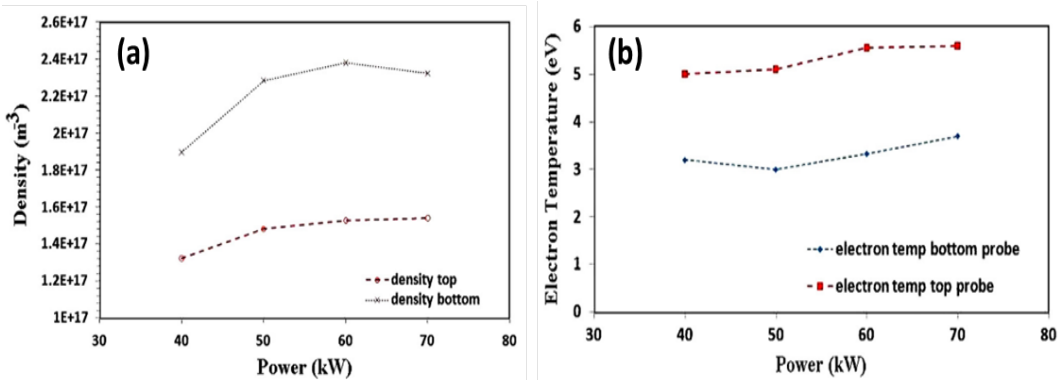

Figure 1.4: (a) Plasma density in m^{-3} and (b) electron temperature in eV as a function of input RF power from ROBIN first phase experiment [12].

1.4.1 Length and Time scales

Basic physical parameters related to plasma transport under typical ROBIN experimental conditions as well as important time and length scales are calculated, and provided in Table 1.2. Typical magnetic field and electron temperature found in ROBIN experiments are in the rage of 0-10 mT and 1-10 eV, respectively [12]. In the magnetic filter region, magnitude of collision frequencies as well as the diffusion mechanisms change due to the Gaussian shaped magnetic field and fall in electron temperature. It is important to understand the role of different collisions and look into the variation of different collision frequencies as a function of electron temperature typically seen in negative ion source experiments.

Figures (1.5) and (1.6) shows the important length and time scales necessary to understand the physics of plasma transport under ROBIN experimental

Length scales		
Physical parameter	**Equations**	**Value**
Debye length (λ_D)	$(\frac{\epsilon_0 kT}{n_e e^2})^{1/2}$	$7.43 \times 10^{-6} m$ ($\frac{kTe}{e}$=1 eV) $2.35 \times 10^{-5} m$ ($\frac{kTe}{e}$=10 eV)
electron Larmor radius (R_{Le})	$\frac{0.0238 T_e^{1/2}}{B}$	$3.40 \times 10^{-6} m$ ($\frac{kTe}{e}$=1 eV) $1.08 \times 10^{-5} m$ ($\frac{kTe}{e}$=10 eV)
ion Larmor radius (R_{Li})	$\frac{(1.02 \times m_i/m_e)^{1/2} T_i^{1/2}}{B}$	$9.96 \times 10^{-3} m$
Time scales		
plasma frequency (ω_p)	$(n_e e^2/m\epsilon_0)^{1/2}$	5.64×10^{10} Hz
electron cyclotron frequency (ω_{ce})	$\frac{eB}{m_e}$	1.231×10^8 Hz
ion cyclotron frequency (ω_{ci})	$\frac{eB}{m_i}$	0.335×10^6 Hz
ele-ion Coulomb collision frequency (ν_{ei})	$\frac{n_i e^4 ln\lambda}{4\pi\epsilon_0^2 m_i^{1/2} (3kT)^(3/2)}$	$2.79 \times 10^7 Hz$ ($\frac{kTe}{e}$=1 eV) $2.49 \times 10^6 Hz$ ($\frac{kTe}{e}$=5 eV) $8.81 \times 10^5 Hz$ ($\frac{kTe}{e}$=10 eV)
ele.-neutral collision frequency (ν_{en})	$n_o \sigma_{en} \frac{kT_e}{m_e}^{1/2}$	$6.08 \times 10^6 Hz$ ($\frac{kTe}{e}$=1 eV) $1.36 \times 10^7 Hz$ ($\frac{kTe}{e}$=5 eV) $1.92 \times 10^7 Hz$ ($\frac{kTe}{e}$=10 eV)
ion-neutral collision frequency (ν_{in})	$n_o \sigma_{in} \frac{kT_i}{m_i}^{1/2}$	$2.29 \times 10^4 Hz$
Other parameters		
plasma potential (V_{pp})	$(\frac{kT_e}{2e})[1 + ln(\frac{m_i}{2\pi m_e})] = 3.7\frac{kT_e}{e}$ in case of H_2 taking bias voltage 0 V	21.9 V ($\frac{kT_e}{e}$ = 6 eV)
plasma parameter (N_D)	$\frac{4}{3}\pi\lambda_D^3 n_e$	$5.44 \times 10^4 >> 1$
Bohm velocity	$(\frac{kT_e}{m})^{1/2}$	$1.33 \times 10^6 m/s$
electron diffusion co-efficient (D_e)	$\frac{kT_e}{m_e \nu_{en}}$	$7.88\ m^2/s$
ion diffusion co-efficient (D_i)	$\frac{kT_i}{m_i \nu_{in}}$	$3.61\ m^2/s$
classical diffusion co-efficient (D_{class})	$\frac{kT_e m_e \nu_{ei}}{e^2 B^2}$	$1.02\ m^2/s$
Ambipolar diffusion co-efficient (D_a)	$D_{\perp i}\frac{T_e}{T_i}$, $D_{\perp i}$-ion diffusion co-efficient	$1.39 \times 10^3 m^2/s$
Bohm diffusion co-efficient (D_{Bohm})	$\frac{kT_e}{16eB}$	$89.3\ m^2/s$

Table 1.2: Different length scales and time scales using electron temperature kT_e/e = 10 eV, ion temperature kT_i/e = 0.026 eV and magnetic field B = 7 mT [90], m_i - ion mass, m_e - electron mass. Electron (or ion) collision cross section σ_{en} and σ_{in} - $1.00 \times 10^{-19} m^2$ [31, 124, 125, 147, 155].

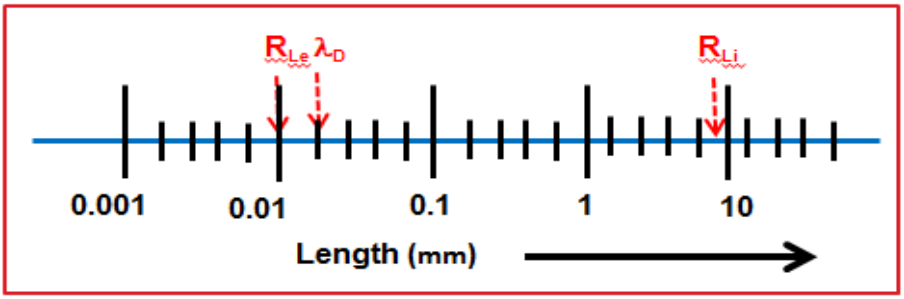

Figure 1.5: Different length scale using electron temperature kT_e/e = 10 eV, Ion temperature kT_i/e = 0.026 eV, B = 7 mT.

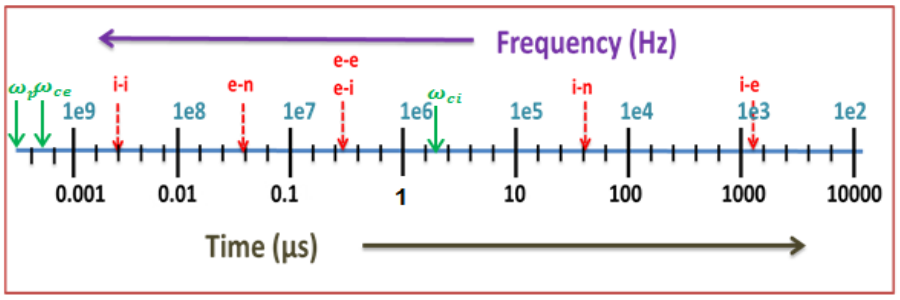

Figure 1.6: Different time scale using, electron temperature kT_e/e = 10 eV, Ion temperature kT_i/e = 0.026 eV, B = 7 mT, Electron and ion collision cross-section = 1.00×10^{-19} m^2

conditions. At 7 mT magnetic field, Debye length (λ_D) and electron Larmor radius (R_{Le}) is in order of 0.01 to 0.02 mm (Fig. (1.5)). Ion Larmor radius (R_{Li}) is 1000 times larger than electron Larmor radius. In this condition, ions are either weakly magnetized or remain unmagnetized. Plasma frequency (ω_p) and electron cyclotron frequency (ω_{ce}) are the highest frequencies in the order of 10^9 Hz. All collision frequencies are lower than plasma and electron cyclotron frequencies. This means that the Hall parameter (h_e) for electrons (the ratio of electron cyclotron frequency to the collision frequency) is greater than 10. It also indicates that electrons are strongly magnetized in the ROBIN source, whereas the ion Hall parameter (h_i) is less than 1, showing that ions are not magnetized.

1.4.2 Collision frequencies and diffusion

Typical magnetic field and electron temperature observed in ROBIN experiments are in the rage of 0-10 mT and 1-10 eV respectively [12]. In the magnetic filter region, magnitude of collision frequencies as well as the diffusion mechanisms change due to the Gaussian shaped magnetic field

and fall in electron temperature. It is important to understand the role of different collisions and look into the variation of different collision frequencies as a function of electron temperature typically seen in negative ion source experiments.

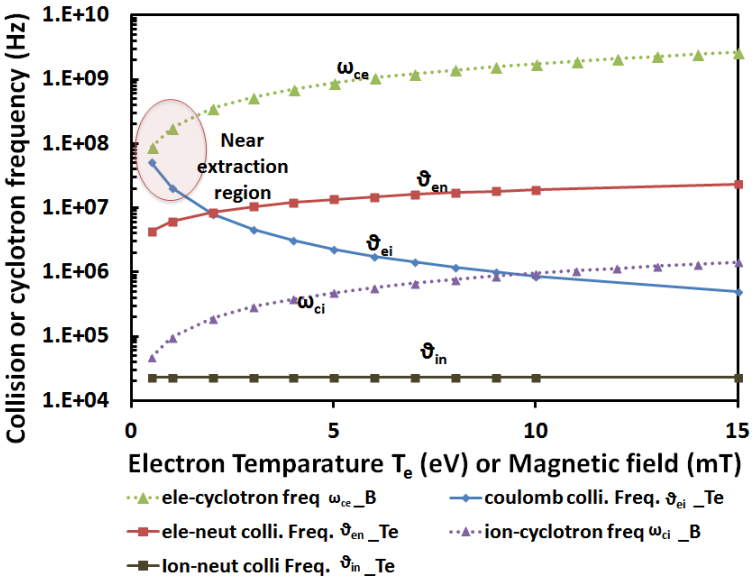

Figure 1.7: Collision frequency vs. electron temperature, and cyclotron frequency vs Magnetic field plot. Coulomb and electron-neutral collision frequencies are represented by blue and brown line respectively for different electron temperatures in eV. Green and purple line represents electron and ion cyclotron frequency in Hz for given magnetic field in mT. Neutral density $n_o = 1.45 \times 10^{20}\ m^{-3}$, and electron and ion density $n_e = n_i = 10^{18}\ m^{-3}$. Electron and ion collision cross section are of the order of $10^{-19}\ m^2$ [124, 125].

We can see from Fig. (1.7), that for a typical electron density of around $10^{18}\ m^{-3}$, electron-neutral collision dominates over Coulomb collisions at temperatures greater than 3 eV, however at lower temperatures (typically seen in the extraction region) Coulomb collisions dominate. Electron cyclotron frequency is always higher than ion-cyclotron frequency due to lower mass of electrons as seen in Fig. (1.7), and we can also see that electron cyclotron frequency is always higher than all other (electron-neutral, electron-ion, and ion-neutral) collision frequencies. This means, electrons are strongly magnetized, and undergo effective cyclotron trapping, whereas ion cyclotron orbits are destroyed by collisions, and ions remain unmagnetized. One of the important regions in Fig. (1.7) is the area marked by a red circle, where electron temperature is less than 2 eV. This scenario happens near the extraction region, where the Gaussian magnetic field starts falling sharply (typically 1 mT and below). and electron temperature drops very fast [23, 54, 132]. In this

region, Coulomb collision frequency is nearly equal to the electron cyclotron frequency and therefore electron cyclotron orbits are destroyed by electron-ion Coulomb collisions. This leads to ineffective electron cyclotron trapping in this region and electron loses energy due to collisions.

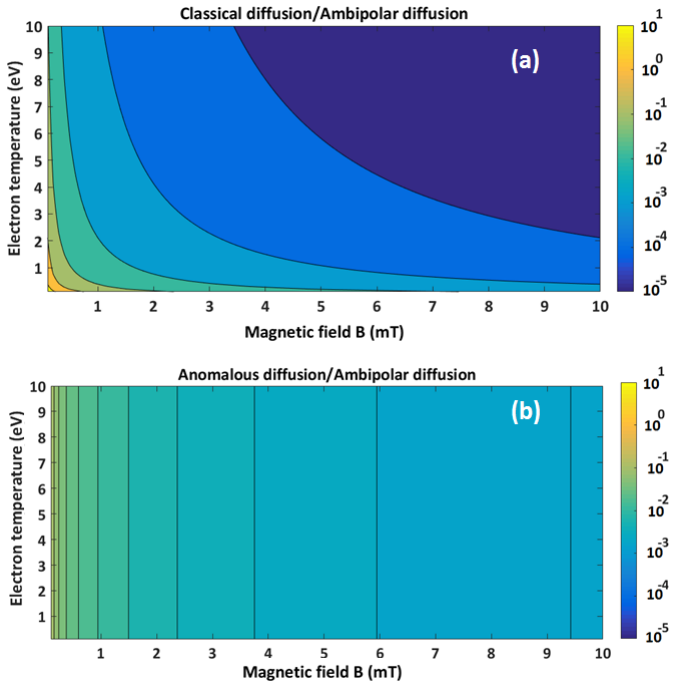

Figure 1.8: (a) ratio of classical diffusion to ambipolar diffusion, (b) ratio of anomalous to ambipolar diffusion contours for different magnetic field B in mT and electron temperature in eV. Ratios are in log scale. Neutral density $n_o = 1.45 \times 10^{20}\ m^{-3}$, and electron and ion density $n_e = n_i = 10^{18}\ m^{-3}$. Electron and ion collision cross section are of the order of $10^{-19}\ m^2$ [124, 125]. Ion temperature is 0.026 eV.

Classical and Bohm diffusion depends on electron temperature as well as magnetic field, whereas ambipolar diffusion depends only on the electron temperature and not on the magnetic field. As seen from Fig. (1.8) for typical values of electron temperature and magnetic field (considering electron and ion density $n_e = n_i = 10^{18}\ m^{-3}$), ambipolar diffusion $>$ Bohm diffusion $>$ classical diffusion. For lower electron temperature and lower magnetic field (typical scenario near extraction region), magnitude of all the diffusions are nearly similar. Classical and Bohm diffusion follows $1/B^2$ and $1/B$ trends, respectively. Presence of different combinations of magnetic field and electron temperatures leads to different dominant diffusion mechanism in different regions of the negative ion source. In the case of a low magnetic field of less than 1 mT, classical diffusion dominates over all other diffusion processes. At

higher magnetic fields, ambipolar diffusion dominates over all other diffusions due to density gradients as seen in Fig. (1.8). From these two figures (1.7 and 1.8), we can conclude that near the extraction region (where the magnetic field is low and electron temperature is below 2 eV) the role of collisions and diffusion on the plasma transport changes drastically. Data and broad trends presented in this section will aid us to understand the simulations results presented in the thesis.

1.5 Contribution of the Thesis

The low-temperature plasma (LTP) with a magnetic field in a low-pressure condition has a wide range of applications such as negative ion source [23, 54, 132], Hall thrusters [68], magnetron discharge [105], electron cyclotron resonance source [67], ion-mass separator, linear magnetized machines and end-hall source [95]. Electrons in such plasmas are magnetized, whereas ions are not completely magnetized. The presence of an inhomogeneous magnetic field along with a non-uniform electric field in such applications leads to E×B drifts thereby leading to complex plasma transport. Such a plasma source with a non-thermal equilibrium state, inhomogeneous magnetic and electric field, leads to the asymmetry in the plasma density, temperature, and pressure. The gradients in plasma parameters, different drifts (e.g. E$\times$B drift, grad-B drift, polarization drift, diamagnetic drift etc.) and several collisional processes result in fluctuations or instabilities in the plasma, which can increase the electron cross field mobility that cannot be explained by the physics of classical collisional mobility. Complex plasma transport involving several time and length scales necessitates the need of computationally expensive kinetic simulations, such as Particle-in-Cell Monte Carlo collision (PIC-MCC), to improve the current understanding of anomalous transport in such systems. In this thesis, we have used a simple negative ion source geometry with a transverse magnetic filter as a testbed problem for our investigations, however the complexities and physics issues are similar for all the above mentioned devices of interest.

For efficient negative ion beam generation, the transverse magnetic filter

(TMF) plays an important role in the negative ion source. TMF plays three different tasks: 1) cools down electrons below 2 eV to minimize destruction of negative ions by decreasing electron stripping, associative detachment, and mutual neutralization. 2) reduces the number of co-extracted electrons due to reduced electron temperature and density. 3) increases surface-produced negative ions extraction probability. However, TMF has several disadvantages associated with it such as the generation of instabilities and drifts leading to anomalous plasma transport and it also creates asymmetry near the extraction region in the plasma [23, 54, 57]. To address these issues, a detailed accurate computational investigation of plasma transport across TMF is required which can explain the experimental observations and aid in future experimental activities.

PIC-MCC is a widely used particle based computational technique to investigate low-temperature plasmas (LTP). It involves solution of Vlasov-Poisson equations, and provides spatial and temporal evolution of the charged-particle velocity distribution functions under the effect of self-consistent electromagnetic (EM) fields and collisions [16, 133]. PIC MCC method calculates trajectories and velocities of each particle on the Lagrangian grid (mesh-free) and calculates collective behavior such as potential by solving Poisson's equation on Euler grids. The computational cost of PIC-MCC code is decided by grid size, the number of computational particles (a bunch of real particles), dimensions of phase-space, time-step, and total number of iterations required to complete simulations [36, 38, 133, 134]. Strict numerical constraints on time-step ($< \omega_p$), grid spacing ($< \lambda_D$), and number of particles per cell (PPC) (> 10) makes computation even more challenging [23, 66]. Considering large size negative ion source geometry, small-time step in the order of few ns, small grid spacing in the order of 10^{-4} m, and high plasma density in the order of 10^{18} m^{-3} makes 2D-3V PIC MCC simulation computationally very expensive for such studies. On a standard Desktop, it may take several months to simulate such problems. These necessities the sophisticated parallelization of the PIC-MCC code and its execution on advanced HPC (High-Performance Computing) facilities for the problem at hand.

The thesis is focused on the following main aspects:

- Understanding the physics of plasma transport across magnetic fields (TMF) in negative ion sources for fusion applications.
- Develop an accurate numerical model (kinetic, PIC-MCC) to study the plasma transport across the magnetic field in the context of negative ion sources.
- Parallel Particle-in-Cell Monte Carlo Collision (2D PIC-MCC) Code development on latest computer architectures to study large problem sizes in the context of negative ion sources for ITER-NBI systems.
- Comparison and benchmarking of computational results with published experimental data from ROBIN negative ion source. Understand the effect of magnetic filter configuration on plasma transport.
- Detailed investigation of instabilities and double layers observed in such systems and its possible role on anomalous plasma transport.
- Perform different case studies with experimental viewpoint (with real ROBIN experiment parameters) along with necessary plasma characterization to provide useful feedback for future experiments.

1.6 Organization of the thesis

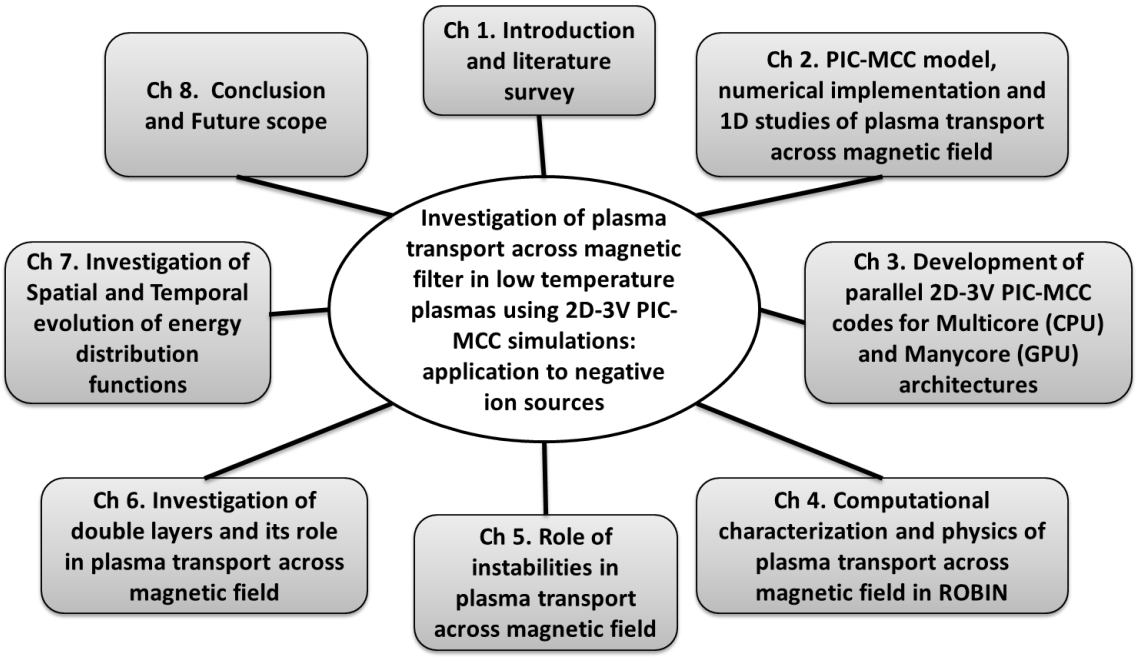

Figure 1.9: Organization of the thesis chapters.

The thesis is being planned to be structured in eight chapters as shown in Fig. (1.9). In chapter 2, the PIC-MCC kinetic model is discussed and results from 1D-3V PIC-MCC simulations as well as comparison with experimental results are included. Chapter 3 focuses on the development of efficient parallel 2D-3V PIC-MCC algorithm for computationally expensive 2D simulations. In chapter 4, the physics and results associated with computational characterization of the plasma transport across magnetic filter under conditions similar to phase I ROBIN experiments have been included. Identification and investigation of instabilities as well as its role on plasma transport is discussed in chapter 5. In chapter 6, the possibility of double layer formation in such plasmas and its role towards anomalous transport has been discussed. Detailed spatio-temporal EDF analysis using the data obtained from PIC-MCC simulations and its importance in interpreting the experimental observations is included in chapter 7. Conclusion, general remarks and future scope are included in the final chapter.

CHAPTER 2

PIC model and 1D studies of plasma transport across magnetic field

Low-temperature plasmas (LTP) with low gas pressure and weak magnetic field generate non-thermal plasma with magnetized electrons and unmagnetized or partially magnetized ions. Modeling such complex LTP requires the solution of all particle kinetics, transport, collisions, and proper plasma source modeling. It involves the solution of non-linear differential equations with several unknowns. As discussed in Chapter 1, section 1.4.1, under the conditions of negative ion source, important time scales varies from 10^{-4} s to 10^{-10} s and length scales varies from 10^{-3} m to 10^{-6} m. For accurate investigations, these different time and length scales have to be resolved simultaneously and self-consistently [92]. Out of two widely used approaches, the fluid model initially guesses the velocity distribution function of particles and solve moments of the Boltzmann equation, whereas the particle model tracks particle individually and represents the distributions by a large number of particles [92]. In the fluid model, the velocity distribution is determined from the electric field or local energy dissipation. Due to this, the fluid model fails to accurately capture the non-local effects in such LTP. Using the kinetic model, due to tracking of individual particles, we can capture non-local, kinetic, and non-linear effects encountered in such LTP [92]. It is one of the primary reasons to use kinetic modeling-based simulations for our investigations.

In this chapter, the PIC-MCC kinetic model used in our work is described in detail, along with its algorithmic implementation and associated challenges.

This study uses a self-consistent electrostatic kinetic method for the particle-in-cell Monte-Carlo Collision (PIC MCC). In this method, the self-consistent electrostatic force is calculated using Coulomb's law, where N^2 operations are required for N charged particles. The reduction of the computation is made by introducing grids in the model. In the 1970s, the PIC method was established by Birdsall and Langdon [16], and Hockney and Eastwood [85]. Considering the computational complexity of the PIC code, as a first step, we have used the 1D-3V PIC-MCC code for understanding the ROBIN experimental results. The results from 1D studies, comparison with experimental results, and the limitations of the 1D model are presented in this chapter.

Organization of chapter

This chapter is divided into two parts. First part is focused on the development of PIC-MCC kinetic model (section 2.1), whereas, comparison of simulation results with experimental results are presented in the second part (section 2.2) . Section 2.1 presents important details related to PIC-MCC kinetic model used in this thesis, hydrogen chemistry considered in MCC (section 2.1.1), numerical constraints associated with PIC-MCC (section 2.1.3), scaling (section 2.1.5), power module considered in the model (section 2.1.2), and associated computational challenges (section 2.1.4). 1D studies on plasma transport across magnetic filter is given in section 2.2 along with convergence studies in section 2.2.1. Comparison of 1D-3V simulation results with ROBIN first phase experiment results is provided in section 2.3. Finally, the chapter ends with conclusions in section 2.4.

2.1 PIC-MCC kinetic model

PIC-MCC is a widely used particle-based computational technique to investigate low-temperature plasmas (LTP). It involves the solution of Vlasov-Poisson equations and provides spatial and temporal evolution of the charged-particle velocity distribution functions under the effect of self-consistent electromagnetic (EM) fields and collisions [16, 133]. Charged

particle collisions with neutral atoms in the PIC-MCC algorithm are taken into account using the random sampling-based Monte-Carlo Collisions (MCC) method [16, 118]. PIC is a self-consistent method wherein the motion of charged particles is solved in the presence of self-consistent fields as well as externally applied EM fields. When the current generated by plasma is low, the self-induced magnetic field can be ignored, and it is known as the Electrostatic (ES) PIC method.

The flowchart of self-consistent ES PIC-MCC method used in our work is shown in Fig. (2.1) [133]. The algorithm consists of two grids (mesh-free Lagrangian grid and fixed Euler grid). The trajectories of a representative number of charged particles are evolved in the Lagrangian grid (mesh-free), and the collective interaction of the particles is described by solving Poisson's equation on the Euler grid (fixed grid point) [16, 92]. It involves splitting of the kinetic Vlasov-Poisson equation (Eq. (2.1)) into two ordinary differential equations (Eq. (2.2) and Eq. (2.3))

$$\frac{\partial f}{\partial t} + v \cdot \frac{\partial f}{\partial r} + \frac{q}{m} \cdot \left(\vec{E} + \vec{v} \times \vec{B} \right) \cdot \frac{\partial f}{\partial v} = \left(\frac{\partial f}{\partial t} \right)_{colli} \tag{2.1}$$

where, *f(r,v,t)* is distribution function, r is position of particle, v is velocity of particle, t is time, q is charge, m is mass, $\vec{E}$ is electric field, $\vec{B}$ is magnetic field and $\left(\frac{\partial f}{\partial t} \right)_{colli}$ is change in distribution function f with time due to collision.

$$\frac{d\vec{r}}{dt} = \vec{v} \tag{2.2}$$

$$\vec{F} = m\frac{d\vec{v}}{dt} = q \cdot \left(\vec{E} + \vec{v} \times \vec{B} \right) \tag{2.3}$$

Different blocks of ES-PIC-MCC shown in Fig. (2.1) are explained below. Temporal time step and grid spacing have been represented using Δt and Δx, respectively.

A. Initial particle loading

Computational charged particles (superparticles representing many physical particles - electrons and ions) are loaded inside the simulation domain either uniformly or non-uniformly. The same charge-to-mass ratio for both simulation (superparticles) and physical particles [156] are considered, and superparticles follow the same trajectory as the corresponding plasma particle. Each *superparticle* represents 10^6 to 10^7 real particles. In uniform distribution, particles are inserted uniformly all over the simulation domain, whereas in non-uniform distribution, particles are loaded in the source region instead of the entire volume. Particles in PIC simulation are injected by either initial particle loading as described earlier, or via particles re-injection from the boundary, or using a volumetric source. In our implementation, computational particles (representing electrons and ions) are uniformly loaded inside the simulation domain, and their positions and velocities are assigned randomly [55]. Generally, a Maxwellian distribution function is used for initialization

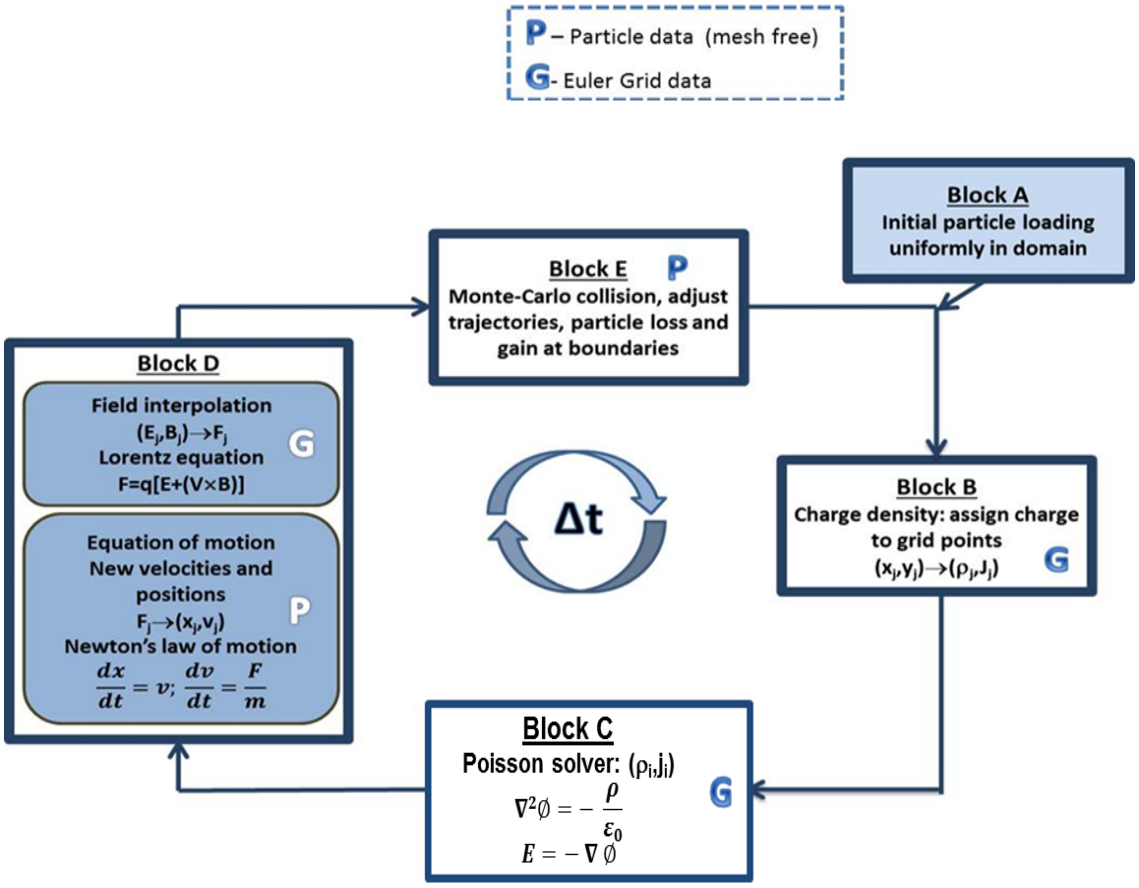

Figure 2.1: Flowchart of the ES PIC-MCC algorithm.

of particle velocities [43]. This distribution evolves with time due to particle interaction through collisions, electric, and magnetic field.

B. Particles to grid charge density interpolation

Charge Deposition on grid points, used to convert the Lagrangian phase space information to Euler-grid points, for calculation of electric field is a computationally expensive part of the PIC-MCC method. A particle contributes its charge to the surrounding points and this is accomplished by performing interpolation at every iteration for all particles. We have used a linear interpolation scheme which is less noisy, and computationally cheaper compared to zeroth order and higher order schemes [17].

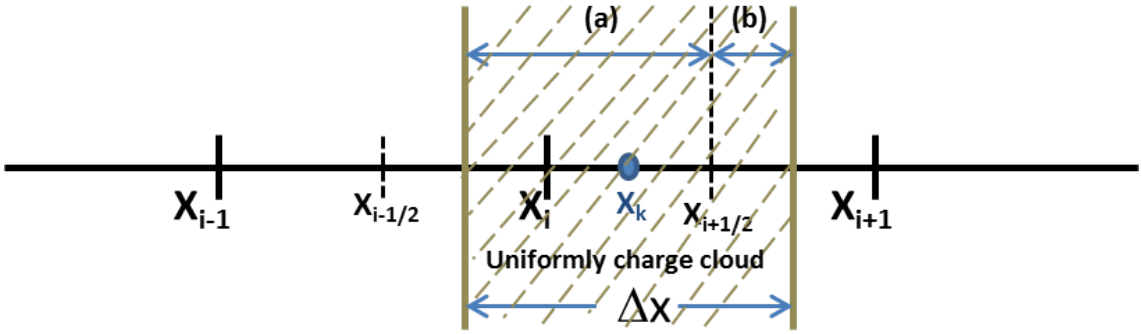

Figure 2.2: First order cloud-in-cell weighing scheme. Blue dot is charged particle. i-1, i, and i+1 are three grid points. Cloud is centred at X_k. Part of the cloud falls in X_i is weighted on X_i (fraction (a)), and part of the cloud falls in X_{i+1} is weighted on X_{i+1} (fraction (b)).

In 1D, the nearest grid point (NGP) method, a zeroth-order scheme, relies on counting the number of particles within distance $\pm\frac{\Delta X}{2}$, where ΔX is the grid spacing. We have used first order linear interpolation scheme (cloud-in-cell scheme), which reduces noise compared to the NGP method, but it requires twice computation. Interpolation scheme is shown in Fig. (2.2) and given by Eq. (2.4) and Eq. (2.5) [16].

$$q_i = q_c\left(\frac{\Delta X - (X_k - X_i)}{\Delta X}\right) = q_c\left(\frac{X_{i+1} - X_k}{\Delta X}\right) \tag{2.4}$$

$$q_{i+1} = q_c\left(\frac{X_k - X_i}{\Delta X}\right) \tag{2.5}$$

Where, X_k is position of charge particle. X_i and X_{i+1} are nearest grid points, ΔX is grid size, and q_c is total cloud charge. Above Eq. (2.4) and Eq. (2.5) are used for calculating the part assigned to i and i+1 for total cloud charge of q_c.

C. Field calculation

Charge densities calculated at grid points are used to compute scalar potential by solving Poisson's Eq. (2.6). We have used PARDISO library to solve Poisson's equation. PARDISO library is an optimized, high-performance, and memory-efficient parallel library for solving large sparse linear systems of equations on multiprocessors [131]. Finally, the electric field E at the grid points is computed using the finite difference form of Eq. (2.7).

$$\bigtriangledown^2\phi = -\frac{\rho}{\epsilon_0} \tag{2.6}$$

$$\vec{E} = -\vec{\bigtriangledown}\phi \tag{2.7}$$

where, ϕ is potential, ρ is charge density, and ϵ_0 is permittivity of free space.

D. Grid to particle interpolation (*Mover*)

New velocities and positions of particles are calculated using the modified field on Euler-grids. Euler grid to Lagrangian node transformation is accomplished by linear interpolation which is similar to the interpolation scheme described in the previous section 2.1.B. Force given by Eq. (2.3) is used to update equations of motion (Eq. (2.2) and Eq. (2.3)) by using Boris method [28]. *Mover* is also computationally intensive due to calculation of position and velocity of all the particles.

E. Monte-Carlo Collision (MCC)

Monte-Carlo collision model is applied to particles. Collision probabilities are calculated. Particles selected randomly undergo collisions according to the collision probabilities [156]. Types of collisions are also decided by the above method. Collisions change the momentum of the particles, and new velocities

are calculated [38].

2.1.1 Hydrogen Chemistry

H_2 gas is considered with a density of 1.45×10^{20} m^{-3}. Important electron-neutral molecular collisions (elastic and inelastic such as excitation and ionization) are taken into consideration using the set of cross-sections of Phelps in the electron scattering database LXcat [33, 125]. Only H_2^+ positive ion is considered. Ionization cross-section for H_2^+ ion is higher than that of H^+ ion, therefore H_2^+ is considered. Detailed hydrogen chemistry for ion energy below 1 eV, which leads to the formation of the H_3^+, is not taken into account. Coulomb collisions are considered as discussed in Ref. [23]. Detailed hydrogen chemistry is listed in Table 2.1. Collision cross-section for all 16 types of collisions (as given in Table 2.1) are shown in Fig. (2.3).

#	Reaction	Energy	Type
1	$H_2 + H_2$	-	Momentum transfer
2	$H_2(J=0) \rightarrow H_2(J=2)$	0.044 eV	Rotational excitation
3	$H_2(J=1) \rightarrow H_2(J=3)$	0.073 eV	Rotational excitation
4	$H_2 \rightarrow H_2(v=1)$	0.516 eV	excitation
5	$H_2 \rightarrow H_2(v=2)$	1.000 eV	excitation
6	$H_2 \rightarrow H_2(v=3)$	1.500 eV	excitation
7	$H_2 \rightarrow H_2(b3)$	8.900 eV	excitation
8	$H_2 \rightarrow H_2(b1)$	11.300 eV	excitation
9	$H_2 \rightarrow H_2(c3)$	11.750 eV	excitation
10	$H_2 \rightarrow H_2(a3)$	11.800 eV	excitation
11	$H_2 \rightarrow H_2(c1)$	12.400 eV	excitation
12	$H_2 \rightarrow H_2(d3)$	14.000 eV	excitation
13	$H_2 \rightarrow H + H(n=2)$	15.000 eV	dissociative excitation
14	$H_2 \rightarrow H_2$	15.200 eV	sum of excitation of Rydberg levels
15	$H_2 \rightarrow H + H(n=3)$	16.600 eV	dissociative excitation to Balmer alpha (N=3)
16	$H_2 \rightarrow H_2^+$	15.400 eV	Ionization

Table 2.1: Hydrogen chemistry involved in the 1D-3V PIC-MCC simulations [33, 125].

2.1.2 Power Absorption

While comparing simulation results with experiments, we should have a good estimation of the input power given in the experimental set-up and how

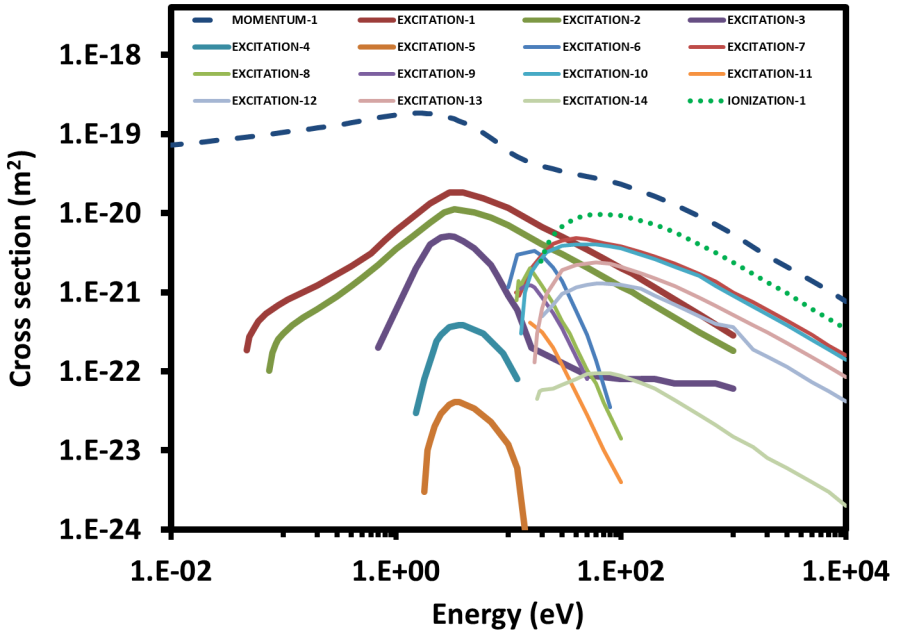

Figure 2.3: Collision cross section in m^2 for differnt energies for all 16 collision processes mentioned in Table 2.1 [33, 125].

efficiently it gets coupled to the plasma. The power given to the source of ROBIN is between 60 kW - 100 kW. Source/*driver* region absorbs only 10 % - 20 % of the given total power. The remaining power gets lost in the heating of various components, and some part of it gets reflected or radiated out. There are no accurate measurements of actual power that is finally coupled to the plasma. Instead of actually simulating the interaction of the RF field with the plasma, we apply a simple mechanism of RF power absorption and electron heating proposed in Refs. [23, 61]. Self-consistent electron heating is applied to sustain the plasma in the *driver* region. We assume that this power is uniformly absorbed in the "*driver*" region. The goal of heating is to balance electron-impact ionization in the discharge volume to the charged particle losses to the walls [23]. The power absorption leads to the Maxwellian velocity distribution. In the *driver* region, randomly selected electrons are heated at each time step Δt, the total energy of the electron during Δt in the *driver* increases by $P\Delta t$. Here, P is the absorption power to electrons for ionization. The heating temperature T_{heat} (increased due to absorbed power) is calculated at each time step using Eq. (2.8).

$$kT_{heat} = \frac{2}{3}\frac{1}{N_{eh}}\left[\sum_{i=1}^{N_{eh}}\frac{1}{2}m_e v_i^2 + P\Delta t\right] \tag{2.8}$$

where, k is Boltzmann constant, $N_{eh}(= N_T \nu_h dt)$ is number of heated electrons, N_T is number of electrons present in the *driver* at time $t + \Delta t$, ν_h is heating frequency, and v_i is velocity of the i^{th} electron before heating.

2.1.3 Numerical Constraints

PIC-MCC model has stringent numerical constraints, which depend on the temporal and spatial scales found in the system. In this case, plasma frequency ($\omega_p = \sqrt{ne^2/m\epsilon_0}$) and Debye length ($\lambda_D = \sqrt{\epsilon_0 kT/ne^2}$) needs to be resolved properly during the simulation [25, 66]. The temporal time step Δt is chosen such that it can resolve important time scales of the system and is generally given by Courant-Friedrichs-Lewy (CFL) condition.

$$\Delta t \leq \frac{0.2}{\omega_p} \tag{2.9}$$

where, ω_p is plasma frequency in Hz. Grid spacing ($\Delta X, \Delta Y$) less than electron Debye length (λ_D) and small time step (Δt) make simulations computationally expensive because of large plasma volume and long simulation times [16, 23]. The simulation must be performed until the steady state is reached. One more constraint of the PIC simulation is that the number of macro-particles (*superparticles*) per cell (PPC) must be significant to avoid numerical heating. According to [66], PPC must be greater than 10.

2.1.4 Computational Challenges

To accurately model and capture all the phenomena occurring during the experiment, simulation has to take care of the highest frequency (plasma frequency in our case) and smallest length scale (debye length or electron Larmor radius). Plasma density in such sources is 10^{18} m^{-3} leading to high plasma frequency. The electron Debye length (λ_D) is of the order of 10s of μm, much smaller than the source dimension (10s of cm). These requirements make PIC simulations computationally very expensive and challenging. There is a large number of computations due to calculations associated with the large number of particles in phase space. Mover and particle-to-grid interpolation are the most expensive part of the PIC-MCC model. The computational cost

for such code is decided by the number of computational particles, time step, number of grid points, and number of iterations (desired simulation/ physical time).

2.1.5 Scaling

One of the solutions to address the computational challenges (arising due to high plasma density, large source dimension, and strict constraints) mentioned above is to perform a simulation with low plasma density and use scaling laws to extrapolate the results, which provides similar results to the real condition. We have used scaling on plasma density. The Boltzmann equation for the charged species given in Eq. (2.1) is linear if collision term is linear (assuming only charged particle collisions with neutrals) and therefore Eq. (2.1) remain same after dividing f by a constant γ [61]. Dividing Eq. (2.1) by a constant γ and using Eq. (2.3), we wil get Eq. (2.10), where γ is scale factor. The scale factor is calculated using the ratio of the physical plasma density to the simulated plasma density [23, 61, 96, 137].

$$\frac{\partial f/\gamma}{\partial t} + v \cdot \frac{\partial f/\gamma}{\partial r} + \frac{dv}{dt} \cdot \frac{\partial f/\gamma}{\partial v} = \left(\frac{\partial f/\gamma}{\partial t}\right)_{colli} \tag{2.10}$$

The electric field remains invariant with scaled plasma density as seen in electron and ion momentum equations (Eq. (2.11)).

$$en_eE - J_e \times B = - \bigtriangledown P_e + m\nu_{en}J_e \tag{2.11}$$

where, J_e is electron current density, n_e is electron plasma density, P_e is electron pressure, and ν_{en} is the electron-neutral collision frequency. The linearity between the absorbed power and the plasma density used for scaling has been assumed. The properties of quasineutral plasma remain invariant with scaled number density. However, the sheath is affected by the scaling of plasma density, but as sheath voltage and plasma potential do not depend on plasma density hence, only sheath thickness will be modified. In the case of negative ion sources, the sheath thickness is much smaller than the discharge dimensions, and therefore the scaled simulation provides an

accurate description of the real problem. Besides density scaling, scaling to the source dimension [59, 60, 62], and to the vacuum permittivity [107, 108] are also applied in some previous work available in the literature.

2.2 1D studies of plasma transport

Simulations have been performed with experimental parameters obtained from the first phase of ROBIN negative ion source experiments. Details related to ROBIN source are described in Chapter 1, section 1.4. Plasma flow is in X-direction, therefore. X-dimension is scaled in this 1-D study. Numerical convergence studies of 1D-3V PIC-MCC code is given in section 2.2.1. Validation of model with experimental results are given in section 2.3.

2.2.1 Convergence studies using 1D-3V PIC-MCC code

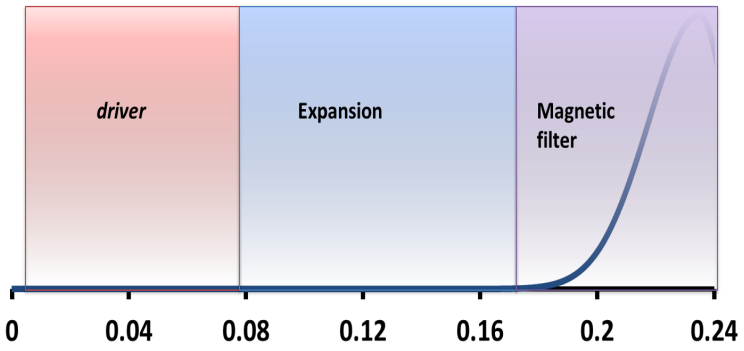

Figure 2.4: Simulation domain used for 1D-3V PIC-MCC simulation.

Parameter	Value	Remarks
X-dimension	0.24 m	
Gas Pressure	0.6 Pa	
power	60kW	Experimental
Electron energy	10 eV	output
Gas	H_2	
Ion energy	0.026 eV	
No of simulation particles	1×10^5	
No of real particles	0.2×10^{14} m^{-3}	Operational
No of species	2	parameter
Heating frequency	0.1×10^9 Hz	

Table 2.2: Parameter used for 1D-3V PIC-MCC simulations.

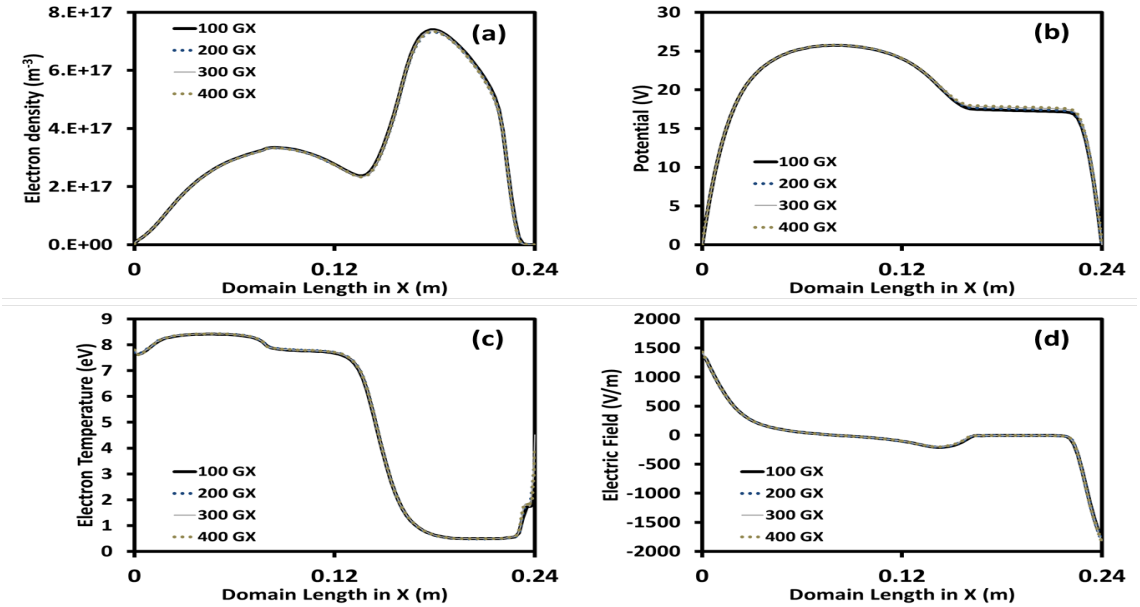

Figure 2.5: (a) plasma density (m^{-3}), (b) potential (V), (c) electron temperature (eV), and (d) electric field (V/m) using 1D-3V PIC-MCC simulation. Physical parameters are calculated for different number of grids (100 GX, 200 GX, 300 GX, and 400 GX). GX is for number of grids in X-direction. In this case, bias voltage is 0 V.

Simulation domain used for 1D-3V PIC-MCC model is shown in Fig. (2.4). Different regions (*driver*, expansion, magnetic filter) are shown in different colours (Fig. (2.4)). Simulation domain is in X-direction. Simulation parameters are provided in Table 2.2. Magnetic field for the convergence study is taken as 3 mT.

Convergence studies of 1D PIC-MCC simulation have been performed by changing spatial grid size and time steps. In figure (2.5), different physical parameters are shown for four different grid sizes with fixed time step ($\Delta t = 0.18 \times 10^{-9} s$). The grid size is varied by changing the number of grid points. Four different cases with different number of grid points (100 GX, 200 GX, 300 GX, and 400 GX) are considered. Studies are performed by obeying strict constraints ($\frac{\Delta t}{(0.2/\omega_p)}$) $\sim$ 0.23 and ΔX varied from 0.1 to 0.45 for different grid sizes). GX is the number of grid points in X. Physical parameters such as plasma density, potential, electron temperature, and electric field are shown in Fig. (2.5). Physical quantities, as shown in Fig. (2.5), remain the same in all cases. Bump in plasma density, fall in potential, and fall in electron temperature in the magnetic filter region are also captured in 1D simulations.

Figure (2.6) shows physical parameters from 1D PIC-MCC simulation for three

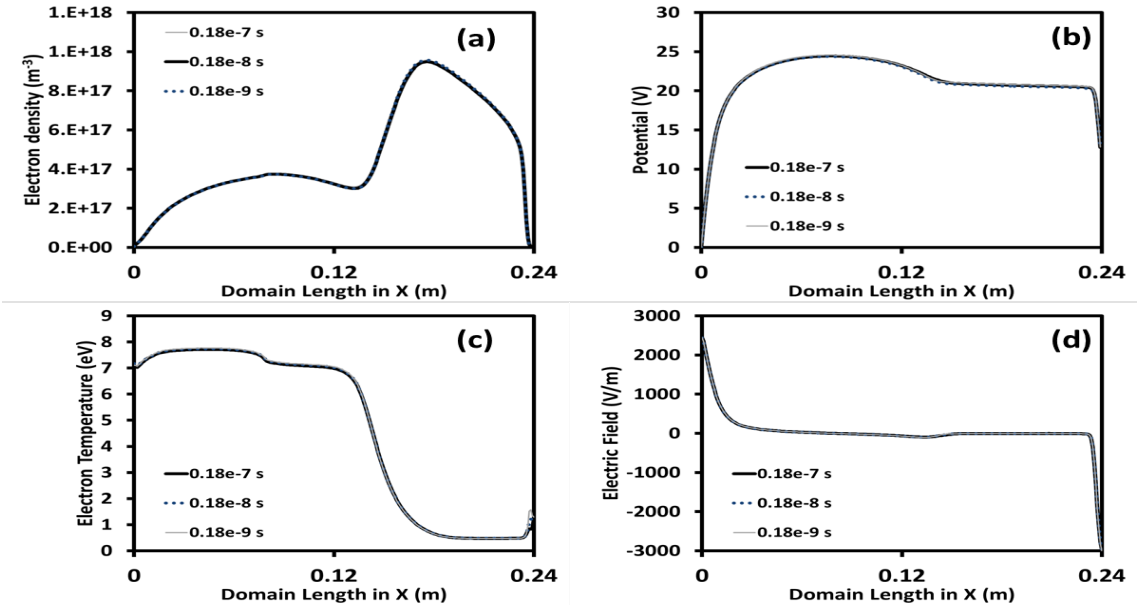

Figure 2.6: (a) plasma density (m^{-3}), (b) electron temperature (eV), (c) Electric field (V/m), and (d) potential (V) using 1D-3V PIC-MCC simulation. Physical parameters are calculated for different time steps (10^{-7} s,10^{-8} s, and10^{-9} s). In this case, bias voltage is 10 V.

different time steps (10^{-7} s, 10^{-8} s, and 10^{-9} s) with fixed number of grid points ($GX = 256$). In this case, also, plasma parameters remain the same for different time steps. In this case, $\Delta X \sim 0.18$ is taken, and $\frac{\Delta t}{(0.2/\omega_p)}$ varied from 23 to 0.23 for different time steps. This study shows that the developed 1D PIC-MCC code converges well with different grid sizes and time steps considered for this study.

2.3 Comparison of 1D-3V simulation and experimental results

We have taken the physical parameters (Table 1.1) from ROBIN ion source experiments to study the plasma transport across the magnetic field using the 1D-3V PIC-MCC model. 7 mT magnetic field is used in this particular case. Detailed simulation parameters are given in Table 2.2 and Table 2.3. Simulations have been performed considering all strict constraints given in [66] with $\frac{\Delta X}{\lambda_D} \sim 0.18$ and $\frac{\Delta t}{(0.2/\omega_p)} \sim 0.23$.

Comparison of plasma parameters from 1D-3V PIC-MCC simulations with ROBIN experiment results are shown in Fig. (2.7) and Fig. (2.8). We observe

Parameter	Value
ΔX	0.0009375 m
Δt	0.18×10^{-9} s
scale factor	5000
PPC	391

Table 2.3: Numerical parameters used for 1D-3V PIC-MCC simulations.

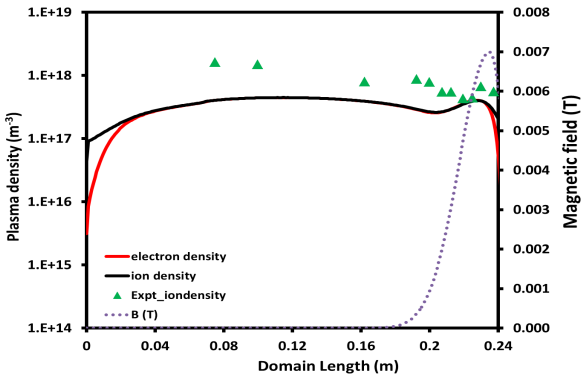

Figure 2.7: Plasma density in m^{-3} using 1D-3V PIC-MCC simulation. Dark solid lines are from simulations. Green triangle markers are ROBIN experiment results. The purple dotted line is the magnetic filter line.

similar trends (quantitative as well as qualitative) between the experimental and simulation results as shown in Fig. (2.7). Plasma obeys quasi neutrality inside the source but not near both boundaries. Ions have a large density at the boundaries compared to the electrons. Plasma density falls at the rise of the magnetic filter, and then a sudden jump is observed at the peak of the magnetic filter. These variations are visible in the plasma density data available from ROBIN experiments (green triangle markers in Fig. (2.7)). Such a jump in the plasma density at the peak of the Gaussian magnetic filter is also reported in different literature [23, 99, 137].

Yellow line and red triangle markers show electron temperature in eV in Fig. (2.8). Electron temperature drops in the magnetic filter region that is also visible in the experimental results (red triangle markers in Fig. (2.8)). The magnetic filter increases the electron's residence time due to cyclonic trapping. Electrons lose more energy due to collisions, and that results in a drop in the electron temperature in the magnetic filter. There is also a drop in the potential in the magnetic filter region. At the extraction boundary (boundary at the end of the magnetic filter), 0 V bias is applied. Potential in the plasma at the source and expansion region sustains at the plasma potential (near 21 V).

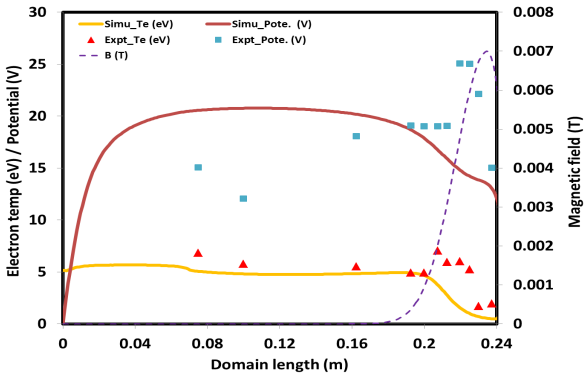

Figure 2.8: Electron temperature (yellow solid line) in eV and potential (red solid line) in V from 1D-3V PIC-MCC kinetic simulation. Blue square markers and red triangle markers are potential and electron temperature from the ROBIN experiment. The purple dashed line shows a magnetic field.

2.4 Conclusions

We presented a kinetic model to simulate the plasma transport across the magnetic field in low-temperature plasmas. The computational model (1D-3V PIC-MCC) has been validated using ROBIN negative ion source experimental results. Although not exactly similar, but we observe a good match between the 1D simulation and experimental results. The plasma density and electron temperature profile show similar quantitative behavior in both simulations as well as experiments. The bump in plasma density in both results in the magnetic filter region is due to the stacking of trapped electrons in the magnetic filter.

The mismatches between the ROBIN experiment and simulation results are due to the assumption made during simulations. Simulation is 1D, the effect of drifts and instabilities (occurs in real experiments) are not present in the simulations. We have considered simple hydrogen chemistry. However, even with several limitations, we find that 1D-3V PIC-MCC simulations can predict plasma behavior in such LTP experiments with acceptable accuracy. Our analysis shows that an advanced 2D-3V PIC-MCC model is required for a complete understanding of the physics of plasma transport across the magnetic filter.

CHAPTER 3

Development of parallel 2D-3V PIC-MCC codes for Multi-core (CPU) and Manycore (GPU) architectures

As discussed in the previous chapter (Chapter 2), 1D model cannot accurately capture the real experimental scenario. A 2D or 3D model is necessary to understand the detailed physics of drifts and instabilities. However, 2D-3V PIC-MCC model is computationally very expensive and that necessities the development of parallel 2D-3V PIC-MCC code to bring down run-time to desirable limit. In this chapter, we have discussed about the development of 2D-3V PIC-MCC code, the different parallelization strategies for different computing architectures and analysis of speedup for different problem sizes. Simulation domain, considered for this study, takes into account 2-D displacements of particles in X-Y plane with 3 velocity components under the influence of an externally applied magnetic field (B_z) perpendicular to the simulation domain (in Z direction with Gaussian shape variation in X direction [23]). The spatial grid size in the computational domain is small enough to resolve the important physical length scales such as electron Debye length. Temporal time steps are chosen such that it can resolve important time scales of the system and is generally given by Courant-Friedrichs-Lewy (CFL) condition $\Delta t \leq \frac{0.2}{\omega_p}$.

Organization of the chapter

This chapter is divided into three parts: serial implementation of 2D-3V PIC-MCC code (section 3.1), parallelization for CPU architecture (section 3.2) and parallelization strategies for GPU (many core) architecture (section 3.3). Section 3.2 is divided into two parts: (1) shared memory (OpenMP) parallelization (section 3.2.2) and (2) Hybrid (OpenMP + MPI) parallelization (section 3.2.3). Results from different computational experiments are provided in section 3.2.4. Detailed overview of CUDA environment and Kepler architecture is given in section 3.3.1, different parallelization strategies with optimization techniques are summarized in section 3.3.2, and results of GPU parallelization are provided in section 3.3.3.

3.1 Implementation of serial 2D-3V PIC-MCC code

3.1.1 Data Structures

There are two essential groups of quantities associated with PIC simulations: Particle quantities and Grid quantities. As explained earlier, the particle to grid interpolations (for charge deposition) and the grid to particle interpolations (for moving the particles) are performed extensively. Hence, these quantities interact with each other very often.

In our 2D-3V PIC code, for a specific computational particle representing many actual particles, particle quantities are the phase space information (position and velocity vectors) of that particle along with an identifier describing the species of that particle (electron or ion). These quantities are grouped into a structure which is named as *Particle* and to keep track of these quantities for every particle, an array of *Particle* structure is used as shown in Fig. (3.1-c).

Quantities such as charge density, potential, electric field, magnetic field have been discretized over the 2D grid. Since these quantities are recorded for every grid point, we have called them grid quantities. Each grid point has two components of electric field, one along X and the other along Y direction. Hence, electric field information is stored in a structure for a particular grid point and an array of these structures is used to maintain the information of

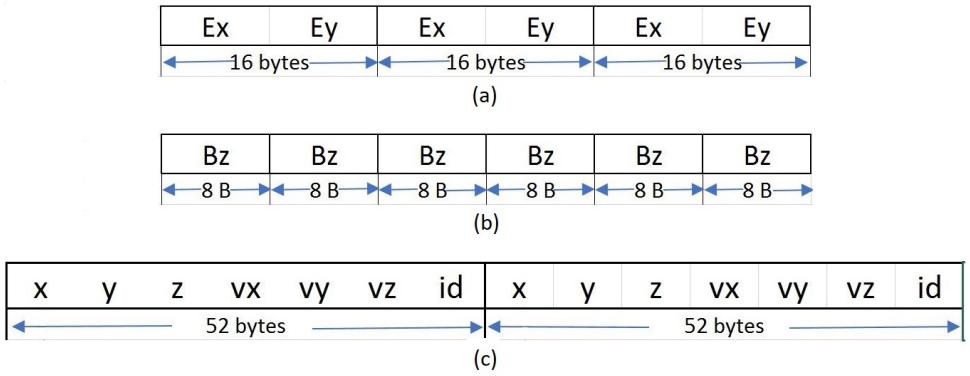

Figure 3.1: Visualization of particle and grid data structures. (a) Electric field components are stored as an array of structure. (b) Magnetic field has only one component, so it is stored in an array. (c) Every particle has their own phase space information and hence, it is stored as an array of structure.

electric field for the whole grid. The magnetic field for our simulation purpose has been kept varying only in the Z direction. Hence, only the array of values is needed to keep track of magnetic field over all grid points. Same is the case for charge density and electric potential. All the quantities (particle and grid) are stored as double precision floating point values during the simulation. An important point to note here is that even though the grid quantities are over the grid points of a 2D grid, but when storing it as an array, we have used just a 1D array rather than using the 2D array (array of arrays) [133].

3.1.2 Arithmetic Intensity

Arithmetic intensity of a section of code (or subroutine) is the ratio of the number of computations performed to the number of bytes transferred from/to memory in that code section and gives an idea about whether the section (module or subroutine) is compute or memory bound. From the Fig. (3.2), we can see that the most of the simulation time goes into *Charge deposition* and *Mover* module. Hence, the important subroutines are *charge deposition* and *mover*. The arithmetic intensity of these important subroutines are presented in Table 3.1 and from that we can see that both *Mover* and *Charge deposition* are memory bound.

Mover needs to load 6 phase space values of 8 bytes each and another 4 bytes are needed to identify the type of particle – id attribute of Particle structure as shown in Fig. (3.1-c). Based on the type of particle, we have to fetch the charge

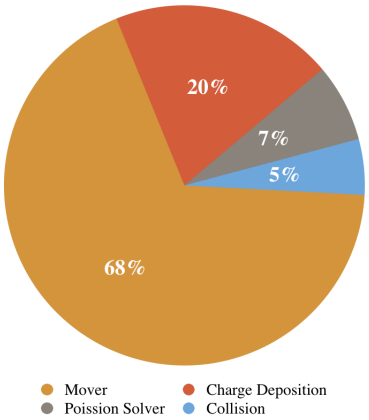

Figure 3.2: The contribution of different modules/subroutines towards the total run-time of the serial code for a typical simulation (moderate problem size). Grid size of 1024 $\times$ 1024 with 20 PPC density simulation. Executed on a single core of Intel Xeon E5-2630 v3 with 64 GB of DDR3 RAM. *Mover* and *Charge Deposition* prevail the the overall execution time.

to mass ratio for that particle which requires 8 bytes to be fetched. 12 values corresponding to E_x, E_y and B_z on four cell corners (8 bytes each) are read to interpolate the fields on to the particles as shown in Fig. (3.3). Finally, all the 6 phase space values are updated (8 bytes each). The rest of the data is for keeping track of the different particle types and their start index in the particle data structure.

In *Charge Deposition*, x and y coordinates of the particle along with an identifier for the type of particle is loaded (20 bytes total). Weighing factor (8 bytes) is required to balance the charge density against the actual number of particles. Finally, the charge density is loaded (8 bytes each) and updated (8 bytes each) on all the four cell corners. Rest of the data is used for book keeping.

	Mover	CD
Double-precision operations (FLOP)	91	19
Double-precision Read/Write (Byte)	204	92
Arithmetic Intensity (FLOP/Byte)	0.446	0.206

Table 3.1: Arithmetic Intensity (ratio of number of computations to the number of bytes transferred from/to memory)

3.1.3 2D Interpolation Scheme

As mentioned in Chapter 2 section 2.1-B, linear interpolation is applied to calculate particle to grid or grid to particle interpolation in 2D-3V PIC-MCC

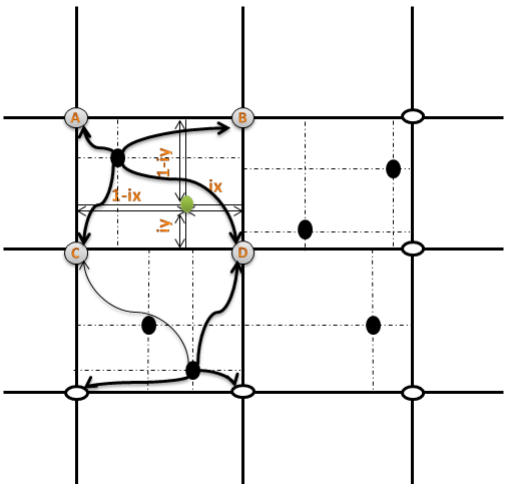

Figure 3.3: Charge density assignment on grid points using linear interpolation. A, B, C and, D are grid points on the 2-D simulation grid. Green and black circles are particles inside different grid cells.

model. In 2D, interpolation scheme is explained in Fig. (3.3). For example, contribution of a particle (shown in green circle in Fig. (3.3)) towards charge density on four different grid points A, B, C, and D are calculated using the following equations,

$$\rho_A = \rho_A + q\left(\frac{ix \cdot iy}{\Delta X^2 \cdot \Delta Y^2}\right) \tag{3.1}$$

$$\rho_B = \rho_B + q\left(\frac{(1-ix) \cdot iy}{\Delta X^2 \cdot \Delta Y^2}\right) \tag{3.2}$$

$$\rho_C = \rho_C + q\left(\frac{ix \cdot (1-iy)}{\Delta X^2 \cdot \Delta Y^2}\right) \tag{3.3}$$

$$\rho_D = \rho_D + q\left(\frac{(1-ix) \cdot (1-iy)}{\Delta X^2 \cdot \Delta Y^2}\right) \tag{3.4}$$

where ΔX and ΔY are grid sizes, and ix, iy are fractional distances of particle from the cell origin in the X and Y direction, respectively.

3.1.4 Renormalization

Renormalization technique is applied to balance plasma particle growth with the limitation of computer memory. Ionization and re-injection increase plasma particles during simulation. If computational particles increase to

some percentage of the initial computational particles, computational particles are lowered again and empty the computer memory.

3.1.5 Profiling of Serial Code

The contribution of different sections/subroutines towards the total run-time of the serial code for a typical case has been presented in Fig. (3.2). The simulation was performed on a grid of 1024×1024 with 20 number of particle per cell (PPC) and the code was executed on a single core of Intel Xeon E5-2630 v3 clocked at 2.4 GHz with 64 GB of DDR3 RAM. From the Fig. (3.2), it is clear that *Mover* and *Charge Deposition* consumes a lot of time (about 88%). Note that, 5% and 7% of the total time is taken by MCC and Poisson Solver respectively, which is less in comparison to *Mover* and *Charge Deposition*.

3.2 Shared memory (OpenMP) and Hybrid (OpenMP + MPI) parallelization

3.2.1 Hardware and Programming Frameworks

Large scale highly parallel systems based on shared memory architectures are dominant computing platforms that give rise to many different parallel programming paradigms. **OpenMP** is a popular API for parallel programming on shared memory architecture. It uses a set of compiler directives (pragmas), library routines, and environment variables to specify multi-threaded execution of the code. On distributed memory systems, **MPI** is widely used for writing message passing programs across nodes of a cluster. OpenMP based code can be also ported to emerging many-core architectures such as Intel Xeon-Phi [144]. Xeon Phi is a series of many-core processors. This vector processor has 256 bit wide SIMD (Single Instruction Multiple Data) registers and multiple cores. Its special vector processor helps in doing SIMD instructions faster. Depending on the version, it can do 4 or 8 double precision operations in the same time as a single operation on conventional processors. It supports four way multi-threading and has high bandwidth for on chip data access, which brings down latency to a great extent.

	Reference	Bench 1	Bench 2	Bench 3	Bench 4
CPU	Intel i5-4210U Processor	Intel Xeon 2630, 2 sockets **(Xeon)**	Intel Xeon Phi 5110P Co-processor **(Phi 5)**	Intel Xeon Phi 7250 Processor **(Phi 7)**	4 node cluster : 2 Intel processor (E5-2640) / node
Frequency (GHz)	1.70	2.40	1.053	1.40	2.60
Cores	2	16	60	68	64
L2 size (MB)	0.25 (per core)	0.25 (per core)	30 (shared)	34 (shared)	-
L3 size (MB)	1.5 (per core)	20 (shared)	-	-	20 (shared)
Peak Memory Bandwidth (GB/s)	25.6 (2 channels)	59 (4 channels)	320 (16 channels)	115.2 (6 channels)	25.6 (2 channels)

Table 3.2: Specifications of the platforms used in our computational investigation. The compilation was done through the Intel Compiler 16.0.3 on all architectures. The compilation requires -fopenmp, -lpthread, -lm and -ldl flags. Other flags included are libiomp5.a, libmkl_blacs_openmpi_ilp64.a

For small problem sizes, researchers generally use an OpenMP based code, however for bigger problem sizes and better accuracy we need hybrid codes. Thus, a combination of shared memory and message passing parallelization paradigms within the same application, often known as hybrid programming, is expected to provide more efficient parallelization strategy for clusters of shared memory nodes. The **hybrid OpenMP + MPI** programming refers to a programming style in which communication between nodes is handled by MPI processes and each MPI process has several OpenMP threads running inside to occupy the CPUs for computation.

Table 3.2 shows the four test benches which have been used in our work. The reference benchmark is a standard standalone CPU with 2 cores. But the hardware limitations of this CPU limits the grid sizes for which our simulation can be run. Thus, the serial code is parallelized using OpenMP and a high degree of thread level parallelism is achieved when it is run on the many-core architecture of the Intel Xeon Phi processors. When we develop the hybrid code, we run it on the 4 node cluster with shared memory multi-core processors, such that we get advantage of node-level parallelism as well.

The parallelization of PIC code serves as a major research problem in the area of High Performance Computing. The earliest works on parallelizing the PIC codes were designed for distributed memory systems. The nodes simply communicate using message passing, no shared memory is available to take advantage of thread level parallelism [127]. This approach does not scale for larger problem sizes [44]. With the advancements of shared memory parallelism, researchers tried to implement PIC code using OpenMP library. This method also suffers from similar problem of scalability [46].

Newer methods for parallelizing PIC codes are based on distributed systems with shared memory parallelization in each node. This system uses the hybrid MPI + OpenMP programming technique which is the focus of this chapter. There are two ways in which hybrid parallelization is achieved. These are particle and grid based decomposition.

The particle-based decomposition is widely used because of its easy implementation and near perfect load balance [46]. The hybrid programming paradigm used in this chapter implements OpenMP based thread level shared memory parallelization inside MPI based node level processes, i.e., each MPI node has a fixed number of OpenMP threads and which communicate among MPI processes outside the parallel region.

The grid-based decomposition is based on sharing a part of grid among different nodes rather than the particles. This method suffers from the problem of load balancing as it is difficult to ensure that the particles are distributed equally among all nodes. A similar method consisting of very fine-grain domain decomposition referred to as patch-based decomposition has also been used in recent works [46], where patches denote very small sub domains. This method is an extension of grid-based decomposition.

3.2.2 Shared Memory (OpenMP) Parallelization Strategy

Parallelization of *Charge deposition* Module

There are two different strategies which can be used to parallelize the *Charge Deposition* module.

1) Dividing the rows of the grid equally among the threads. The interpolations of all the particles lying in one region will be done by the thread which is assigned that region. If each thread shares the entire grid then the two threads having common grid points along the common rows are vulnerable to race conditions. Therefore we must give each thread an exclusive portion of the whole grid. To get a consistent view of grid quantities, we need to aggregate the grid quantities shared between two threads at the boundary. Due to the continuous movement of the particles in the computational domain, it is very likely that there are an unequal number of particles across the different areas of the grid and hence an unequal number of particles per thread which may lead to **uneven load balancing**. Moreover, each thread must know exactly the particles that are lying in the region assigned to it, along with the location of those particles in the array of particles. To do this efficiently, the particles lying in one region have to be grouped together in the array of particles. The start and end index of that group has to be calculated. This grouping has to be done after every iteration since the particles will be moving continuously throughout the simulation. Doing this at every iteration introduces extra overhead and complexity.

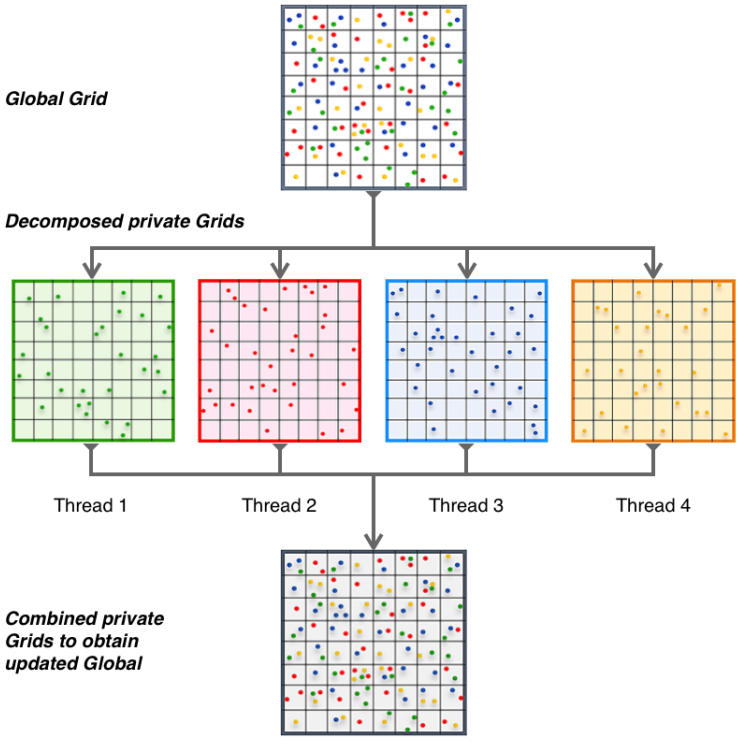

Figure 3.4: Parallelization strategy for Charge Deposition module.

2) Dividing equal number of particles among the threads. This strategy is motivated by the Principle of Superposition. Since the interpolations in this module applies as particle-to-grid, the race conditions may arise when two different particles handled by two different threads try to update the grid quantities pertaining to the same grid point simultaneously. In order to avoid race conditions we shall assign each thread a private copy of the global grid as portrayed in Fig. (3.4). This ensures that each thread works independently on its share of particles without any critical region or requirement for locks. Once the threads have done their share of calculating grid quantities on their own private grids, we aggregate all the private grids to get back the global grid. This strategy involves the overhead of generating private grids for each thread. Synchronization is straightforward.

Out of these two strategies, the second approach would result in efficient load balancing among all the threads as compared to the first one. Also, if we increase the problem size, the latter strategy is scalable since the time taken to synchronize the whole grid is negligible compared to the time taken to perform particle to grid interpolations.

We have used the second strategy in our implementation and the following is the **pseudo-code for parallel execution of charge deposition module**.

```
1   void chargeDeposition()
2       GridQty *private_grid_qty = malloc(no_of_threads * \\
3       GRID_DIMENSIONS);
4       /* Parallelization over particles using private grids */
5       #pragma omp parallel for
6       for(i = 0; i < total_particles; i++)
7           int id = omp_get_thread_num();
8           /* Position of neighboring grid points */
9           double x1, y1, x2, y2, x3, y3, x4, y4;
10          /* Calculate the position of neighboring grid points
11          based on the position information from particle_array[i] */
12          double update1, update2, update3, update4; /* Updates */
13          /* Calculate the value of updates */
14          /* Update the private grid quantity's value at nearby grid
15          points */
16          private_grid_qty[id * GRID_DIMENSIONS + x1 * Nx + y1] +=
17          update1;
```

```
            private_grid_qty[id * GRID_DIMENSIONS + x2 * Nx + y2] +=
            update2;
            private_grid_qty[id * GRID_DIMENSIONS + x3 * Nx + y3] +=
            update3;
            private_grid_qty[id * GRID_DIMENSIONS + x4 * Nx + y4] +=
            update4;
        /* Combine the private grids to form the updated global
        (Synchronization) */
        for(i = 0; i < no_of_threads; i++)
            for(j = 0; j < Nx * Ny; j++)
                global_grid[j] = private_grid_qty[i * GRID_DIMENSIONS
                + j];

```

Parallelization of Mover Module

The *Mover* subroutine can be parallelized by dividing the particles equally among the threads. In this subroutine, the interpolations are performed from the grid to particle. Since particles are divided among the threads, a particular particle's phase space information is updated only once by one thread and to do that update, the thread has to just read the grid quantities. Therefore, there will be no race conditions while updating the phase space information of particles in parallel. Hence, this is an embarrassingly-parallel challenge. Moreover, dividing particles equally among the threads will lead to efficient load balancing with a straightforward implementation using static scheduling.

```
    void mover()
        /* Parallelization over particles using private grids */
        #pragma omp parallel for
        for(i = 0; i < total_particles; i++)
            double updateX, updateY; /* Updates in position */
            double updateVx, updateVy, updateVz; /* Updates in
            velocities */
            /* Calculate the value of updates based on the value of
            grid quantities at neighboring grid points */
            /* Update the phase space information at particle_array[i] */
            particles_array[i].x += updateX; particles_array[i].y
            += updateY;
            particles_array[i].vx += updateVx; particles_array[i].vy
```

```
14              += updateVy;
15              particles_array[i].vz += updateVz;
16
```

Sorting

It has been well established that sorting significantly increases simulation speeds of PIC and eliminates cache thrashing [29]. Cache thrashing occurs while interpolation of quantities from the grid to particles and particles to the grid. If the particle array is sorted based on their positions in the grid, the grid quantities are no more accessed randomly, and hence this strategy successfully achieves cache re-usability.

We performed experiments on different architectures to inspect when sorting leads to increase in speedup. The results can be seen in Fig. (3.5-a). For processors with smaller cache sizes, the grid data structures used in the simulation cannot fit in the cache completely and thus, sorting helps in improving their performance. But for systems with very large cache size like in the Intel Xeon Phi co-processors and those commonly used today, the grid data structures are able to easily fit in the cache. Thus, sorting adds unnecessary overhead in this case and leads to lower speed up than expected. Therefore, we are not sorting the particles before the charge deposition module.

	Serial	Parallel
Xeon	88.24	76.22
Phi 7	95.66	86.88

Table 3.3: Cache hit rate comparison (perf analysis). This observation is in accordance with the fact that Phi-7 architecture has a significantly larger cache than the Xeon architecture.

The numerical results in Fig. (3.5) and the supporting figures have been obtained through guidelines laid down by Hoefller [86]. For analyzing the behavior of strategies on varying architectures, we chose a base architecture (Intel i5) to act as a common reference.

There is an extensive variation in the sequential code execution time of the architectures that we have considered for analysis. The values range from 140 seconds on Intel Xeon E5-2630 **(Xeon)**, 386 seconds on Intel i5, 971 seconds

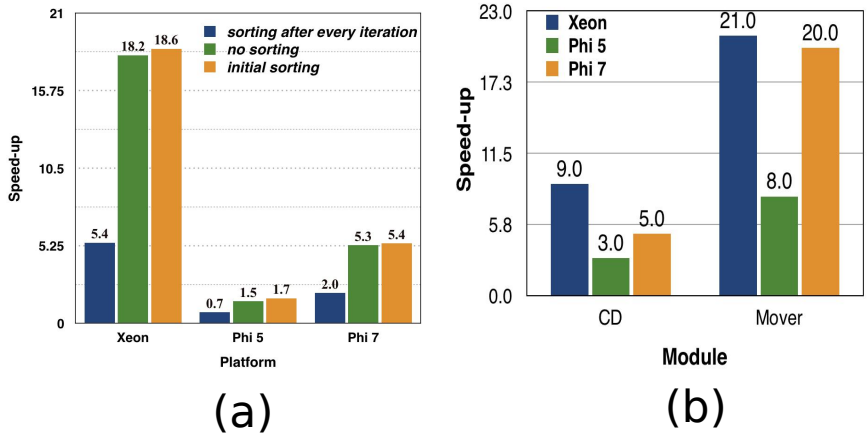

Figure 3.5: (a) Strategy-wise maximum speed-up of optimized parallel execution on 3 different architectures relative to a non-sorted serial execution on the Intel i5 processor. (b) Module-wise maximum speed-up on selected architectures (different number of threads on different architectures). This value is calculated relative to a serial execution on an Intel i5 based machine.

on Intel Xeon Phi 7250 **(Phi 7)** and 3892 seconds on Intel Xeon Phi 5110p **(Phi 5)**. The simulation corresponds to a physical time of 18 ns on a square grid of 128-128 partitions with a density of 20 PPC. Due to this significant difference in the serial processing power; theoretically, a perfectly parallel code executed on Xeon Phi 5110p with 28 cores will perform at par with the same serial version executed on E5-2630.

Xeon Phi has a more primitive prefetching, slower clock frequency, in-order processing, a smaller pipeline, one instruction per two cycles etc. Therefore, the key to best performance is doing the best optimization in all the three aspects: vectorization, parallelization, and memory utilization. The under-performance of our execution can be explained through the very low vectorization potential of the PIC algorithm as supported by the arithmetic intensity values in Table 3.1. This explains why the scalar code running on a single thread of Xeon Phi is slower than scalar code running on a Xeon. This is a problem because the scalar unit of Phi 5 is quite under-powered, both for itself and relative to modern processors. This was improved in the Phi 7 but it still remains slower in comparison with the multi-core Xeon.

Inferring from the values in Fig. (3.5-b), the performance of the overall optimization is significantly specific to the features and ability of the hardware.

The clock speed of a single processor, cache size and cores are among the major contributors in shaping of the above results.

3.2.3 Hybrid Parallelization Strategy

For system architectures enabled for hybrid parallelization, we can make use of multiple nodes connected to each other via the network. We use the MPI library to enable communication between the nodes (*Node-level parallelism*). Each node has a specific number of cores and each core, in turn, is capable of launching hardware threads (*Thread level parallelism*).

Let us revisit the parallelization strategies discussed in above section to extend them to the hybrid implementation. The parallelization of the *Charge Deposition* module has been achieved using OpenMP. The particles are equally divided among the OpenMP threads and each thread has its own private copy of the grid quantities to avoid race conditions when performing particle to grid interpolation. Once all the OpenMP threads have updated their private copies of the grid quantities, these private copies are aggregated to get the updated global grid. This ensures that the grid quantities are consistent before and after the *Mover* module is executed. For the parallelization of the *Mover* module, the particles are equally divided among the OpenMP threads, as a solution to an embarrassingly parallel sub-problem.

The hybrid parallelization strategy naturally builds from the strategy used for thread level parallelization which is summarized above. At the beginning of the simulation, the particles are equally divided among the nodes as shown in the Level 1 parallelization of Fig. (3.6). Each node is responsible for executing the *Charge deposition* and *Mover* module for the set of particles that are assigned/private to that node. Since the particles are divided among nodes, each node is required to have its own private copy of the grid in order to avoid race conditions with the other nodes during the *Charge deposition* subroutine. After the execution of the *Charge deposition* module, the private copies of each node must be aggregated to get consistent view of grid quantities on global level.

Since each node has multiple cores, it shall execute the thread level

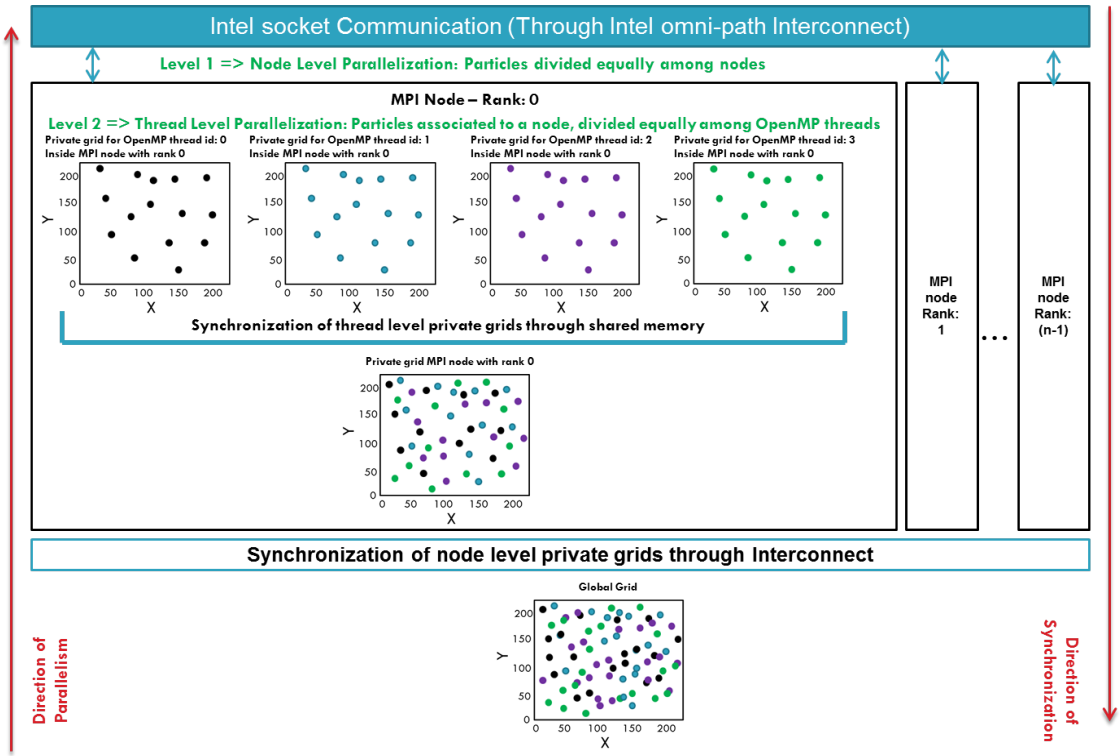

Figure 3.6: Visualization of the hybrid parallelization strategy. Level 1 (node-level parallelization): Particle distribution per node and the aggregation of private grids of all nodes and Level 2 (thread level parallelization inside a node): Further distribution of particles of a node per thread and the synchronization of private grids per thread to get a consistent private grid per node

parallelization strategy explained in above section for the *Charge Deposition* module for the particles assigned to that node to get the updated node-level grid quantities. Once each node has its own private copy of grid quantities updated, each node takes part in the global node-level aggregation of the grid quantities through its own private grid quantities.

For this global aggregation, each node must use the network and communicate to every other node its private copy of grid quantities. Post this communication between nodes, the grid quantities are consistent among all the private node grids. Since, this aggregation takes place over the network, it is expensive communication. It is important to reduce this cost, by optimizing it using the `MPI_Allreduce` function provided by MPI library.

Pseudo-code of Hybrid Parallelization Strategy

At the beginning of the PIC simulation, the data about initial conditions of the simulation is read from a file. That file contains information about the total number of computational particles in the simulation. Each MPI node reads the file and is allotted the number of particles that it is supposed to handle as follows:

```
int particles_for_this_node = total_particles / MPI_WORLD_SIZE
if (mpi_world_rank == MPI_WORLD_SIZE - 1):
    particles_for_this_node += (total_particles % MPI_WORLD_SIZE)
/* Memory allocations for the Particle array based on
the total number of particles assigned to this node */
Particle *particle_array = malloc(particles_for_this_node)
/* Memory allocations for private grids */
GridQty1 *private_grid_qty_1 = malloc(GRID_DIMENSIONS)
GridQty2 *private_grid_qty_2 = malloc(GRID_DIMENSIONS)
...
GridQtyN *private_grid_qty_n = malloc(GRID_DIMENSIONS)
/* Other initializations */

```

Once these initialization are complete, each node enters the simulation loop. The pseudo-code for the simulation loop is as follows:

```
while (simulation_not_over):
    /* Execution of charge deposition module,
```

```
        using the thread level parallelization */
        chargeDeposition();
        /* Global synchronization of private node-level copies
        of grid quantities */
        MPI_Allreduce(private_grid_qty_1, ...)
        MPI_Allreduce(private_grid_qty_2, ...)
        ...
        MPI_Allreduce(private_grid_qty_n, ...)
        /* After the call to Allreduce, each node has
        consistent view of grid quantities */
        /* Execution of mover module using the thread level
        parallelization */
        mover(grid_qty)
        /* Other modules of the PIC simulation */

```

3.2.4 Results of shared memory parallilization

As the grid size increases, while keeping the Particle Per Cell (PPC) value constant, then the number of particles also increases. Therefore, the memory consumption also increases for both grid and particle data structures. In the Table 3.4, we have reported the memory consumption of grid data structures used to store electric and magnetic fields, and the memory consumption of the particle data structure. Similar amount of memory is also used for other grid based data structures such as electron number density, ion number density, charge density, energy and potential. The memory taken by one element of the respective data structure is reported in the section 3.1.1. It is evident from the first column of the Table 3.4 that the memory needed to store the array of particles increases drastically as we increase the grid size.

The biggest advantage of our hybrid parallelization strategy is in terms of memory consumption. Since the particles are divided equally among the nodes, even if we increase the grid size, the memory used to store all the particles would increase but it would be less per node when compared to the OpenMP parallelization strategy in which the array of particles would have been stored in just one node. This analysis is shown in the Table 3.4.

As we can see from Table 3.5, if we keep the number of nodes fixed, then the

Grid size	OpenMP with 4 cores			Hybrid with 4 nodes, 4 core each			Hybrid with 8 nodes, 4 core each		
	Particle array size (MB)	EF array size (MB)	MF array size (MB)	Particle array size (MB)	EF array size (MB)	MF array size (MB)	Particle array size (MB)	EF array size (MB)	MF array size (MB)
512x512	1040	4	2	260	4	2	130	4	2
1024x1024	4160	16	4	1040	16	4	520	16	4
2048x2048	16640	64	16	4160	64	16	2080	64	16

Table 3.4: Memory consumed in MBs by the particle and grid data structures - Electric Field (EF) and Magnetic Field (MF) per each MPI node - in the parallelization achieved using OpenMP and the hybrid parallelization strategy for different problem size and fixed particle per cell(PPC) value of 80.

Grid size	Speedup for 40 PPC		Speedup for 80 PPC	
	Hybrid 4 nodes, 4 cores per node	Hybrid 8 nodes, 4 cores per node	Hybrid 4 nodes, 4 cores per node	Hybrid 8 nodes, 4 cores per node
512 x 512	2.42	3.46	2.69	4.51
1024 x 1024	3.13	4.92	3.82	6.16
2048 x 2048	3.35	5.57	3.00	7.00

Table 3.5: Comparison of the speedup for hybrid system with different number of MPI nodes for 100 iterations of the simulation with different grid sizes and particle per cell(PPC) values. Here, Speedup = execution time of OpenMP based code on a multi-core processor with 4 cores (Bench 1) / execution time of corresponding hybrid system (Bench 4)

speedup increases when we increase the problem size, i.e., increasing the grid size and/or increasing the PPC. Also, for large problem sizes, increasing the number of cores/node leads to increase in the speedup indicating the code scales well for architectures with many nodes or cores/node. One reason for this is that as we increase the problem size, the aggregation of the node-level private copy of grid quantities through `MPI_Allreduce` takes negligible time compared to the time taken in performing extensive interpolations for a large number of particles per node.

As shown in the Fig. (3.2), the *Poisson Solver* and *Collision* modules take negligible fraction of time out of the whole computation time. Therefore, we have only reported the speedup for the *Mover* module in Table 3.6. As can be seen from the Table 3.6, for large problem sizes, the *Mover* module give super-linear speedup (marginally), suggesting that they are able to efficiently

Grid size	Speedup – Mover	
	Hybrid 16 cores	Hybrid 32 cores
512x512	4.14	8.24
1024x1024	4.73	10.02
2048x2048	4.44	9.37

Table 3.6: Speedup of the Mover module for the hybrid code with different number of cores and different problem size and fixed PPC value of 80. Here, Speedup = execution time of OpenMP based code on a multi-core processor with 4 cores (Bench 1) / execution time of corresponding hybrid system (Bench 4)

use the (combined) cache compared to the OpenMP implementation.

Also, from the results of Table 3.6, one can see that the speedup is maximum when the grid size is 1024×1024 and the speedup for 2048×2048 is lesser than that when grid size is 1024×1024. One plausible explanation for this is that as we increase the grid size, after a point, it is not possible to accommodate the entire electric and magnetic field's grid in the cache, as can be observed from Table 3.4. For the specific case of 1024×1024 grid size, the grids barely fit in the cache for the hybrid code as well as OpenMP code, but the cache utilization for this specific grid size is much more significant for hybrid code than its OpenMP counterpart.

3.3 GPU (manycore) parallelization

3.3.1 Overview of CUDA Environment and Kepler Architecture

GPUs provide an excellent and a cost effective way of parallelizing computationally intensive simulations. Nowadays, GPUs have thousands of cores, and they offer TFLOPS of compute performance. Compute Unified Device Architecture (CUDA) is an API developed by Nvidia for the application developers to harness the power of thousands of cores. In order to make the task of porting a serial code to the GPU easier, CUDA provides a layer of abstraction over the underlying GPU hardware. Computationally expensive subroutines can be declared in a separate function (called a kernel) so that it

can be executed by each thread on the GPU. Threads are logically arranged in thread blocks, which in turn are arranged in grids (not to be confused with our simulation grid) to make the mapping of threads to data easier. However, on the GPU hardware, threads are scheduled in the batch of 32 threads (called a warp). CUDA allows the programmer to manage different types of memory, such as shared, texture, constant and global, offered by a modern day GPU.

Kepler architecture provides notable improvements over Fermi architecture which are of specific interest to us. First of all, global memory atomic operations are 9x faster on Kepler architecture as compared to Fermi architecture [69]. We use atomic operations in the *Charge Deposition* subroutine to perform particle-to-grid interpolations. Such a significant improvement in the performance of atomic operations will be helpful. Kepler-based GPU offers a 2$\times$ large last level L2 cache [69]. This will be beneficial for the Sort-Shuffle parallelization strategy that is discussed in section 3.3.2. A larger L2 cache will help both *Mover* and *Charge Deposition* to cache more grid-based data structures such as potential, charge density, electric and magnetic fields. GPUs with compute capability 3$\times$ or more can launch more than 2 billion thread blocks in a single dimension as opposed to an earlier limit of 65535 [69]. That, in turn, translates to the easier mapping of threads to particles. Earlier, if the number of particles were too large, we were required to launch a 2D or 3D grid of thread blocks and map it to the particles data structure which is one dimensional. Finally, Kepler architecture brings shuffle instruction to perform intra-warp communication [69, 45]. Shuffle instruction can be used to perform operations such as reduction directly within the warp without the need of auxiliary space in shared memory. Shuffle instruction directly accesses data from the other thread's register, and hence it is 1.5$\times$ faster than shared memory [69]. We have used Shuffle to perform fast parallel reduction for *Charge Deposition* in the section 3.3.2 [94].

3.3.2 Parallelization Strategies and Optimization Techniques

The overall speedup of a parallel code mainly depends on the efficient parallelization of the most expensive sub-routines, and in this case, *Mover* and *Charge Deposition* in the serial code takes the maximum amount of execution

time (around 88%). Therefore we have focused mainly on the efficient parallelization of the *Mover* and *Charge Deposition* modules for our GPU-based PIC code. Poisson Solver in the GPU code has been kept unchanged and has been implemented on CPU using PARDISO [122, 123]. However, multiple CPU cores are made available to the PARDISO solver during the execution of the GPU code (by setting the environment variable OMP_NUM_THREADS=4 in the case of Xeon E5). The following sub-sections are arranged in such a way that each strategy builds upon the previous one with incremental improvements.

Strategy 1: Naive

Starting from compute capability 3.$\times$, a CUDA kernel can be launched with a one-dimensional grid with 2147483647 thread blocks, and therefore it is possible to launch billions of threads simultaneously on a GPU. Keeping this in mind, each computational particle in *Mover* has been assigned to a thread, and therefore a total number of threads is determined by the number of computational particles. Similarly, in *Charge Deposition* each thread is assigned a particle to deposit the charge on neighboring four grid points. There are two major caveats in this Naive strategy. First of all, the memory access to the particles data structure is uncoalesced. Strategy-2 and sorting subroutine from strategy-3 makes all the memory accesses in the *Mover* coalesced. Secondly, in *Charge Deposition* each thread deposits charge on the four cell corners using global atomics. Also, the particles are not spatially close enough, as shown in Fig. (3.9-a). Hence, it results in poor utilization of device memory due to the use of global atomics. The strategy discussed in section 3.3.2 vastly improves upon this problem using a CUDA intrinsic called shuffle.

Strategy 2: Coalesce

In the case of *Mover* and *Charge Deposition*, threads are mapped to particles, and all the threads will execute the same instruction concurrently. For instance, if all the threads are updating the x coordinate of the particle, all threads need to fetch x from memory at the same time, which are 52 bytes (or practically 56 bytes due to padding) apart in memory. As shown in Fig. (3.7-a), an array

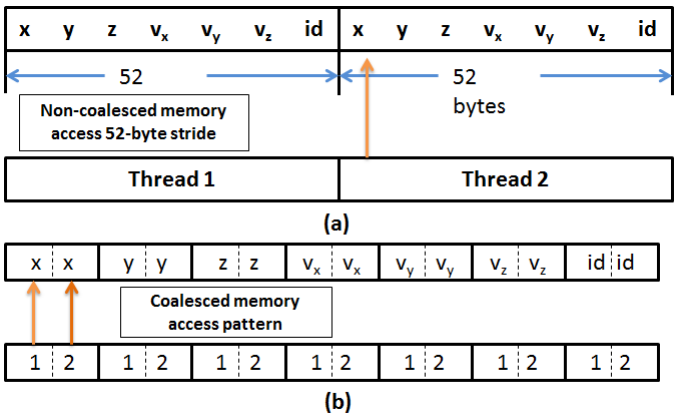

Figure 3.7: (a) Strided memory access on a GPU with an array of structures. (b) Coalesced memory access after changing to the structure of arrays.

of structures for particles will result in a strided memory access. Thus, it would result in poor utilization of memory. The data structure for particles was changed to structure of arrays instead of an array of structure as shown in Fig. (3.7) to have a coalesced memory access. After this change, 8 out of 20 global loads in *Mover* are coalesced. Still, the remaining 12 global loads will be uncoalesced. Recall that the rest of the 12 global loads correspond to the electric and magnetic fields on the neighboring four grid points, and it is highly unlikely for two adjacent particles in the data structure to reside in nearby cells as the particles are spread across the grid in a random fashion as shown in Fig. (3.9-a). The strategy-3 addresses this issue. Moving on, all the 6 global stores to update the phase space are coalesced in *Mover*. In addition to that, all the three global load operations in *Charge Deposition* are coalesced. Atomic operations in *Charge Deposition* are also susceptible to uncoalesced memory access on the grid point. Fig. (3.7-b) shows the visual interpretation of the data structure changes that are incorporated in this strategy.

Strategy 3: Sort-Shuffle

Sorting as described in [73, 142] is used to bring together all the particles within each cell in the adjacent locations of the particles data structure. The sorting algorithm used is a slightly modified version of bucket sort to rearrange only those particles which have moved away from the intended cell. First, a histogram is created to count the particles in each cell. Each thread is assigned one particle, and it increments the cell counter in which the

particle resides using global atomics. A scan is performed on this histogram to facilitate the creation of sorted indices of cells called bucket_num. Now, a second histogram is created to find the number of particles leaving. The size and the offsets can be determined from this new histogram. The array particle_buffer is used to rearrange the misplaced particles with the help of holes_buffer, which keeps track of the index. Variables are used to keep track of the number of entries in the buffer. These variables are updated using global atomic adds. Finally, the particles are put in the right cell by fetching the index from the holes_buffer. Once sorted, the adjacent particles in the structure of

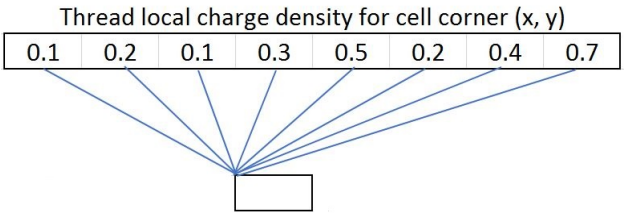

Figure 3.8: Threads competing to perform atomic add on the same cell's corner.

arrays will be in the same cell or in the neighboring cell as shown in Fig. (3.9-b). Hence, they will all perform a global read on the same four corners of the cell, thereby increasing the L2 cache hit rate and reducing the number of global load transactions. Thus, the remaining 12 global loads (four for each E_x, E_y and B_z) of the *Mover* are now coalesced memory access. Recall that the global loads in *Charge Deposition* were already coalesced, and global atomics were used to update the values of the charge density on the four corners of the cell. A caveat of Sorting would be apparent here as all the threads working on the particles residing in the same cell will be competing to update the charge density on the same four corners resulting in a divergent execution as shown in Fig. (3.8). This will result in very poor performance. The next paragraph explains a different strategy for *Charge Deposition* to overcome this problem.

We propose a similar approach to what has been described in one of the *Charge Deposition* strategies in [73]. But instead of using shared memory, we propose the use of CUDA intrinsic called SHFL for performing reductions. Each thread block with exactly 32 threads (one warp) is assigned to each cell. An equal number of particles are distributed to each of the 32 threads to mitigate a divergent execution. As shown in Fig. (3.10), half of the threads will read the

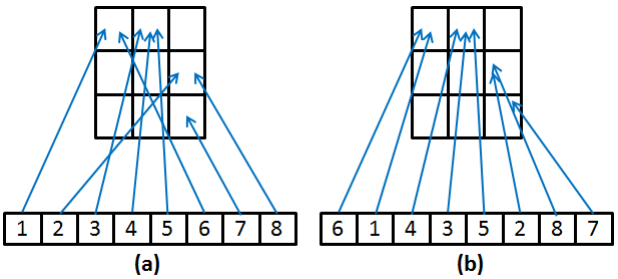

Figure 3.9: Rearranging misplaced particles to achieve spatial locality. (a) Unsorted particles are trying to access grid cells randomly. (b) After sorting, adjacent particles access the same grid cell.

charge density from the other half and add it to their personal register. This process will continue until the first thread in the block has the aggregate charge density of the entire cell. Finally, it will perform a global atomic add to deposit the charge density to the global array. Essentially, the entire operation is a reduction without making use of shared memory followed by a global atomic add. Using this *Charge Deposition* strategy, the number of atomic operations reduce dramatically. Earlier, four atomic operations were required for each particle. Now, we only require four for each cell.

```
double reduce(double val) {
  for (int index = threadCount/2; index > 0; index /= 2)
    val += __shfl_down(val, index);
  return val;
}
```

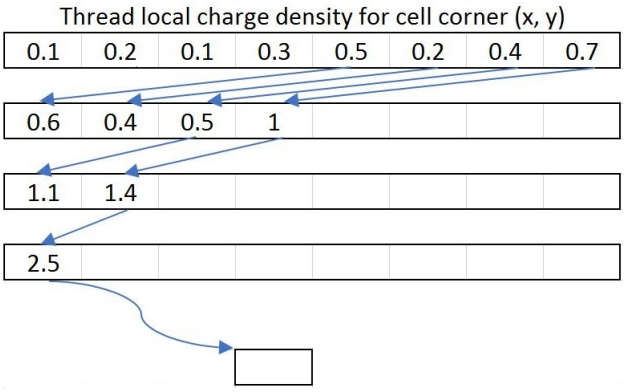

Figure 3.10: Pseudo-code for intra-warp parallel reduction using shuffle down CUDA intrinsic. It is followed by a visual representation of reduction with a single global atomic add operation peformed at last.

3.3.3 Performance Results of GPU parallelization

Several methodologies are adopted in this section to evaluate the performance of our GPU based PIC codes. Our main goal is to identify the best

parallelization strategy for Kepler architecture and identify the important factors affecting the performance of a GPU based PIC code. Firstly, we study and compare the behavior of *Mover* and *Charge Deposition* modules across all the strategies discussed in the previous section while keeping the test bench (hardware-software environment) and the simulation parameters same. It helps to get a better insight of the performance of each strategy without introducing any external variables pertaining to the test bench. Secondly, we have varied the simulation parameters i.e. grid size, PPC, and total number of particles to understand the overall behavior of the PIC code on a GPU. In this case also we have used the same test bench to analyze the performance variations that are caused due to changes in simulation parameters. Finally, we benchmark the best GPU strategy on three different test benches as shown in Table 3.7. Bench 1 will be the primary system and it will be used in almost all scenarios discussed here. It consists of a Xeon E5-2630 v3 CPU along with 64 GB ECC enabled RAM and Tesla K40 graphics card having 12 GB VRAM. For speedup comparison of GPU based code against a serial CPU version we have used the system described in bench 1 with one core. All codes were compiled using gcc 4.8 for CPU and nvcc 7.0 for GPU. Standard procedures have been followed during the collection of performance related data [86].

Specifications	**Bench 1**	**Bench 2**	**Bench 3**
CPU	Xeon E5-2630 v3	Core i7-4690	Xeon E5-2630 v3
Core Count	8	4	8
Base Clock	2.40 GHz	3.60 GHz	2.40 GHz
Turbo Clock	3.20 GHz	4.00 GHz	3.20 GHz
L3 cache	2.5 MB/core	2 MB/core	2.5 MB/core
RAM (DDR3)	64 GB	32 GB	16 GB
ECC enabled	Yes	No	No
Graphics Card	Tesla K40	GTX 690	Quadro K620
GPU Name	GK110	GK104	GM107
Architecture	Kepler	Kepler	Maxwell
GPU Clock	745 MHz	915 MHz	1058 MHz
Boost Clock	875 MHz	1019 MHz	1124 MHz
Double Precision Performance	1464 GFLOPS	117 GFLOPS	25 GFLOPS
VRAM (GDDR5)	12 GB	2 GB	2 GB
Memory Bandwidth	288 GB/s	192 GB/s	28.8 GB/s
L2 cache	1536 KB	512 KB	2048 KB
ECC enabled	Yes	No	No

Table 3.7: Test Benches

A. Performance of PIC subroutines across different strategies

GPU based PIC codes with three different parallelization strategies discussed in the previous section have been executed on the Bench 1 with a 1024 x 1024 grid and 20 PPC for a similar physical problem described in Chapter 1 section 1.4. Fig. (3.11) shows that we have achieved speedup with all the three strategies, but there is a dramatic improvement in the speedup of *Mover* and *Charge Deposition* in the case of Sort-Shuffle strategy. In order to better

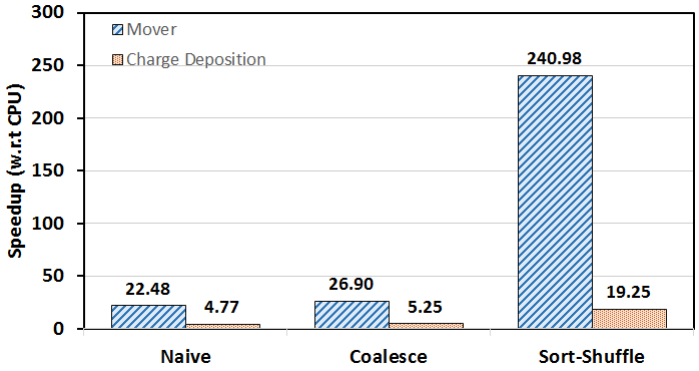

Figure 3.11: Speedup of *Mover* and *Charge Deposition* for all three strategies. Results are taken for a 1024 $\times$ 1024 grid and 20 PPC.

understand the performance gains shown in Fig. (3.11), we derived memory profiling results using Nsight Visual Profiler in CUDA toolkit, especially the number of memory transactions. A single memory transaction in CUDA refers to an access of a 128 byte memory block by a warp (32 threads). In other words, each thread contributes in accessing 4 bytes. For a fully coalesced access of a double precision value, it takes 2 memory transactions for a warp. It is important to recall that when going from Naive to Coalesce strategy, all the memory accesses to the particles data structure were coalesced. This is apparent from the Fig. (3.12) that Naive strategy requires 55.05 million store transactions while Coalesce strategy takes only 7.86 million of them. The ratio is 7:1, the same as 56:8. Phase space information is stored in a structure which is 56 bytes in size (due to 8 byte boundary alignment) as shown in Fig. (3.7-a) (padding not shown in image). Being an array of structure layout, for every 8 bytes desired, all the 56 bytes are accessed. This problem was addressed by changing array of structure to structure of arrays. This way we need not load unnecessary bytes. Reiterating that change from strategy 1 to 2 still doesn't ensure coalesced memory access for the 12 values, four

values corresponding to each E_x, E_y and B_z. This is clear from Fig. (3.12), the number of load transactions in *Mover* haven't reduced much. The dramatic reduction in the number of global loads occur when going from Coalesce to Sort-Shuffle strategy due to the sorting of particles. The access pattern for the grid data structures also becomes more predictable. For instance, *Mover* requires approximately 27 transactions per warp. 15 for phase space and charge to mass ratio ($52 + 8$ bytes) and 12 for E_x, E_y and B_z. The upper two grid points and the lower two grid points of a cell are adjacent to each other in memory. However, the upper and lower grid points have 1024 (grid size in X direction) other values in between them. Hence, the upper two and lower two grid values will be brought into L2 cache in two different memory accesses. And we know that, to bring a double value it requires 2 transactions. Hence, 12 grid points will require 6 memory accesses and hence 12 (memory access * transactions/memory access) transactions. So, the total number of global loads in *Mover* will be $27 \times 655360 = 17.69$ million (transactions/warp * warp count). The actual number is 18.31 million which can be due to a L2 cache misses.

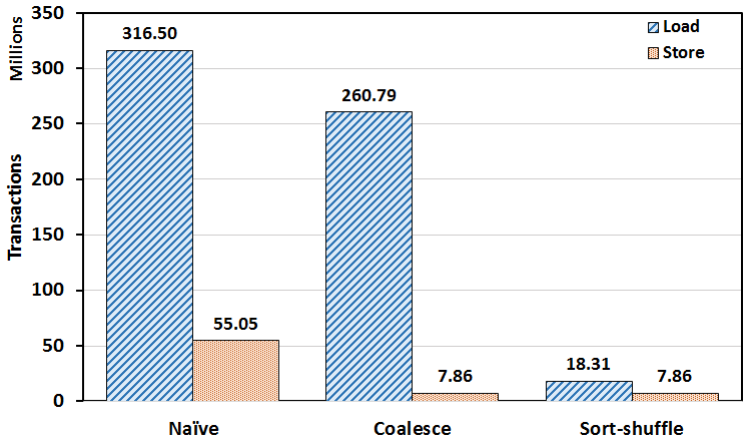

Figure 3.12: Global memory load and store transactions for *Mover* as reported by Nsight Visual Profiler. Results are taken for a 1024×1024 grid and 20 PPC.

Similarly, we also derived the number of transactions required by the *Charge Deposition* kernel as shown in Fig. (3.13). Similar to *Mover*, it is hard to predict an expected number for first two strategies due to inherent randomness. However, in last strategy 60 bytes are loaded from global memory and 4 double atomic operations are performed. Out of 60 byte loads, 28 bytes is for the phase space information, which requires 5 transactions. Recall that

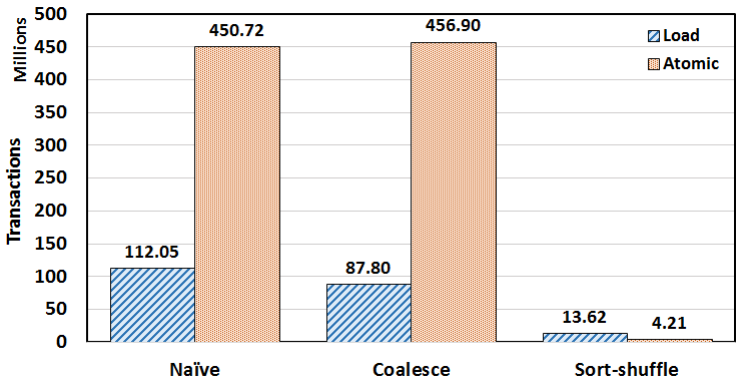

Figure 3.13: Global memory load and atomic transactions for *Charge Deposition* as reported by Nsight Visual Profiler. Results are taken for a 1024 $\times$ 1024 grid and 20 PPC.

in Sort-Shuffle a warp is launched for each cell and hence there are only 20 particles in a warp. Hence, $\frac{28}{128} \times 20 = 4.375$ transactions per warp (bytes per thread/128 bytes * active threads). For a meaningful conclusion, fractional transaction needs to be rounded off to 5 transactions per warp. Every thread requires 8 bytes of bookkeeping data, which results in 2 additional transactions per warp. Finally, four 8 byte pointers to grids points for performing atomic operations are loaded into memory. As explained previously for *Mover*, it will require 4 transactions. Hence, a total of 11 transactions are required per warp. And there are 1024 x 1024 warps, resulting in 11.53 million global loads. But the actual value is a bit more than expected at 13.62 million. However, we can accurately predict the number of atomic transactions. Each warp performs 4 atomic operations per cell. And there are 1024 $\times$ 1024 cells, resulting in 4.19 million atomic transactions. It's almost close to the actual value i.e. 4.21 million.

B. Behavior of PIC code with varying simulation parameters

As discussed earlier, the three most important simulation parameters, grid size, number of particles and PPC determines the final run-time in actual applications and it is necessary to understand the effect of these simulation parameters on the speedup of the different strategies. For these studies, we have used the first test bench with Xeon E5 CPU and Tesla K40 graphics card. In each study one of the three parameters is varied and the results are recorded.

In the first study, the grid size has been set to 256 $\times$ 256 and the number of

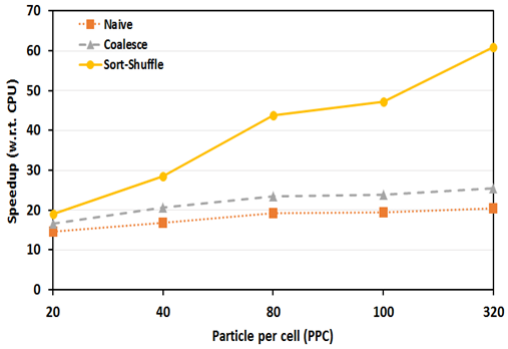

Figure 3.14: Speedup curve for a fixed 256 $\times$ 256 grid and varying number of particles. Speedup increases with increase in PPC.

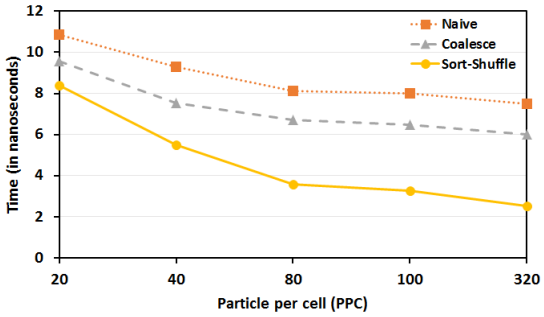

Figure 3.15: Runtime per particle for a single time step of the PIC code for a fixed grid size of 256 $\times$ 256 and varying number of particles. Runtime decreases with the increase in PPC for a fixed grid size.

particles have been varied from 20 PPC (1.31 million) to 320 PPC (20.97 million) corresponding to total 5 cases. Fig. (3.14) shows the speedup of all three strategies for each case w.r.t CPU code. A Kepler GPU can launch more than 2 billion thread blocks simultaneously. Thus, when the PPC increases the true potential of the GPU is realized and the speedup increases. But, the increase in speedup of the Sort-Shuffle strategy is phenomenal. As discussed in the earlier subsection, the dramatic decrease in the number of memory transactions is responsible for multi-fold increase in the speedup. For last case with 320 PPC, Sort-Shuffle can achieve up to 60$\times$ performance as compared to the CPU code. Secondly, in the *Charge Deposition* strategy of Sort-Shuffle, the workload per each thread increases (32 threads per cell is fixed) leading to less overhead of launching threads and less divergence. Consider the first case with 20 PPC and the last case with 320 PPC. In the first case, only the first 20 threads work on each particle while the remaining 12 threads are inactive leading to warp divergence. On the contrary, for 320 PPC each thread works on 10 particles and there is no divergence. The third reason is due to our heterogeneous CPU-GPU

implementation of PIC code where the Poisson solver runs on the CPU. As our parallel Poisson solver is running on the 4 cores of CPU, it becomes an expensive operation when PPC is less. When the number of particles are increased keeping the grid size same, the cost of Poisson solver subroutine is not so apparent in the total time. The best way to visualize the problem is to look at the run time per particle for a single time step as shown in Fig. (3.15). This holds true for all three strategies. The last strategy achieves less than 3 ns per particle for one time step.

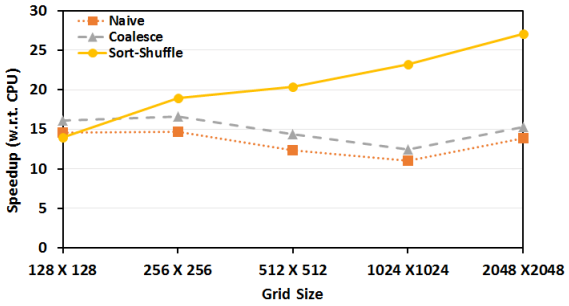

Figure 3.16: Speedup curve for varying grid size and number of particles. Particle per cell (PPC) is fixed to 20.

In the second study, we have kept the PPC fixed to 20. The grid size is varied from 128 $\times$ 128 (0.32 million particles) to 2048 $\times$ 2048 (83.88 million particles). Two interesting trends are visible in the speedup curve of Fig. (3.16). First and the most obvious is the overlap of all the curves corresponding to three strategies at 128 $\times$ 128 grid size. As described earlier, Sort-Shuffle strategy uses sorting of particles which is an added overhead. In a test case with a small grid and less number of particles, this overhead dominates the overall runtime making it slightly slower than the other two strategies. The other interesting phenomena is a drop in speedup till 1024 $\times$ 1024 and then a sudden increase. Using the perf utility in Linux we found out that the cache performance of the CPU degrades for a big grid like 2048 $\times$ 2048. Now, the CPU performs a bit slower than expected due to cache misses. Hence, the jump in speedup is seen in Naive and Coalesce strategy. Interestingly, we cannot see a drop in the speedup of Sort-Shuffle till 1024 $\times$ 1024. This is because the small effect of CPU caching is overpowered by the vast improvement in the memory access.

In the third study, the number of particles have been set to 83.88 million. The grid size varies from 256x256 (with 1280 PPC) to 2048 $\times$ 2048 (with

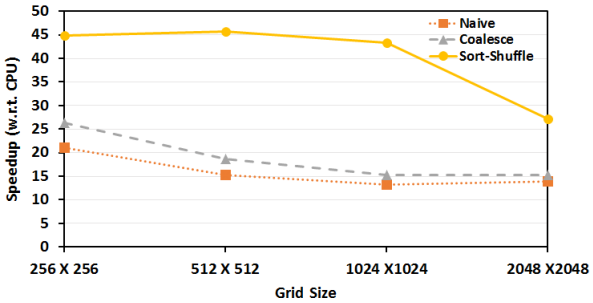

Figure 3.17: Speedup curve for a fixed number of particles and a varying grid size. Speedup decreases with increase in grid size.

20 PPC). Fig. (3.17) shows a constant drop in the speedup as the grid size is increased. This is the exact opposite of what has been discussed in Fig. (3.15). As the number of particles increase while the grid size is kept constant, the contribution of CPU based Poisson solver towards the total run-time decreases. At the same time, if the number of particles are kept same while the grid size is increased, the dominance of Poisson solver becomes apparent. Speedup drop in the Sort-Shuffle strategy for 2048 x 2048 case is also attributed to the warp divergence in *Charge Deposition*.

C. Performance of PIC code on different GPUs

The performance studies in the previous section clearly shows that the Sort-shuffle strategy is the most efficient parallel implementation. In this section, we explore the behavior of Sort-Shuffle strategy on different graphics cards. Nine test cases with variations in grid size, particles and PPC have been executed on all three test benches mentioned in Table 3.7. The main aim of this comparative study is to understand the effect of double precision performance and the memory bandwidth on the run time of the GPU based code.

To achieve our aim, we benchmark the normalized speedup of PIC codes on GTX 690 and Quadro K620 against the Tesla K40 graphics card. It is to be noted that from now on the expected values derived are based on the theoretical specifications which are susceptible to variations in actual run. However, it can still give us an idea of what should be expected out of a particular graphics card. Also, the predicted values shown in graphs are not to be misinterpreted as the upper and lower bounds.

The high end Tesla K40 has 1464 GFLOPS of double precision performance

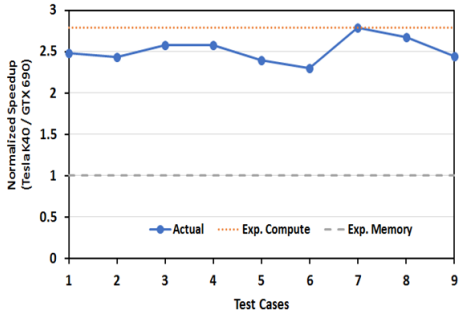

Figure 3.18: Comparison of actual normalized speedup on GTX 690 w.r.t Tesla K40. GTX 690 slows down due to compute limitations rather than memory bottleneck.

and 288 GB/s bandwidth. As per Nsight statistics, only 50% of the compute hardware was utilized i.e. approximately 732 GFLOPS for *Mover* kernel. Also, it utilizes 172.93 GB/s of memory bandwidth (without ECC overhead). *Charge Deposition* utilized very little compute hardware due to its relatively low arithmetic intensity of 0.206 and the absolute number of arithmetic operations are also less in comparison to *Mover*. Also, it utilizes about 23.81 GB/s of memory bandwidth. In theory, *Charge Deposition* will not be the main bottleneck. The major bottleneck will be caused by the *Mover* kernel and hence it is reflected in the aggregate of *Mover* and *Charge Deposition*.

The solid blue line with marker in Fig. (3.18) shows the normalized speedup of actual run on GTX 690 when compared to Tesla K40. The theoretical double precision performance of the GTX 690 is 117 GFLOPS. While, our code can utilize a maximum of 732 GFLOPS. That's slow by a factor of 6.25. But not all are arithmetic instructions. As per Table 3.1, *Mover* only has an FLOP/byte ratio of 0.446. Hence, the perceivable slowdown should be $6.25 \times 0.446 = 2.79$ times. This is shown as an orange dotted line in Fig. (3.18). Now, we need 172.93 GB/s memory bandwidth and GTX 690 offers about 192 GB/s. Hence, it should not slow down anything. From the experimental results, it is apparent that actual result follows the expected compute bottleneck line. Hence, the PIC code on GTX 690 is primarily limited by the double precision performance of GTX 690.

Enacting the same steps on Quadro K620, we get somewhat different results in Fig. (3.19). The double precision performance of Quadro K620 is 25 GFLOPS and the available memory bandwidth is 28.8 GB/s. These numbers are off

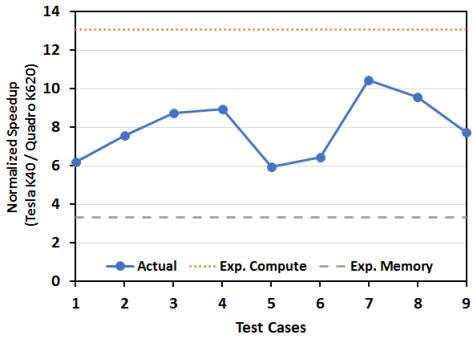

Figure 3.19: Comparison of actual normalized speedup on Quadro K620 w.r.t Tesla K40. Quadro K620 slows down due to both compute and memory limitations.

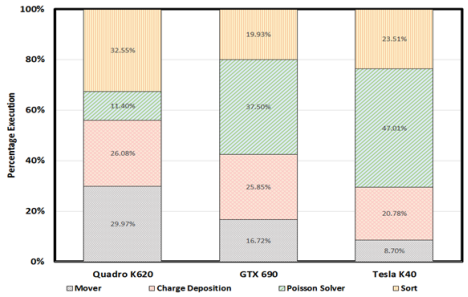

Figure 3.20: Execution fraction of different subroutines on Quadro K620, GTX 690 and Tesla K40.Dominance of Poisson Solver and *Mover* is much more on Tesla K40 as compared to other two due to more speedup in *Mover* and *Charge Deposition*. Simulation parameters were set to 512 $\times$ 512 for grid and 20 for PPC.

by a factor of 29.28 (732 GFLOPS required) and 6 (172.93 GB/s required) respectively. We have around 44.6% compute instructions and 55.4% memory operations. Hence, the expected compute slowdown would be $29.28 \times 0.446 = 13.05$ and the expected memory slowdown would be $6 \times 0.554 = 3.32$. It is shown in orange dotted and gray dashed line respectively. As we can see in Fig. (3.19), the actual values lie between the two expected values. Hence, the PIC code on Quadro K620 is limited by its double precision performance as well as its memory bandwidth.

Till now, we have glanced upon the Poisson solver (executed on CPU) and Sorting subroutine. For a large grid with less number of PPC, there is a scope of improvement for both of them especially in the Sort-Shuffle strategy. One can see in Fig. (3.20) that now Poisson solver and Sorting takes 70% of the total execution time on Tesla K40 with simulation parameters set to 512 $\times$ 512 for grid size and 20 for PPC. According to the Amdahl's law, the main speedup

limiters would be both of these and improving their performance even by a factor of 2 can show about 40-50% improvement in the overall results. The performance impact of Poisson Solver and Sorting is less pronounced but still significant in the case of Quadro K620 (about 44%) and GTX 690 (about 58%) cards because their *Mover* and *Charge Deposition* are slower as compared to Tesla K40. However, if the PPC is increased for the same grid size, the fraction of Poisson Solver will decrease but that of sorting the particles will increase. For example, with a 512×512 grid and 320 PPC, the fraction of Poisson Solver drops to 9% but that of Sorting increases to 53%. Hence, improvement to these subroutines will really speed up the entire GPU code.

3.4 Conclusions

An optimized shared memory parallelization strategy of the PIC-MCC algorithm for plasma simulation on Intel Xeon-Phi (many-core) and Xeon (multi-core) architectures as well as an efficient hybrid (OpenMP + MPI) implementation which can be easily implemented on a HPC cluster consisting of nodes with multi-core processors have been proposed and investigated in detail. In order to take advantage of recent advancements in architectures supporting hybrid parallelization, our hybrid parallelization strategy is a natural extension of the shared memory parallelization strategy which requires minimal changes in the code. Our numerical experiments with different problem sizes reveal that for large problem sizes it becomes increasingly difficult to use just the shared memory parallelization strategy because of the limited access to shared primary memory. But the hybrid parallelization strategy makes such large scale simulations possible as it makes use of a large number of nodes such that the particles fit in the primary memory of their respective nodes. Also, unlike other previous strategies based on grid decomposition, our particle decomposition strategy scales very efficiently with increasing number of nodes. We also observe that unlike Xeon multi-core architecture, observed speedup is below expectation in case of Xeon-Phi MIC processors due to lack of scope of vectorization of PIC algorithm and other limiting factors pertaining to serial executions on Xeon-Phi. Efficient hybrid PIC codes opens up many possibilities for research in the area of

Low Temperature Plasmas which require computationally intensive PIC-MCC simulations.

In this chapter, we have also studied the PIC code at a varying level of granularity. First, we implemented a few GPU parallelization strategies inspired from the existing work. Then incremental improvements pertaining especially to memory performance were incorporated while keeping Kepler architecture in purview. Finally, the Sort-Shuffle strategy leverages the idea of sorting particles along with a novel implementation of *Charge Deposition* using SHFL instruction in CUDA. This lead to a dramatic improvement in overall performance of the code. For large problem sizes, we obtained a maximum speedup of 60$\times$ in double precision mode on a Tesla K40 which is significantly higher compared to existing GPU implementations in the literature.

Other set of tests, where we studied the effect of simulation parameters such as grid size, number of particles and PPC on the run time of the code, helps us in understanding how to attain a balance between performance and simulation accuracy. For instance, having a large grid size will be a more realistic simulation, but it takes a hit on the performance. Hence, these tests help us take an informed decision to achieve a balance between performance and accuracy before running a longer simulation.

Finally, the comparison of performance of PIC implementation on different GPUs gives a better insight into the implications of having a particular graphics card. Choosing the right GPU is essential to realize the utmost potential of the code. For instance, choosing a GTX 690 would result in a 3 times slower execution in comparison to a Tesla K40 for large problem. At the same time, having the most powerful graphics card will be an overkill if the available hardware is not used judiciously. Henceforth, striking a balance between the available hardware and required double precision performance for a particular problem is important. Efficient GPU-based PIC codes opens up many possibilities for research which require resource intensive PIC simulations as a precursor for a relatively cheap cost.

CHAPTER 4

Computational characterization and physics of plasma transport across magnetic field in ROBIN

In the previous chapter, the details related to the development of the 2D-3V PIC-MCC code have been presented. In this chapter, simulation results obtained from our PIC model have been compared and validated against real experimental results. We have taken real ROBIN experimental conditions (7 mT partially Gaussian shaped magnetic filter) for our simulations, and the results have been compared with available data from the first phase of the ROBIN source experiments (without negative ions). Most of the previous simulation works reported in the literature have considered the BATMAN parameters [23, 38, 57, 145]; BATMAN (BAvarian Test MAchine for Negative ions) is a negative ion source developed at the IPP Garching [53, 54, 145]. Consideration of the full real dimensions of the experiments in the simulation is challenging due to strict spatial ($\Delta X \leq \lambda_D$) and temporal ($\Delta t \leq 0.2/\omega_p$) constraints in the 2D-3V PIC-MCC model. PIC-MCC simulations with a higher magnetic field (more than 5 mT) require a much smaller grid size and time step compared to 3 mT magnetic field due to the smaller Larmor radius and a significant decrease in Debye length as the simulation progresses. Our optimized hybrid parallel PIC-MCC code makes it possible for us to consider the full simulation domain in the plasma flux direction [36]. Here, we have used the real X dimension (plasma flux direction) of the simulation domain as in the ROBIN experiment. In this work, we have addressed all numerical constraints mentioned in Garrigues et al. [66], and

as reported in that paper [66] several previous works have been performed without considering these important numerical constraints, which leads to numerical heating and diffusion. Very few papers have reported about the direct comparison of simulation results with experiments that have been presented in this chapter, and to our knowledge, no work has addressed the issue of power to be considered during simulations while comparing the results with experiments. Different case-studies by varying the magnetic field configuration have also been performed to understand better plasma transport in different magnetic-filter field profiles, which is not available in the literature.

Organization of this chapter

The chapter is organized as follows; section 4.1 presents the simulation domain and important parameters used in 2D-3V PIC-MCC simulations for all studies presented in this chapter. Two sets of investigation have been carried out, firstly with periodic boundary condition (section 4.2) and subsequently with non-periodic boundary conditions (section 4.4). Several important aspects such as the stability of the simulation results (section 4.2.1), plasma profiles under ROBIN conditions (section 4.2.3), and how much power has to be considered while comparing simulation results with experimental results are presented in this chapter. Section 4.2 ends with section 4.3 summarizing the results from well thought out parametric studies by changing magnetic filter field configurations such as Gaussian width, magnitude, and position of the Gaussian shape magnetic filter. Section 4.4 contains results from simulations with non-periodic boundary condition. Finally the chapter ends with important conclusions from this 2D study (section 4.5).

4.1 Experimental setup and Simulation Domain

ROBIN experimental conditions given in section 1.4 have been considered for the simulation studies presented in this section. Experimental parameters are given in Table 1.1. The simulation domain considered for this study considers 2-D displacements of particles in the X-Y plane with three velocity components under the influence of an externally applied magnetic field (B_z) perpendicular

to the simulation domain. XY plane of simulation domain is parallel to the plasma transport (X-direction) and perpendicular to the magnetic field (Z-direction), as shown in Figures (1.3) and (4.1). The Gaussian-shaped magnetic field (similar to ROBIN experiments, same $\int B \cdot dl$) is applied near the extraction region. The Gaussian peak of the magnetic field is at 94 % of the X length. Source/*driver* region is between 0.02 % to 30.8 % of the X length as shown in the red shaded area in Fig. (4.1). We have used similar dimensions of the experimental setup (Fig. (1.3)) in our 2D simulations. 2D simulation

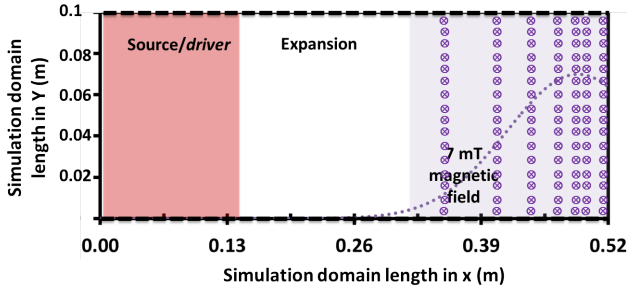

Figure 4.1: Schematic of the simulation domain. Plasma transport is in the X direction. The magnetic field is Gaussian shaped with a peak value of 7 mT in X direction and uniform in the Y direction as used in ROBIN experiments. The extraction boundary (r.h.s.) is at 0 V with respect to the source boundary. Top and bottom boundaries have a periodic boundary condition, as shown by dashed lines. In the case of non-periodic boundary conditions, top and bottom boundaries act as a wall.

of the complete experimental setup is time and memory-consuming owing to the strict constraints on time step and grid spacing (discussed in section 2.1). The correct choice of these numerical parameters is necessary to overcome the inaccuracies and errors due to numerical heating [25, 66].

Run time of the simulation can be decreased by using lower plasma density and scaling mechanism where the scale factor is calculated using the ratio of the physical plasma density to the simulated plasma density [23, 61]. The linearity between the absorbed power and the density used for scaling has been assumed. And we have taken a scale factor of 10000 for all our simulations.

In our work, considering the parameters provided in Table 4.1, we have satisfied the conditions given in Ref. [66] by using $\frac{\Delta X}{\lambda_D} \sim \frac{\Delta Y}{\lambda_D} \sim 0.1236$, $\frac{\Delta t}{0.2\backslash\omega_p} \sim 0.1512$, and particle per cell (PPC) ~ 21. In addition to that, we have

also taken care of electron and ion larmor radius. In this case, $\frac{\Delta X}{R_{Le}} \sim \frac{\Delta Y}{R_{Le}} \sim 0.6$ and $\frac{\Delta X}{R_{Li}} \sim \frac{\Delta Y}{R_{Li}} \sim 0.0065$.

(a) Physical parameters	
Simulation parameter	**Value**
Length in X	0.52 m
Width in Y	0.10 m
Gas	H_2
Pressure	0.0045 Torr (0.6 Pa)
Electron temperature	10 eV
Ion temperature	0.026 eV
Number of species	2 (electron and ion)
Bias Voltage	0.00 V
Magnetic field (B)	7×10^{-3} T
Gaussian width of B	0.29 m
Absorbed power	60 kW
Gas density	1.45×10^{20} m^{-3}
(b) Numerical parameters	
Simulation parameter	**Value**
Δ X	6.5×10^{-4} m
Δ Y	6.5×10^{-4} m
NX	800
NY	155
PPC (particle per cell)	~ 21
Simulation particles	2.6×10^{6} m^{-3}
Real Particles	0.2×10^{14} m^{-3}
Time step (Δt)	0.12×10^{-9} s
Debye length (λ_D)	5.26×10^{-3} m
Plasma frequency (ω_p)	2.52×10^{8} Hz
Heating frequency	1×10^{8} Hz

Table 4.1: Simulation parameters used for 2D-3V PIC MCC simulations.

4.2 Periodic boundary condition (without wall)

4.2.1 Stability of the simulation

The low-frequency events decide the steady-state condition for the PIC-MCC simulation. Fig. (4.2) shows density and electron temperature evolution with time in 4 different parts of the simulation domain. The parameters used for these calculations are mentioned in Table 4.1. The power used for stability results shown in Fig. (4.2) is 10 % of the total power, and similar stability is also achieved for higher values of power. The density and electron

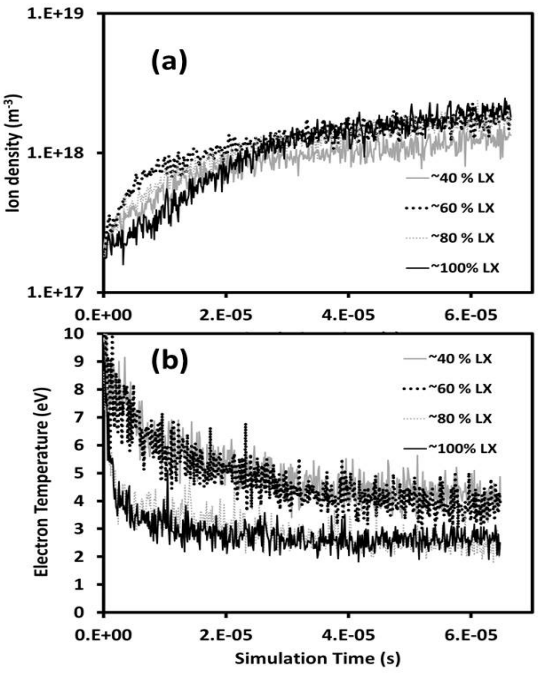

Figure 4.2: Evolution of (a) plasma density (m^{-3}) and (b) electron temperature (eV) with time. LX is the total length of the simulation domain (0.52 m). Lines show four different parts of the simulation domain. 40 % LX and 60 % LX lines are in the expansion region, 80 % LX line falls at the start of the magnetic filter, and 100 % LX line is at the extraction boundary. These lines represent 11 points of space averaged data around the central Y-axis.

temperature represented by different lines in Fig. (4.2) corresponds to different X-locations. In Figures (4.2-a) and (4.2-b), 40 % and 60 % lines are in the expansion region, 80 % line is at the starting point of the magnetic filter and 100 % line is at the extraction boundary. We have observed from Fig. (4.2-b), that the electron temperature start stabilizing after 10 μs. Ion has a residence time in the order of a few μs because ion cyclotron frequency is in order of 10^6 Hz, which decides the stability condition. Density in Fig. (4.2-a) shows a slightly increasing trend, and that is consistent with the observation in the ROBIN experiment. Important frequencies obtained from our simulation using parameters provided in Table 4.1 are shown in Fig. (4.3). Electron-ion Coulomb collision frequency is lower than the electron-neutral collision frequency in the absence of the magnetic field. In the case of the presence of the magnetic field, electron-ion Coulomb collision frequency is one to two orders higher than the electron-neutral collision frequency [23]. Both frequencies are smaller than the electron cyclotron frequency and plasma frequency. This analysis also shows that plasma frequency determines the

simulation time step.

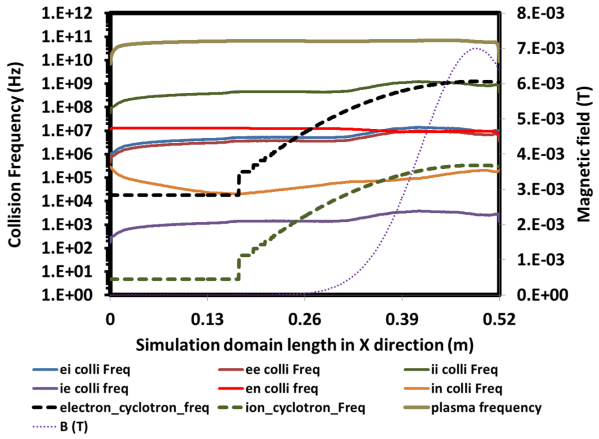

Figure 4.3: Important frequencies from our simulation using parameters provided in Table 4.1, and with electron-neutral and ion-neutral collision cross sections $\sigma_{en} = \sigma_{in} = 1 \times 10^{-19}\ m^2$.

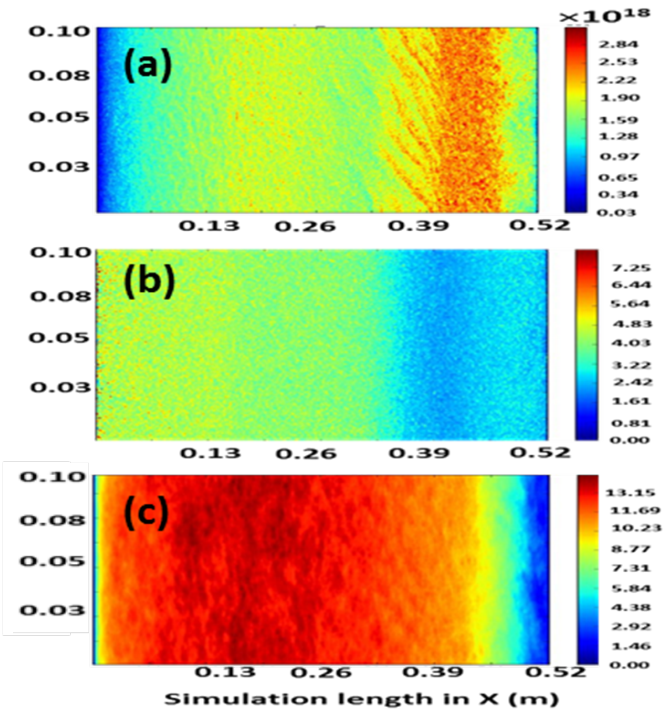

Figure 4.4: (a) Plasma density in m^{-3}, (b) electron temperature (eV), and (c) potential (V/m) at 50 μs. 2D-3V PIC-MCC simulations are done under ROBIN experimental condition as mentioned in Table 1.1 with 10 % power absorption.

4.2.2 2D profiles from simulation under ROBIN condition

2D profile of plasma density (m^{-3}), electron temperature (eV), and potential (V/m) are shown in Figures (4.4-a), (4.4-b), and (4.4-c), respectively. The effect of the magnetic filter (0.26 m-0.52 m) on plasma flux in terms of different

plasma parameters (plasma density, electron temperature, and potential) is clearly visible in Fig. (4.4). The electron temperature is around 5 eV on the left side of the magnetic filter (driver and expansion region) and starts to decrease as the strength of the magnetic field gradually increases. A magnetic filter helps in trapping the electrons, thereby increasing the collisions with neutrals due to longer residence time and reducing the electron temperature to around 2 eV in the filter field region. A decrease in electron temperature also leads to a region of maximum density (bump) in the filter field region. We observe a stripe structure in the plasma density in the X-direction, which is propagating along the Y-direction. This structure is due to instabilities caused in the magnetic filter region as mentioned in the literature [23]. The localized plasma source creates an electron pressure gradient in negative ion sources, which leads to a $\bigtriangledown P_e \times B$ drift. Without wall (periodic boundary conditions considered in our simulations) $\bigtriangledown P_e \times B$ drift current is closed. According to [98], the presence of the variations in the potential leads to the E field and causes E$\times$B drift across the magnetic filter. This gives rise to small spikes in the plasma density formed by electrons crossing the filter. These stripe structures appear to be instabilities originating from the large temperature and density gradients across the magnetic filter.

4.2.3 Power coupling studies and analysis of plasma profiles

One of the important issues while comparing the experimental and simulation results is the unknown real power actually getting coupled into the system. The power given to the RF coil is absorbed partially in the *driver* region, and some of it gets reflected back and a part of it gets lost to the walls ($\sim$30 % - 40 %) in the form of the eddy current, and RF radiation. Nearly 10 % to 20 % of the total power actually get absorbed into the system [120, 121]. Therefore, firstly, the comparison is performed by considering three different values (5 %, 10 %, and 25 %) of power (as a percentage of total applied power; PO=60 kW) coupled to the system. Fig. (4.5) shows time (45-50 μs) and space (11 points centered around the Y-axis of simulation domain) averaged simulation results. Experimentally obtained plasma density (circle markers in Fig. (4.5-a)) shows a reasonably good match with the simulation results (solid lines in

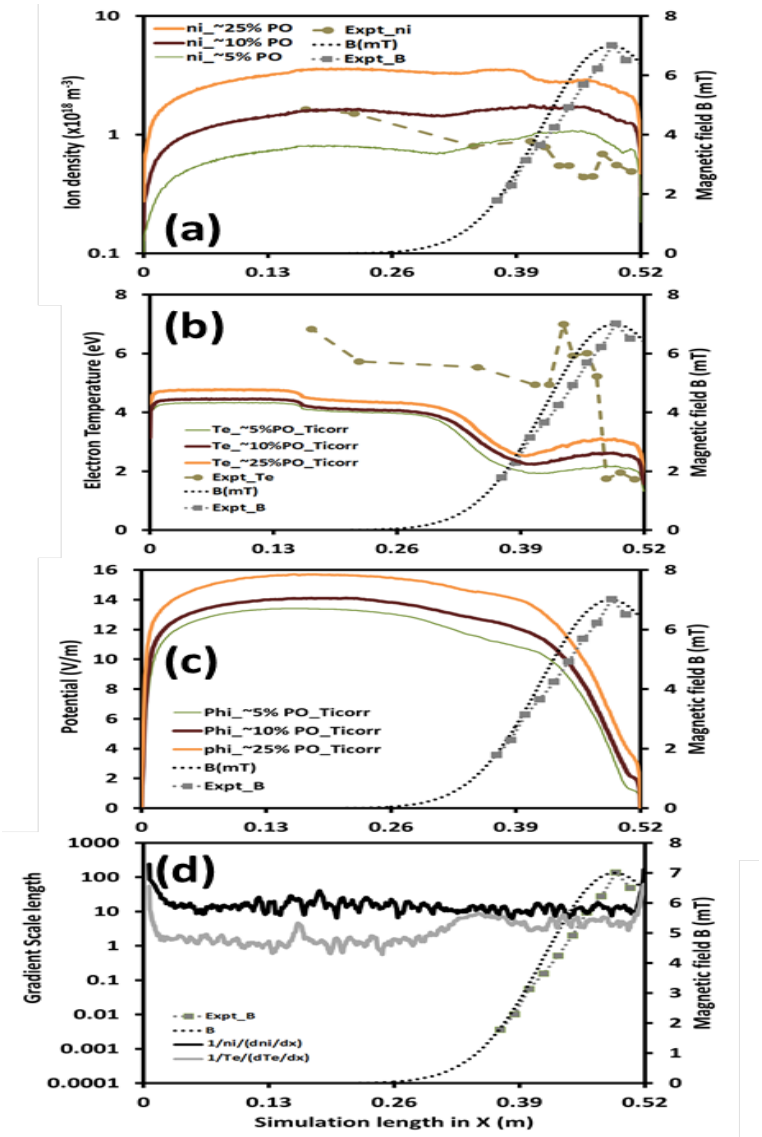

Figure 4.5: (a) Plasma (ion) density (m^{-3}) (b) electron temperature (eV) (c) potential (V/m). These results are time (45-50 μs) and space-averaged (11 points around the central Y-axis of the simulation domain) data for 7 mT magnetic field. Olive green color dashed line with circle markers shows ROBIN experimental results. PO is total power given to the system (60 kW). Other solid lines are simulation results for different percentage of power absorption in the system. Black and grey dotted lines shows the simulation and experimental magnetic field in mT (secondary Y-axis). (d) gradient scale length (GSL) of plasma density and electron temperature in the magnetic filter region for 10 % power given to the system.

Fig. (4.5-a)) when power ranges between 5 % - 10 % of PO. In our simulation results, there is a bump in plasma density in the magnetic field region which is missing in the experimental data, but variation in plasma density is following a similar trend. Such a bump in plasma density in the magnetic filter have been also reported by several other researchers in the literature [23, 24, 99]. One of the reasons for the bump is electrons in the magnetic filter region, which are strongly magnetized, and gets trapped for a longer duration (the Larmor radius is in the order of few millimeters). In Fig. (4.5-b), simulated electron temperature shows a drop at the entrance of the magnetic filter (0.30 m - 0.39 m), after that it shows a little jump and then again drop near the extraction region. This variation is also visible in experimental electron temperature data as shown in Fig. (4.5-b). In the source and expansion region, the simulated electron temperature is in range of 4 eV to 5 eV (where the magnetic field is negligible) as seen in Fig. (4.5-b). As plasma move towards the filter region, electrons get trapped, however because of ions with larger Larmor radius remain un-trapped in the magnetic filter. Trapped electrons lose their energies due to collision with neutrals and collisions play an important role in transport of electrons through the magnetic filter. Effective electron cooling is achieved by favourable transport of slow electrons. Filter field also reduces the electron density near the extraction region. A potential gradient is observed in Fig. (4.5-c) and this leads to the generation of the electric field. As the magnetic field increases towards the peak of the Gaussian, cyclotron trapping becomes stronger and leads to this potential gradient. Inhomogeneity in the electric and magnetic fields in the filter region may lead to different drifts and instabilities which can affect the plasma transport. These drifts can be attributed to E$\times$B drift and diamagnetic drift. The gradient scale length for ion density and electron temperature is shown in Fig. (4.5-d).

Considering experimental challenges in measurement of density in the magnetic filter region, we can say that, our simulation results with 5 %-10 % power shown in Fig. (4.5) shows the closest match with the experimental results [120, 121]. All the case studies presented in the next sections have been performed with 10 % power only.

Some of the discrepancies observed between simulation and experiment are

probably due to the simple periodic 2D nature of the code; whereas experiment is in 3D with walls. In addition, electron temperature measurement in the RF environment in presence of strong magnetic field itself contains large uncertainties. However, the overall trend of simulation results is in a good agreement with experimental results, and this gives us confidence in the validity of our computational model/simulations. We have performed several case studies to further investigate the role of magnetic filter in the plasma transport and interpretation of the results from ROBIN. The results from our case-studies presented in the next section can inspire new experiments and help to interpret observations.

4.3 Importance of Magnetic field configuration - Parametric Analysis

Results presented in the previous section, as well as works carried out by other research groups, clearly show that magnetic filter strongly affects the plasma flux [24, 42, 54, 77, 98, 100]. One of our primary goals is to understand how the magnitude, position, and Gaussian width of the magnetic filter will affect the plasma transport under ROBIN experimental conditions. Carrying out a series of experimental case studies of this nature is an expensive as well as time-consuming matter. The 2D-3V PIC-MCC simulations provide an accurate, easy, and affordable alternative for acquiring a first-hand quantitative estimation of the effect of different magnetic filter configurations on plasma transport. For all the case studies presented below, 2D-3V PIC-MCC simulations have been performed considering ROBIN experimental conditions given in Table 1.1.

Magnitude of B field

The most significant parameter is the magnitude of the magnetic filter. In this study, we have considered 6 cases with a magnitude of 0 mT, 1 mT, 3 mT, 5mT, 7 mT, and 9 mT. There is a significant difference in the rate of fall of electron temperature (slope of decay) for different magnitudes of B in the magnetic filter region. In case of 0 mT (in absence of magnetic field), there is no drop in

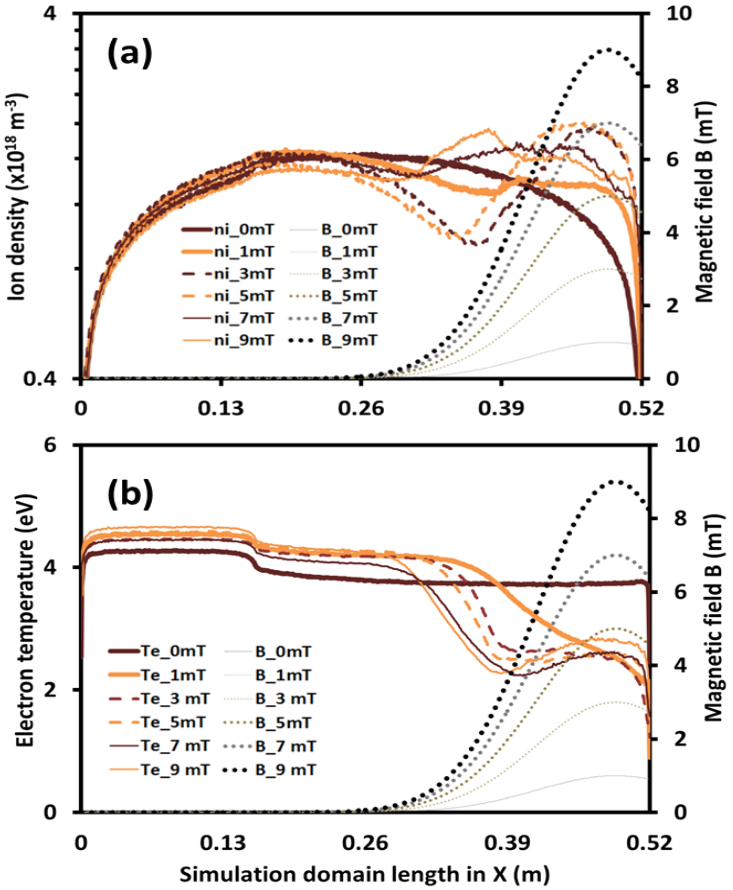

Figure 4.6: (a) Plasma density m^{-3} (b) electron temperature (eV) using 2D-3V PIC-MCC simulations with different peak magnetic filter values: 0 mT, 1 mT, 3 mT, 5 mT, 7 mT, and 9 mT for 10 % power.These are 45-50 μs time and (11 point centered around Y-axis of the simulation domain) space averaged data. Magnetic field values are given on secondary Y axis in mT.

the electron temperature in the extraction region. The electron temperature fall is gradual in 1 mT, whereas in cases of higher magnetic fields (>1 mT) initially there is a drop in the temperature followed by a small rise (in the magnetic filter region between 0.26 m - 0.51 m), and subsequently it decreases sharply in the extraction region. Small rise in the magnetic filter region between 0.26 m - 0.51 m is not visible in 3 mT case. In absence of magnetic filter (0 mT), plasma density falls very fast near the extraction region. Conventionally, high B-field leads to a greater drop in electron temperature and that is visible near the entrance of the magnetic filter. However, our simulation shows that this is not true near the extraction region (Fig (4.6-b) for the given magnetic field configuration (ROBIN B-field configuration [12])), where lower magnetic field helps to loose more electron energy than the high magnetic field. As plasma moves towards the extraction region, important changes in the physics of

plasma transport happen near the initial rise in the magnetic filter (0.26 m - 0.36 m). Both, plasma density and electron temperature falls in that region (0.26 m - 0.36 m) which is also visible in the form of a gradient in electron potential and electron pressure. Such phenomena have been also reported in different Refs. [9, 23].

Gaussian width of the B field

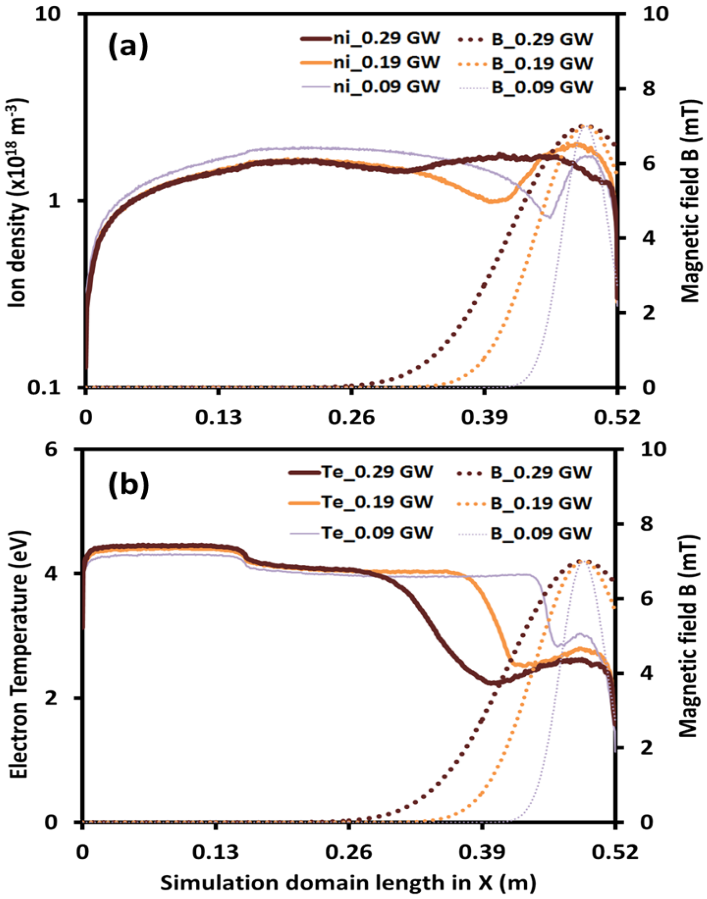

Figure 4.7: (a) Plasma density in m^{-3} (b) electron temperature (eV) using 2D-3V PIC-MCC simulations with different Gaussian width (GW) of the 7 mT magnetic filter and 10 % power shown by different solid lines. Different Gaussian widths are 0.29 m, 0.19 m, and 0.09 m. Different dotted lines shows Gaussian shape magnetic filter position with magnitude mentioned on secondary Y axis in mT. Both the data are time and space averaged.

For this case study, the magnitude and position of the magnetic filter is fixed at 7 mT and 94 % of the total simulation length in the X-direction. It is known that effective electron cyclotron trapping helps to increase negative ion production and in this context, Gaussian width plays a significant role in high energy electron trapping and electron cooling. It offers a shifting mechanism for electron temperature, potential, and electron trapping. Wider

Gaussian width aids in earlier trapping of electrons as they travel from *driver* to extraction region and thereby earlier drop in electron energy as seen in Fig. (4.7-b). Electron temperature follows three stage decrements, initially falls at the opening of the magnetic filter, then little increment due to effective trapping, and again drops at the extraction region. The bump (little increase) in electron temperature can be adjusted by choosing the proper Gaussian width (Fig. (4.7-b)). Maximum electron temperature fall is achieved by lower Gaussian width. In the experiment, Gaussian width can be chosen depending on the requirements of electron temperature drop and profiles.

Magnetic filter position

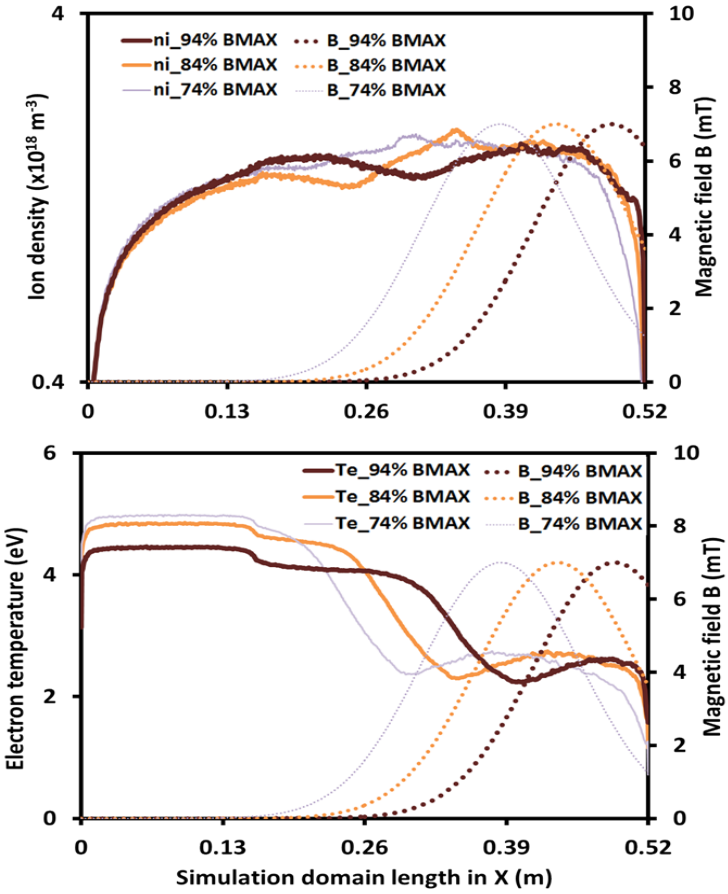

Figure 4.8: (a) Plasma density in m^{-3} (b) electron temperature in eV using 2D-3V PIC-MCC simulations with different position of the magnetic filter like 74 % , 84 % , and 94 % of the domain length keeping 7 mT magnetic field value with 0.29 m Gaussian width for 10 % power. Magnetic field corresponding to the plasma densities shown by same colour in dotted line with magnitude mentioned on secondary Y axis in mT. These results are time and space averaged.

There is another switching mechanism wherein we can keep a fixed Gaussian

width (0.29 m) and fixed magnetic filter value (7 mT), but magnetic filter location can be varied along X-direction (74 %, 84%, and 94% of the total simulation domain length in X-direction). There are significant differences in plasma density and electron temperature profiles as we change the location of the magnetic filter, as shown in Fig. (4.8). One of the observations is that as the magnetic filter moves towards the *driver* region (i.e. 74% of the domain length), electron density increases earlier, and there is a significant region along X-direction with high plasma density. However, in this case, electron temperature also drops earlier, and the slope of decrements along simulation domain length is smooth. This shows that the selection of the magnetic filter peak position is very important, which can be implemented during the experiments to achieve an efficient switching mechanism.

4.4 Non-periodic boundary condition (with walls)

The 2D-3V PIC-MCC model with periodic boundary conditions shows the presence of drifts and instabilities, and suggests particle transport across the magnetic filter is different in 2D simulations compared to 1D. However, in periodic case, due to the absence of walls, symmetry is observed in plasma profiles. In this section, plasma transport has been investigated using more realistic source geometry by considering walls in the 2D-3V PIC-MCC model. The source walls induce an E$\times$B drift current across the magnetic filter, creating asymmetry in the plasma profiles near the magnetic filter and on the extraction side.

4.4.1 Simulation parameters

Non-periodic simulations have been performed by considering wall effect in all four sides of the simulation domain as shown in Fig. (4.1). Potential on walls at source side (right side), top, and bottom boundaries in the simulation domain (as shown in Fig. (4.1)) are fixed at 0 V. Only wall potential at extraction side (right side) of the simulation domain (Fig. (4.1)) is varied from 0 V - 30 V according to the experimental condition. Simulation parameters are given in Table 4.1 and experimental parameters are given in Table 1.1.

4.4.2 2D profiles under ROBIN condition

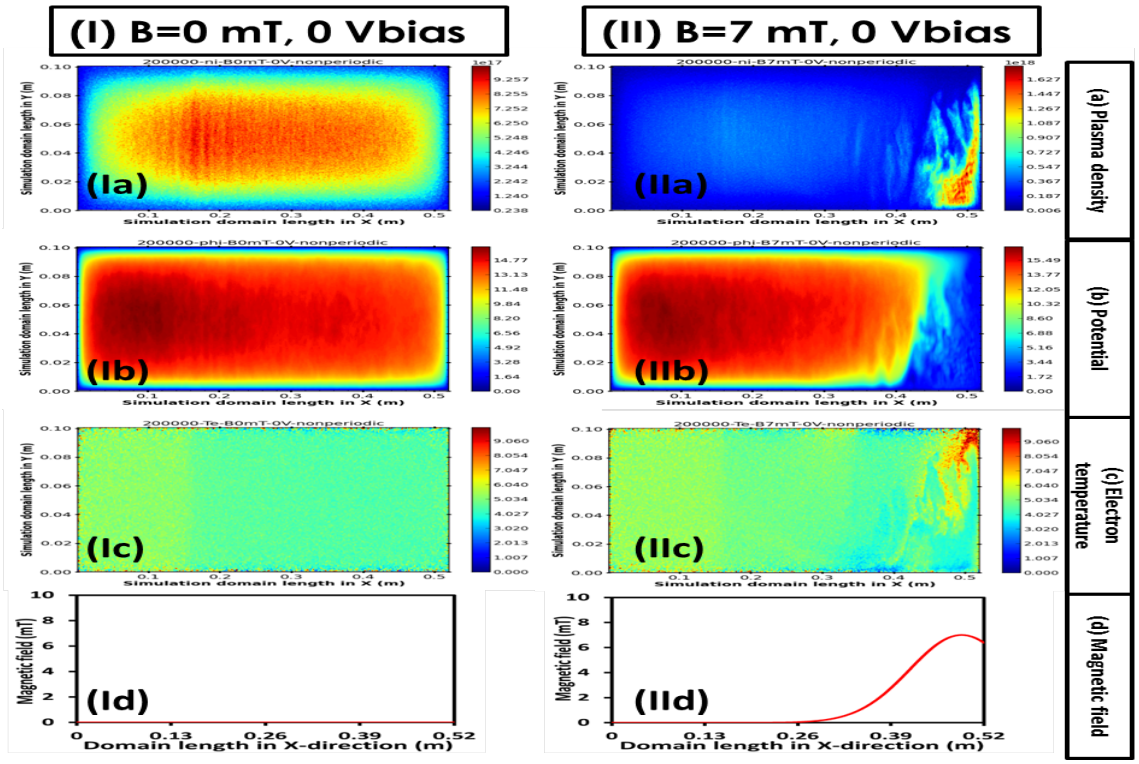

Figure 4.9: 2D profiles of plasma parameters from 2D-3V PIC-MCC simulation using non-periodic boundary conditions under ROBIN experiment conditions at 24 μs. Two cases are: (1) in absence of magnetic field and 0 V bias, (2) with 7 mT magnetic field and 0 V bias. Plasma parameters are (a) plasma density in m^{-3}, (b) potential in V, (c) electron temperature in eV, and (d) magnetic field in mT.

Observation of asymmetries

2D profiles from 2D-3V PIC-MCC simulations using non-periodic boundary conditions with 0 V bias potential on the right boundary are shown in Fig. (4.9). Fig. (4.9) shows plasma profiles for two different cases - without a magnetic field and with a 7 mT magnetic field. In absence of the magnetic field, plasma profiles (plasma density, potential, and electron temperature) looks symmetric (Fig. (4.9)) and low density is observed near the walls due to the sheath effect (as shown in Fig. (4.9-Ia)). In the case of magnetic field (case-II with 7 mT), asymmetries are observed in plasma profiles. High plasma density is seen at the bottom of the magnetic filter near right extraction side (Fig. (4.9-IIa)). This asymmetry in the plasma density creates asymmetry in potential (Fig. (4.9-IIb)) and also modifies electron transport due to electric field generated due to change in potential. Electron temperature is also

asymmetric (Fig. (4.9-IIc)) and is high, where the plasma density is low, which ensures balance in electron pressure gradient. The asymmetry in the magnetic filter region near the extraction side is caused due to the influence of the wall on the dielectric current and E×B drift flowing from top to bottom. Due to the wall, accumulation of plasma density occurs at the bottom side [24]. A potential drop is visible at the start of the magnetic field in the case of the magnetic field, as seen in Fig. (4.9-IId). This is due to the large electron potential gradient at the entrance of the filter [24].

Difference between periodic and non-periodic results

The major difference between periodic and non-periodic boundary conditions is the diamagnetic current. In periodic boundary conditions, the dielectric current is closed and does not interfere with any of the walls, which leads to structures/ instabilities flow from top to bottom. The free flow of the instability or drifts can be observed and is one of the advantages of periodic boundary conditions. That also helps in a detailed understanding of non-periodic results (effect due to the walls). The diamagnetic current is associated with the large electron pressure gradient at the entrance of the magnetic filter. That is the cause of E×B drift driven transport through the filter [24].

4.5 Conclusions

This chapter presents kinetic simulation-based plasma characterization results from an in-house developed parallel 2D-3V PIC-MCC code under conditions similar to first phase ROBIN experiments. The simulations have been performed by satisfying all the strict numerical constraints such as time step, grid spacing, and PPC required for kinetic modeling of such LTP experiments. Comparing the simulation and experimental results from ROBIN gives us sufficient confidence to do further case studies for future ROBIN experiments. Some of the important findings from our simulations using periodic boundary conditions are as follows:

- Simulation becomes stable after tens of microseconds, which is decided by shortest frequencies like ion cyclotron frequency (range of 10^6 Hz).

- Plasma density and electron temperature profiles from our PIC simulations follow similar trends as seen in experimental results. This will help us to understand the role of different diffusion and collisional processes and quantify the plasma transport accurately in the future.
- There are several considerations that need to be considered while comparing experimental and simulation results. Firstly, the time window used for measurements of experimental parameters is not accurately known. Secondly, the exact amount of power absorbed in the ROBIN experiment is unknown; however, according to experimentalists, only 10 % to 20 % of the given power is absorbed in the ROBIN. Thirdly, our simulation model is 2D and does not consider the real geometry, the complex plasma chemistry, and the wall effects. Even with these limitations, simulation results show a reasonably good match with the phase-1 ROBIN experimental results, particularly with 10 % absorbed power. Particularly the simulations are showing similar important patterns in plasma characteristics as seen in the experiments.
- Our case studies show that under ROBIN experimental conditions [12], the lower magnetic field (0.29 m Gaussian width and peak at 94 % of the domain length) gives low electron temperature at the extraction region compared to higher magnetic field values. While comparing different Gaussian widths (7 mT magnetic field magnitude and peak at 94 % of the domain length), the narrow width of the Gaussian magnetic filter reduces electron temperature more than the broader width. As the magnetic filter shifts towards the *driver* region, effective trapping results in lower electron temperature compared to the filter near the extraction region. From these three different sets of case studies, we can conclude that the magnitude, the Gaussian width, and the position of the magnetic filter will play an important role in obtaining the desired plasma profiles for efficient negative ion production.

The bumps in plasma density and electron temperature profiles in the magnetic filter region have been observed in experiments as well as in simulations; however, the nature of the bumps in both cases are different. We also observe a significant difference in the plasma density gradient scale

length and electron temperature gradient scale length, particularly near the start of the magnetic field. Results of simulations with the wall (non-periodic boundary conditions) show asymmetry in the plasma profiles that are due to the influence of the walls on the plasma transport. Instabilities are observed in the presence of a magnetic field, and further investigations of these instabilities are required for a better understanding of anomalous plasma transport across the magnetic field.

CHAPTER 5

Role of instabilities on plasma transport across magnetic field

5.1 Introduction

The results obtained from 2D-3V PIC-MCC simulations carried out under ROBIN first phase experimental conditions show that plasma transport across the magnetic filter is associated with non-collisional transport. Non-collisional transport is driven by drifts or instabilities reported in different literature [24, 62, 72, 98]. The presence of an inhomogeneous magnetic field along with a non-uniform electric field in the negative ion source creates E×B drifts [23, 98]. Such a plasma source with a non-thermal equilibrium state and inhomogeneous magnetic and electric field leads to asymmetry in the plasma density, temperature, and pressure. Several simulation studies have been performed to characterize the plasma transport across the magnetic field under such scenarios [23, 137]. Gradients of plasma parameters result in turbulence and instabilities in the plasma [143].

Some of the previous work mentions the introduction of closed E×B electron drift in the Hall thrusters [26, 150]. E×B drift instability is also known as electron cyclotron drift instability. In Hall thrusters, E×B drift is visualized as an azimuthal wave having a wavelength in mm and velocity in order of the ion-acoustic velocity [26]. A study on the ion-acoustic wave propagation in such an LTP source is possible due to the density gradient. Wave will enhance towards a positive density gradient and damp in the negative density gradient [49, 138]. Charged particles collision with neutrals in the plasma can

modify ion-acoustic wave parameters [138, 143]. If a drift wave occurs in the plasma due to an inhomogeneous magnetic field, then the wave can excite the instability [91]. The energy released from the density gradient and energy exchange through ion-wave resonance drives the drift wave [91].

Very limited efforts have been carried out to understand E×B and other drifts in the negative ion sources. In this chapter, we have done 2D-3V PIC-MCC kinetic simulation of LTP negative ion sources under conditions similar to ROBIN (RF Operated Beam source in INdia) experiments [12]. The goal of the work is to investigate instabilities and drifts in a negative ion source. We have performed some case-studies in the context of the ROBIN negative ion source to understand drifts and instability in the plasma near the magnetic filter field region. Case-studies are performed in such a way that the individual role of electric and magnetic fields can be investigated separately, and the presence or absence of drifts can be captured properly.

Organization of this chapter

The temporal evolution of instabilities is discussed in section 5.2. Effect of bias voltage and magnetic field on instabilities and plasma transport are given in section 5.3. 1D data analysis is presented in section 5.3.1 and 2D profiles of instabilities are discussed in section 5.3.2. Frequencies of instabilities are calculated using FFT in section 5.4. Further analysis towards identifying the instabilities are provided. Chapter ends with conclusion in section 5.5.

5.2 Spatio-temporal evolution of instabilities

Simulation results under ROBIN experimental conditions, presented in the previous chapter (Chapter 4), shows the presence of some structures (patterns) in the potential as well as in the density, particularly near the magnetic filter region (as shown in Fig. (4.4)) [136, 137]. This indicates that the plasma flow may be turbulent in the magnetic filter region. Spatio-temporal evolution of plasma density and potential in the center of the domain along the X-axis for a particular 2D-3V simulation is shown in Fig. (5.1). Simulation domain used for this study is shown in Fig. (4.1) and simulation parameters are given in

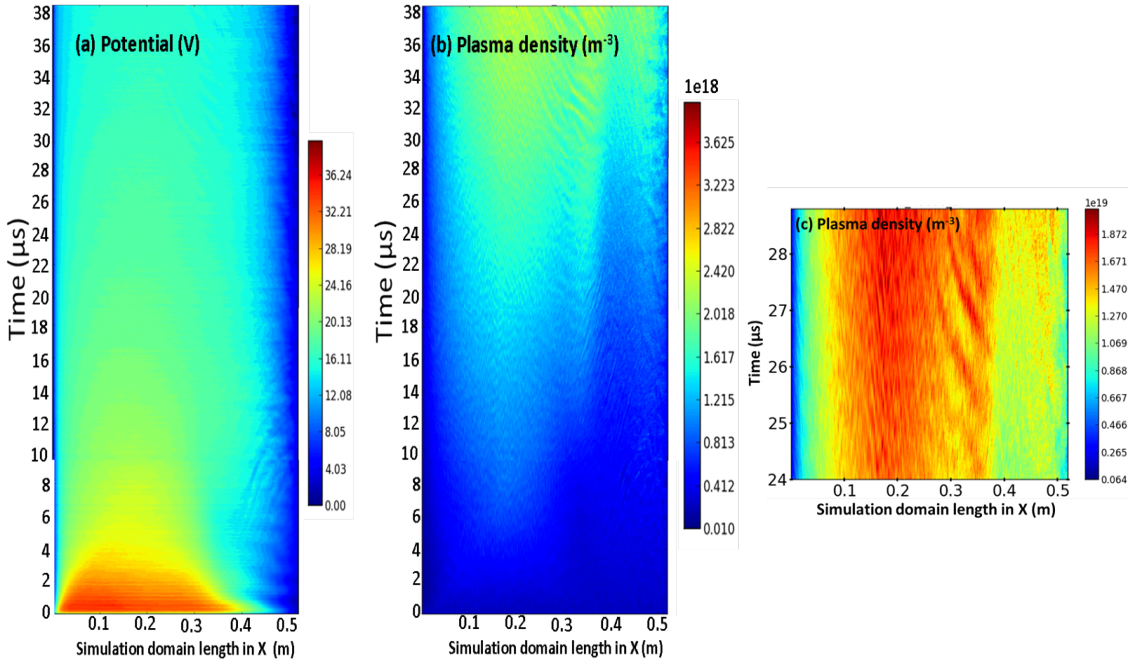

Figure 5.1: Temporal evolution of (a) the potential in V and (b) plasma density in m^{-3} within simulation domain in X direction and from the center of the axis in Y direction. (c) zoom of the plasma density (m^{-3}) from 24 μs to 30 μs.

Table 4.1. Simulations are done by using periodic boundary conditions. Fig. (5.1b) clearly shows how the instabilities evolve with time. Instabilities are more clearly visible after 25 microseconds in the plasma density shown in Fig. (5.1c). Our next goal is to understand under what conditions these instabilities appear and what controls the characteristics of these instabilities.

5.3 Effect of bias voltage and magnetic field on instabilities

Plasma flow as well the formation of structures/ possible instabilities can be well understood if we start from a simple case without a magnetic field and thereafter perform simulations with magnetic field under real experimental conditions. To investigate and quantify the plasma structures (fluctuations) characteristics near the magnetic filter region, a set of four case-studies have been performed. The simulation parameters given in Table 4.1 have been considered in the case-studies. From the Figures (1.3) and (4.1), it can be realized that after being created in the driver region, the plasma flows forward towards the extraction grid, passing through expansion zone having

spatially varying TMF. Due to this configuration, gradients of plasma density, temperature, and potential are created in that region. These gradients are the source of free energies, which lead to different instabilities in that zone. To study the nature of the instabilities, four different configurational cases are considered. These are,

Case-1: B = 0 mT, Bias voltage V_{bias} = 0 V;

Case-2: B = 0 mT, Bias Voltage V_{bias} = 20 V;

Case-3: B = 7 mT, Bias Voltage V_{bias} = 0 V;

Case-4: B = 7 mT, Bias Voltage V_{bias} = 20 V.

The bias voltage to the plasma grid manipulates the electric field inside the plasma locally by scavenging plasma electrons which essentially impacts the plasma dynamics in the filter field zone.

5.3.1 Plasma profiles with and without B field

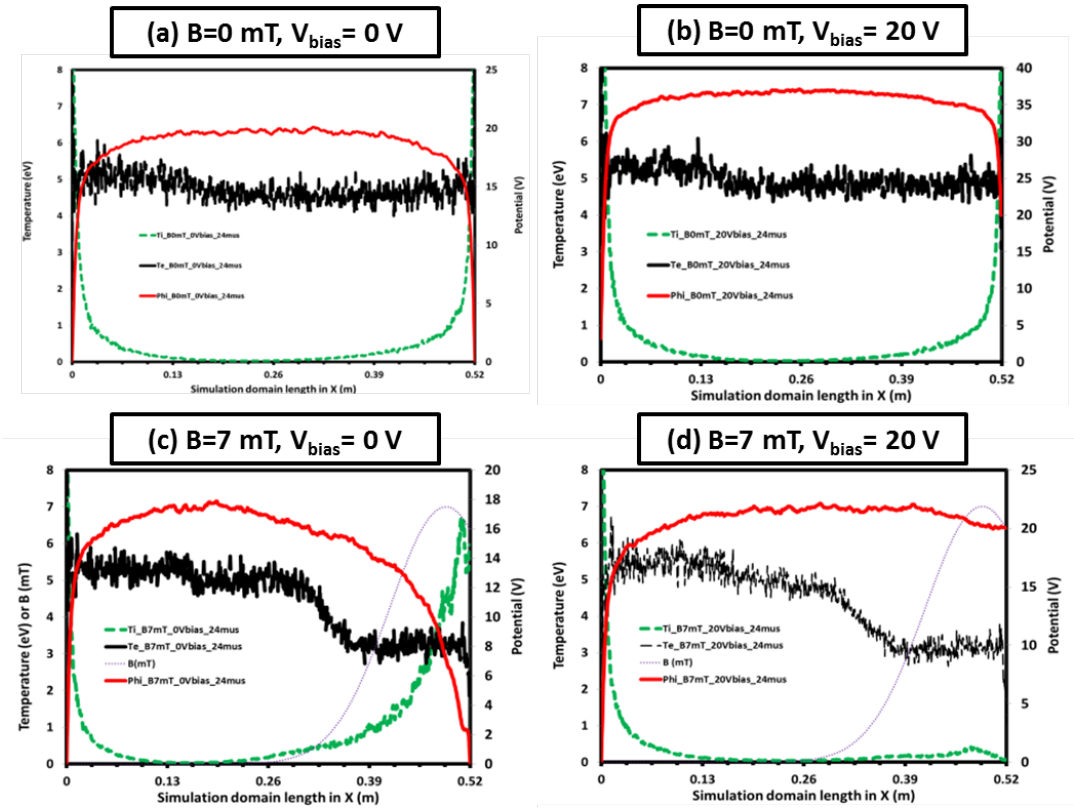

Figure 5.2: 1D profile of the plasma parameter taken from center of the simulation domain in Y-direction at 24 µs. Potential in V, electron temperature in eV, and ion temperature in eV shown by red, black solid lines, and green dashed lines respectively.

In all the cases, it is observed that simulation normally starts stabilizing after 10 µs. The 1D profile of the plasma parameters at 24 µs along the X-direction (at

the central Y-axis of the simulation domain) for all four case-studies are shown in Fig. (5.2). The plasma potential, represented by the red line, in Fig. (5.2) has a sharp gradient near the extraction region in case-1, case-2, and case-3. The sharp gradients represent the sheath region. In case-3, the magnetic field influences the plasma dynamics by magnetizing the electrons and makes the potential fall broad. As a result, a wide zone is created where a strong electric field E and an existing TMF field B are present, and it leads to E$\times$B drift of the plasma. In case-4 (7 mT and 20 V bias), the potential gradient is weak due to the collapsing of the sheath near the plasma grid, and a very weak electric field is present. In the absence of the magnetic field (case-1 and case-2), the electron temperature (shown in the black line in Fig. (5.2)) remains at 5 to 6 eV. The presence of the magnetic field (case-3 and case-4) helps to reduce the electron temperature, from 5 eV to 3 eV and less, near the extraction region. The reduction in temperature is due to the increased residence time of the electrons due to their gyration in the magnetic filter and getting trapped in the filter field zone. This trapping of electrons leads to more collisional losses, and electrons diffuse through the filter field with lower energies (shown in the black line in Fig. (5.2)). Electrons have high collision frequencies compared to the ions and therefore lose energy very fast. Near both boundaries, the source wall and the extraction boundary, a sharp potential gradient due to the presence of sheath gives rise to the electric field, which energizes the ions. In case-4, the ion energy near the extraction grid is very low due to sheath collapse by the positive bias potential applied on the plasma grid surface.

5.3.2 2D - investigations of plasma profiles

2D snapshot of plasma density in m^{-3} for all the above cases are shown in Fig. (5.3). Plasma density in such LTP source is 10^{18} m^{-3}. The plasma density is increasing initially, remains uniform in the middle of the domain, and decreases at the end in case-1 (Fig. (5.3-a)) and case-2 (Fig. (5.3-b)).

In case-3 (Fig. (5.3-c), where the magnetic field is present, a decrease in plasma density starts from the location where the magnetic field starts dominating and electrons become magnetized. This location is near the initial slope of the magnetic filter. This density fall is also associated with plasma potential

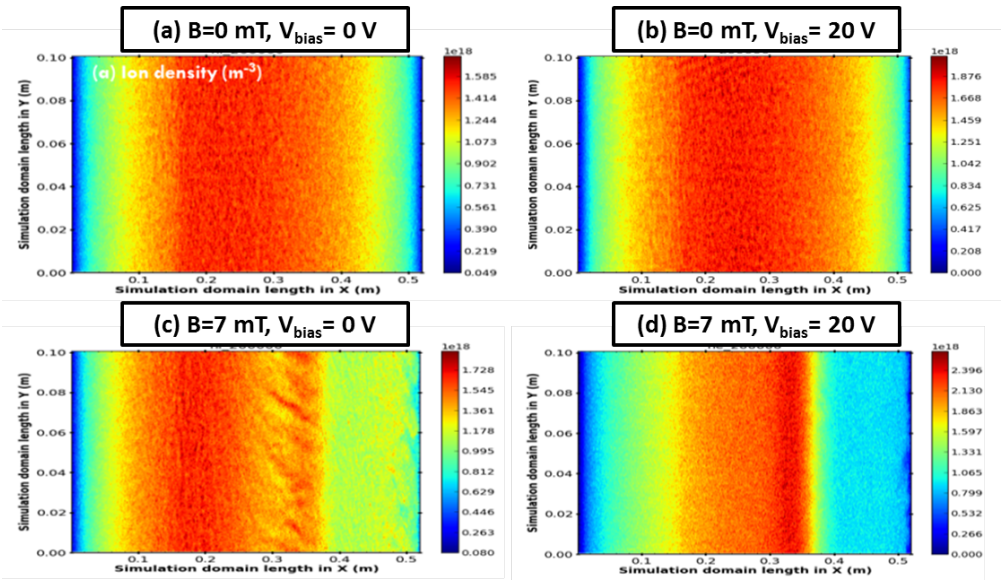

Figure 5.3: 2D snapshots of plasma density in m^{-3} at 24μs for all cases using 2D-3V PIC-MCC simulations.

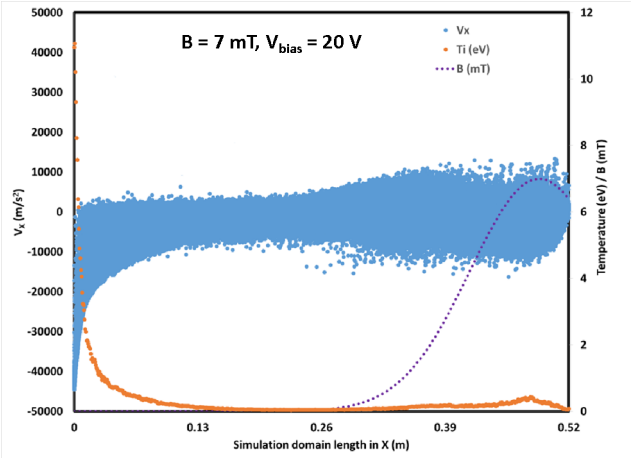

Figure 5.4: Ion velocity in X-direction V_x in m/s^2 shown by blue dots. Ion temperature in eV is given on secondary Y-axis and shown by dark orange line. Magnetic field B in mT is shown by purple line on secondary Y-axis.

fall (electric field) in Fig. (5.2-c). A strong strip structure is visible (Fig. (5.3-c)). In the case-4 (Fig. (5.3-d)), the plasma density is almost similar near the same region of the slope of the Gaussian magnetic field; however, there is no significant plasma potential gradient (electric field) in that region (see Fig. (5.2-d)). The strip structure observed in case-3 may be attributed to the E×B drift instability in the plasma near the extraction region. In case-4, we observe a small bump in the ion temperature near the magnetic filter field region. This may be due to some heating mechanism and can be further understood by looking into the particle velocities. In Fig. (5.4), ion velocity in X-direction and ion temperature in eV is plotted for case-4 (B = 7 mT, V_{bias}

= 20 V). There is a small rise in the ion temperature in the magnetic filter region. In that region, ion velocity V_x is not very different compared to the rest of the simulation domain. This shows ions are not accelerated in the X-direction near the magnetic filter region; however, there is a small bump in ion temperature. High ion energy in a small region may be due to the presence of some instabilities or some kind of resonance phenomena that need more investigation.

5.4 FFT analysis: identification of instabilities

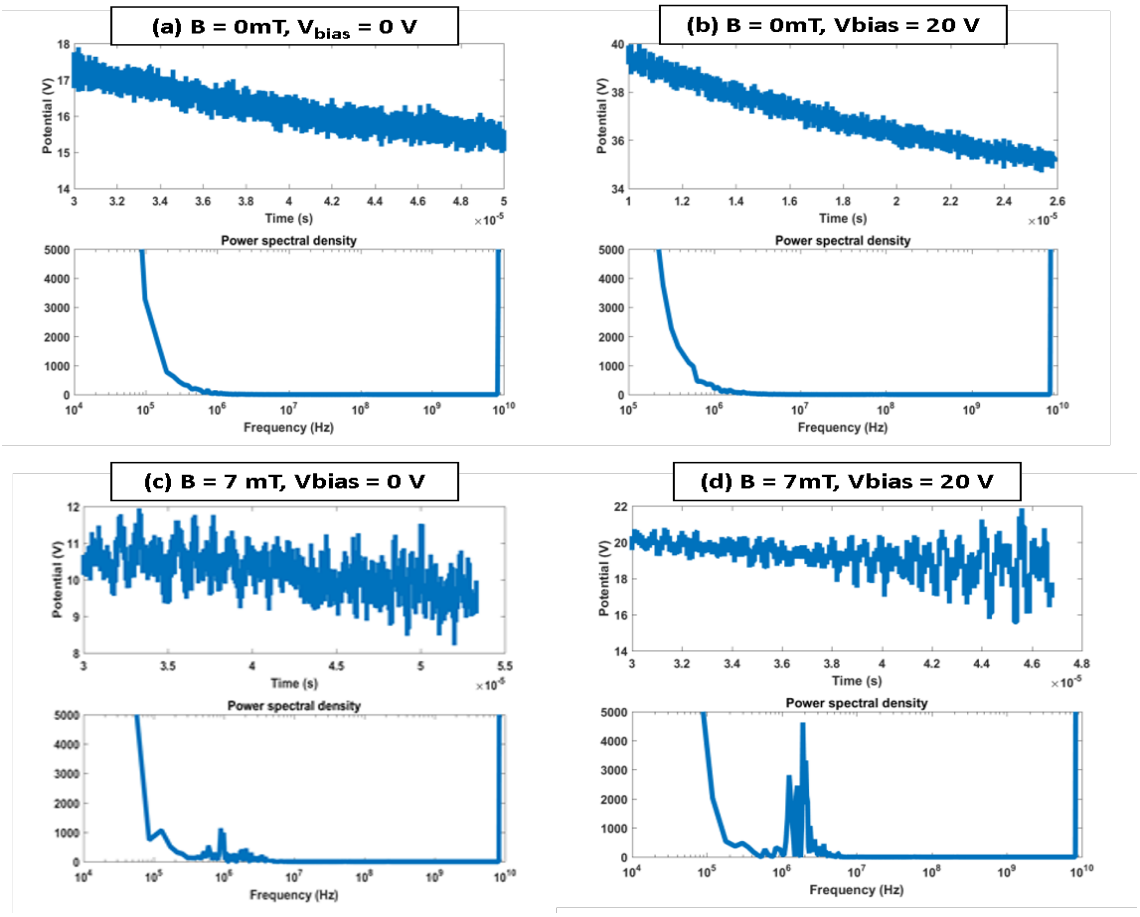

Figure 5.5: Potential with time series plots and its FFT analysis is shown for all cases. Top figure in all cases are potential time series plot from 0.4563 m in X-direction and 0.05 m at the center of the Y-direction. FFT analysis of top time series plot is shown on bottom side for all cases (case-1, case-2, case-3, and case-4).

If some instabilities are present in the source, then it will create fluctuations in density as well as in the potential. A time series and its Fast Fourier Transform (FFT) analysis of the potential profile are carried out for each case for a better understanding of the nature of the instabilities, as shown in Fig. (5.5). FFT

analysis of the time series data (top plots in all four cases in Fig. (5.5)) is shown in the bottom plots for all four cases in Fig. (5.5). In case-1 (Fig. (5.5-a)) and case-2 (Fig. (5.5-b)), no significant frequency peaks are found, but in case-3 (Fig. (5.5-c)) and case-4 (Fig. (5.5-d)), few frequency peaks are visible in two distinct region in the frequency scale. The first frequency peak, which is a bit broad, is peaked at 10^5 Hz, and the second group of peaks is at 10^6 Hz. In case-3 (Fig. (5.5-c)), 10^5 Hz peak is stronger than 10^6 Hz. In case-4 (Fig. (5.5-d)), it is opposite to the case-3 (Fig. (5.5-c)) i.e. 10^6 Hz peak family is stronger than that of 10^5 Hz. These peaks show the possible role of two different physical phenomena having different time scales and may play a role in plasma transport across the magnetic filter [23]. As described above, in case-3 (Fig. (5.5-c)), the magnetic field is 7 mT, and the bias voltage is 0 V. Due to 0 V bias voltage, there is a sharp potential gradient near the magnetic field region which generates an electric field. Case-3 (Fig. (5.5-c)) has a strong E$\times$B field compared to case-4 (Fig. (5.5-d)) and we observe that 10^5 Hz peak is stronger in case-3 compared to 10^6 Hz peak than in case-4. This shows 10^5 Hz peak corresponds to the E$\times$B instability, whose value falls in the ion-neutral collision frequency range (see Fig. (5.6)) and can lead to a resonance condition [49, 138], which may help to carry E$\times$B drift instability driven ion-acoustic wave deeper into the plasma, and eventually transfer energy to the bulk ions through ion Landau damping [161].

Additional analysis to confirm the E$\times$B drift instability has been performed by comparing theoretical and calculated velocities. E$\times$B drift instability velocity can be calculated using $\frac{E\times B}{B^2}$. Simulation velocity of instability is calculated using two ways. One is by finding ω and λ of instabilities using FFT analysis and finding $v = \frac{\omega}{\lambda}$. The second way is manually calculating the velocity of instability from the animation of plasma density. All three velocities are matched and are in order of $2 \times 10^4\ m/s$.

The frequency peaks at 10^6 Hz are more dominant when the electric field is significantly less, but the DC magnetic field is present. Therefore, it must be related to the gyration of electrons and ions. All the data plotted in Fig. (5.5) are at X = 0.4563 m location on the ion source axis. The estimated gyro frequency of electrons is 10^9 Hz, and that of ions is 10^6 Hz at that location

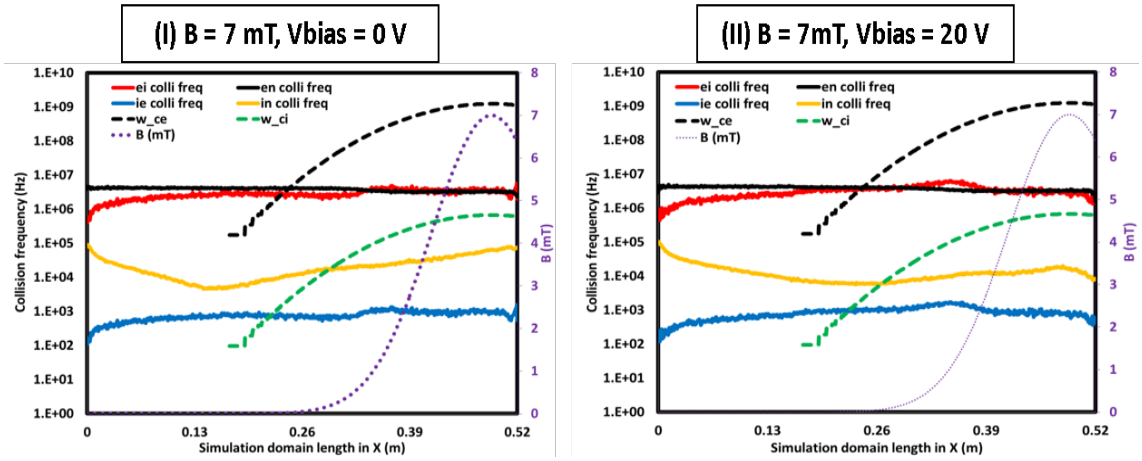

Figure 5.6: Collision frequencies in Hz calculated using 2D-3V PIC-MCC simulations.

(see Fig. (5.6)). All the collision frequencies throughout the domain (plotted in Fig. (5.6)) are calculated using the data obtained from 2D-3V PIC-MCC simulations. In the magnetic filter region, electron-ion and electron-neutral collision frequencies are in the range of 10^6 Hz to 10^7 Hz, while ion-neutral and ion-electron collision frequencies are in the range 10^3 Hz to 10^5 Hz. The nature of the instability having a frequency in the 10^6 Hz scale is not yet well understood. We need a more detailed analysis of the PIC-MCC simulation data to identify and characterize the possible type of instability in the order of 10^6 Hz.

5.5 Conclusions

This chapter presents a 2D-3V PIC-MCC kinetic simulation of plasma transport across the magnetic filter considering the ROBIN test-bed configuration having a Gaussian type transverse magnetic filter (TMF) field. Our simulations show that magnetic field helps to cool down electrons (as seen in Fig. (5.2-c) and Fig. (5.2-d) and the results are consistent with earlier literature [23, 100]. We find that the application of a bias voltage helps to reduce the strong electric field, which is generated near the boundaries otherwise. In the case of 0 V bias voltage, the ion temperature is very high near the extraction boundary due to the acceleration of ions under this electric field. On the contrary, when 20 V bias voltage is applied to the plasma grid, there is almost no electric field (no gradient of potential), and so ions are not getting

accelerated due to the electric field in case-4. As a result, ion temperature near the grid is low. However, we observe a small bump in ion temperature in case-4, and that is still under investigation. We are anticipating ion heating due to instabilities that originated in the filter field region. 2D snapshots clearly show discrete band structure, which corresponds to drifts and instabilities, and its frequencies are identified in Fig. (5.5-c) and Fig. (5.5-d). The instability corresponding to 10^5 Hz is identified as E$\times$B drift instability whereas, 10^6 Hz is still under investigation. As a future study, it is important to investigate and quantify the effect of bias voltage on the observed instabilities.

CHAPTER 6

Double layer formation and its role in plasma transport across magnetic field

The simulations performed under conditions similar to real-life experiments, discussed in previous chapters, clearly showed the presence of instabilities near the magnetic filter region [136]. The magnetic filter leads to drifts and instabilities [23, 99]. Such instabilities may induce double layer formation [19, 20, 126]. Presence of sharp potential gradient, along with few specific conditions, which separates plasma in two different regions gives rise to Double Layer (DL) [102]. The double-layer is similar to a combination of an ion sheath and an electron sheath. There is an important difference between a DL and a sheath [84]. The sheath contains either trapped electrons and free ions or trapped ions and free electrons (two types of species), while DL has both trapped and free electrons/ ions (four types of species). Different mechanisms may be responsible for DL formation in plasma such as sudden potential drop, plasma instabilities, potential structure driven by plasma flow or due to current-sheet equilibrium, charging of density cavities by plasma currents, $E_{||}$ (parallel to the magnetic field) generated by parallel currents, plasma expansion in abruptly diverging geometry and magnetic fields [141]. DL has been observed in many astrophysical events such as polar magnetosphere, aurora [117], and solar flares [93]. DL is also reported in various laboratory experiments such as Q machines [129], plasma diodes [50], triple plasma device [39], high power gas lasers [30], and ion sources [114]. The high-velocity ion beam is also achieved through a current free double layer, which is an important phenomenon in helicon double layer thruster (HDLT) [21, 35]. In

most cases, magnetic fields change charge density distribution and cause pressure gradients, which leads to the formation of DL [141]. Some previous studies have reported that DL can be found in the negative ion source, near the extraction region close to the PG, which can affect the contribution of the negative ion generated from the surface of plasma grid [74, 111, 113]. The detailed characteristics of DL found in negative ion sources and conditions under which such DL formation can take place is not being reported till now. In this chapter, investigation of DL has been done, in the negative ion source, on background plasma (considering electrons and ions) without negative ions. Studies show that the two-step volume process of negative ion generation in negative ion sources via vibrationally excited molecules is limited due to the higher destruction probability of negative ions [5]. Considering this, negative ions are neglected and only background plasmas with electrons and ions are taken.

Organization of chapter

The physics of double layer is explained in section 6.1. Simulation results and parametric studies associated with DL investigations are provided in section 6.2. Detailed analysis, using 1D profiles, towards understanding DL formation is given in section 6.3. Role of DL on ion and electron velocities are given in section 6.4. followed by conclusions in section 6.5.

6.1 Physics of double layer

The electrostatic double layer (DL) in plasma is formed due to two parallel layers of opposite and equal charges that create a sharp potential gradient and results in an electric field that accelerates and decelerates charged particles. DLs separate plasma into two regions: one with hot electrons and the other with cold electrons. Following conditions should be observed for DL formation [20]:

- Potential not following Boltzmann relation, which means that potential drop $\Delta\phi$ must be greater or equal than $\frac{kT_e}{e}$, where T_e is electron temperature of the plasma and $\Delta\phi$ is the potential step in the DL.

$$\Delta\phi \geq \frac{kT_e}{e}$$

- The electric field due to potential gradient is strong inside DL than outside.
- Quasi-neutrality is locally violated inside DL.

Potential derived from Boltzmann relation describes the ambipolar potential and applies to Maxwellian distribution of electrons [11]. Deviation from the Boltzmann relation is associated with potential due to drifts, instabilities, sheath, or DL. Strength of the DL is measured by the magnitude of $e\Delta\phi/kT_e$, where $e\Delta\phi/kT_e = 1, \leq 10, \geq 10$, and $>>10$ represents very weak, weak, strong, and very strong double layers, respectively [83]. In laboratory plasmas, DL varies from $e\Delta\phi/kT_e = 1$ [34] to 2000 [130]. In most of the cases (such as ionosphere, solar flares, thermal barriers in tandem mirrors, Q-machines), magnetic fields introduce charge separation due to different Larmor radii of electrons and ions that cause DL potential structure. The difference between DL and sheath is shown in Fig. (6.1). The schematic for potential structure in the double layer is shown in Fig. (6.1-b). The potential profile associated with DL looks similar to the potential near sheath region but features are different as shown in Fig. (6.1-Ia) [84]. In ion sheath, boundary potential is less than the plasma potential. Whereas the potential structure in DL has high potential followed by a sharp drop and subsequently reaches to the low potential. The double-layer leads to trapped electron and ion population on opposite sides as shown in Fig. (6.1-IIb and 6.1-IIIb) thereby leading to four types of distinct particles: free electrons and ions, and trapped electrons and ions. In DL, free ions get accelerated from high potential side to low potential side, that is due to an electric field generated because of positive potential gradient (as seen in Fig. (6.1-IIb)). Ions from the low potential side are not able to cross DL and gets reflected from DL. So, ions get trapped towards the low potential side (Fig. (6.1-IIb)). Electrons get reflected and trapped towards the high potential side due to an electric field generated from the positive potential gradient and free electrons from the low potential side gets accelerated towards the high potential side (as seen in Fig. (6.1-IIIb)). Free particles (electrons and ions) get accelerated and trapped particles get reflected due to potential difference in DL [83].

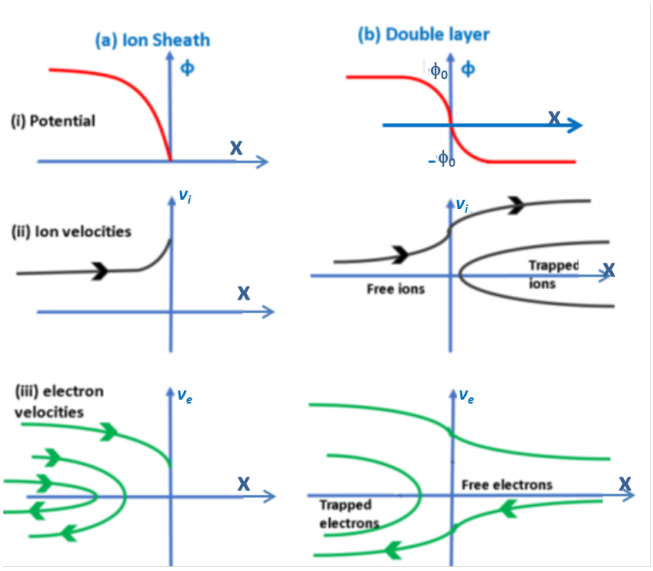

Figure 6.1: Potential ϕ and ion and electron velocities (V_i and V_e) in the phase space are shown for two different cases. (a) is for ion sheath, where the boundary is less than the plasma potential, and (b) is for double layer.

Knorr and Geortz showed that the double layer is a solution of the Vlassov-Poisson equation in the existence of free and trapped electrons and ions [83, 97]. Accordingly, 1D Vlasov-Poisson equation can be written as: (6.1) [97].

$$\frac{1}{4\pi}\phi(x)'' + \sum_k q_k n_{k,tr}[\phi(x)] + \sum_k q_k n_{k,fr}[\phi(x)] = 0 \tag{6.1}$$

where, $\phi(x)$ represents potential, k is for electrons and ions, $_{tr}$ is for trapped particles, $_{fr}$ is for free particles, and E ($E = \frac{1}{2}m_k v^2 + q_k\phi(x)$) is total energy. Distribution of electrons and ions moving from $x = -\infty$ to $x = +\infty$, potential is given by $\lim_{x\to\pm\infty}\phi(x) = \mp\phi_0$. n_k is density of any free and trapped species and function of $\phi(x)$ as given by,

$$n_k(x) = \int \frac{f_k(E)dE}{\sqrt{2m_k}\sqrt{E - q_k\phi(x)}} \tag{6.2}$$

Limits of integral of above Eq. (6.2) are as follows:

Trapped ions: $e\phi(x) < E < e\phi_0$

Free ions: $e\phi_0 < E < \infty$

Trapped electrons: $-e\phi(x) > E > -e\phi_0$

Free electrons: $-e\phi_0 > E > -\infty$

The solution can be achieved by assuming several properties of potential such

as $\phi(x)' \leq 0$ in $-\infty < x < +\infty$, $\phi(x)'$ can be expressed as a simple function of ϕ, $\lim_{x\to\pm\infty} \phi(x) = \mp\phi_0$, $\phi(x)$ is analytic, and the transition region is characterized by the scale length σ. The solution of above equation is given in Eq. (6.3), which is derived by Knorr and Geortz [97],

$$\phi(x) = -\phi_0 tanh(\frac{x}{\sigma}) \tag{6.3}$$

The potential as given in above Eq. (6.3) shows double-layer structure as shown in Fig. (6.1-Ib). A double-layer solution can be found by choosing the right electron and ion drift velocities at the boundaries. Ions with an acoustic velocity and electrons with no drift velocity may give DL solution [83]. As mentioned in [19], electrons need a minimum drift velocity. The double-layer is one of the causes to interpret charged particle acceleration to high energies.

The magnetic field plays a significant role in the creation of a double-layer by introducing instabilities. The magnetic filter separates the source into two regions: one region contains hot electrons primarily the expansion region and the second region contains cool electrons towards the extraction side. This may not be a necessary reason for DL formation, but it may help to sustain DL. We hypothesize that a double layer is formed in specific conditions of the magnetic field and bias voltage. The bias voltage applied to the bias plate may plays significant role in the DL formation. The next objective is to understand under what conditions DL may forms and can sustains in such a plasma source.

6.2 DL hypothesis based on Simulation Results

All DL related investigations presented in this chapter have been performed in the context of the ROBIN negative ion source as presented in Chapter 1 section 1.4. 2D rectangular simulation domain (Fig. 4.1) is considered as given in Chapter 4 section 4.1. Results presented in this section are under periodic boundary conditions. Simulation parameters are given in Table 4.1. All data analyses have been performed either at 24 μs or well beyond the plasma stabilization time (plasma profiles become stable after 10s of μs). As an initial step, we have considered two simple cases (case-I: absence of magnetic field and case-II: 7 mT magnetic field) to understand how background plasma

transport occurs in situations without and with a magnetic field. Firstly, 2D snapshots of plasma density and potential (Fig. (6.2)) obtained from 2D-3V PIC-MCC simulations with 0 V bias voltage are analyzed. Potential, in both cases, rises sharply at the left source side and becomes stable at plasma potential in the expansion region. In both cases, plasma potential matches with theoretical plasma potential calculated using Eq. (6.4), valid only in case of 0 V bias voltage [23].

$$V_{pp} = \frac{T_e}{2}[1 + ln(\frac{m_i}{2 * \pi * m_e})] \tag{6.4}$$

V_{pp} is plasma potential in V, T_e is electron temperature in eV, m_i is ion mass in kg, and m_e is electron mass in kg.

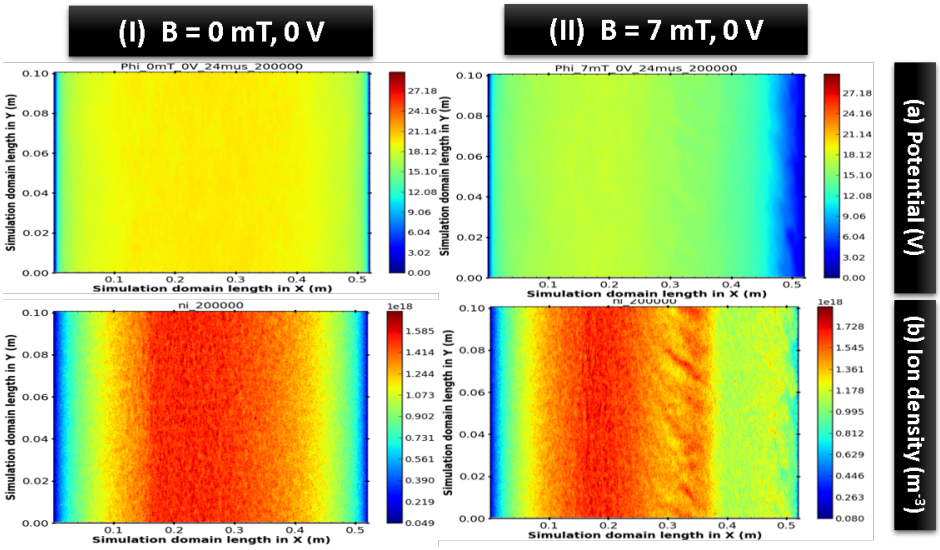

Figure 6.2: 2D snapshots of (a) plasma density in m^{-3} and (b) potential in V at 24 μs using 2D-3V PIC-MCC simulations for two different cases. Case-I is without magnetic field 0 mT and case-II is with 7 mT magnetic field. Both cases are with 0 V bias voltage.

In case-I (B = 0 mT), potential falls sharply at the right boundary near the extraction side due to the presence of 0 V bias as shown in Fig. (6.2-Ia)). In case-II (B = 7 mT), potential starts to fall early starting from the magnetic filter region (Fig. (6.2-IIa)). Cyclotron trapping becomes strong near the peak of the Gaussian shaped magnetic field and causes a potential gradient. In case-I, plasma density is high in the middle of the simulation domain and falls at both sides (right and left boundaries as seen figure in Fig. (6.2-Ib)). This sharp potential drop at the boundaries is due to sheath. Unlike case-I,

plasma density in case-II increases in the middle of the simulation domain and shows some strip structure in the magnetic filter region as shown in Fig. (6.2-IIb). These strip structures are due to instabilities as reported in the previous chapter [136, 137]. Another important observation in the case with the magnetic field (case-II) is that the potential starts falling much early near the start of the magnetic field instead of suddenly dropping at the end of the extraction side (right boundary). In this case, the potential drop in the magnetic field region is not related to the sheath. We hypothesize the possibility of instability driven Double Layer in this case and a detailed investigation is presented in the next section.

6.3 DL associated parametric studies

As discussed in the previous chapters, both, the magnetic field and bias voltage plays an important role in plasma transport. The nature of the instabilities, observed in the presence of magnetic filter, should also depend on the magnitude of B and bias voltage. The first goal is to understand, how plasma profile varies with different combinations of magnetic field and bias voltage. Therefore, we performed a well thought-out parametric study by changing B-field and bias voltages (12 cases as mentioned below).
Case-I (a) 0 mT, 0 V_{bias} (b) 0 mT, 10 V_{bias}, (c) 0 mT, 20 V_{bias}, (d) 0 mT, 30 V_{bias}.
Case-II (a) 3 mT, 0 V_{bias} (b) 3 mT, 10 V_{bias}, (c) 3 mT, 20 V_{bias}, (d) 3 mT, 30 V_{bias}.
Case-III (a) 7 mT, 0 V_{bias} (b) 7 mT, 10 V_{bias}, (c) 7 mT, 20 V_{bias}, (d) 7 mT, 30 V_{bias}.

The magnetic field magnitudes chosen for these case-studies are the most probable magnitude used in the negative ion source experiments [13, 53, 137]. Four bias voltages are chosen - zero and bias voltages below, near and above plasma potential. These different bias voltages will also effect the nature of the sheath. Plasma parameters (such as potential, electron temperature, and ion temperature) calculated at the center of the simulation domain (Y/2 axis) at 24 μs are shown in Fig. (6.3). Case studies are arranged in such a way that B increases as we move from left to right subplots, and bias-voltage increases as we move from top to bottom sub-plots. Black dotted, green dot dashed, blue dashed, and dark grey dashed lines are for potential in V, ion temperature in

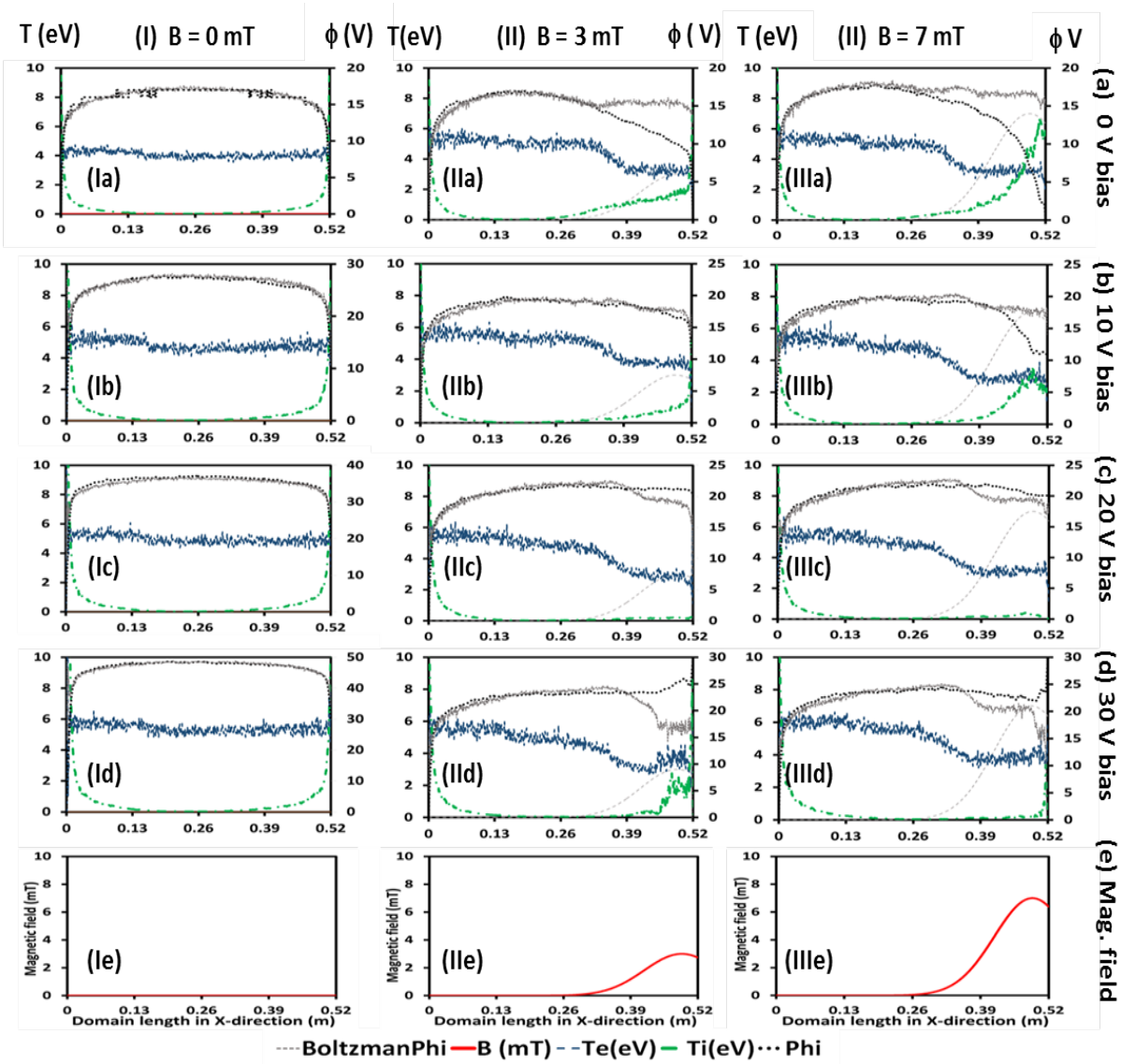

Figure 6.3: 1D profiles calculated at the center of the simulation domain at Y/2 position using 2D-3V PIC-MCC simulations with a periodic boundary condition at 24 μs for three different magnetic fields ((I) 0 mT, (II) 3 mT, and (III) 7 mT) with four different bias voltages ((a) 0 V, (b) 10 V, (c) 20 V, and (d) 30 V). Left and right axes of plots (shown in all a-d cases) represent temperature in eV and potential in V, respectively. Black dotted, green dot dashed, blue dashed, and dark grey dashed lines are for potential in V, ion temperature in eV, electron temperature in eV, and potential derived from Boltzmann relation in V, respectively. The red solid line in sub-plots e represents the magnetic field in mT.

eV, electron temperature in eV, and potential derived from Boltzmann relation in V, respectively in Fig. 6.3 (a-d). We can observe, in Fig. (6.3), that in some cases electron sheaths are observed, while in all other cases ion sheaths are observed. Electron sheath refers to the condition when the sheath or boundary potential is more than plasma potential. The ion sheath is opposite to the electron sheath where the sheath potential is less than the plasma potential

(Ia, Ib, Ic, Id, IIa, IIb, IIIa, and IIIb).

Cases without magnetic field (0 mT) : case - Ia-Id

In the simple case, without magnetic field (Ia-Id in Fig. 6.3), sharp potential drop occurs at both right and left boundaries irrespective of the applied bias voltage (black dotted lines in Fig. (6.3-I). The potential gradient at both boundaries creates an electric field which accelerates ions towards boundaries (ion temperature T_i shown by green dot dashed lines in Fig. (6.3-I)). Potential obeys Boltzmann relation throughout the simulation domain as shown by the grey dashed lines in Fig. (6.3-I). These potential drops and ion acceleration are primarily due to the applied bias potential. Potential drops that occur near both the boundaries in case-1 are matching with the theoretical potential drop obtained using Eq. (6.5).

Cases with magnetic field and ion sheath : case - IIa, IIb, IIIa, IIIb

In case-II (3 mT) and case-III (7 mT), we observe strong ion sheath with 0 V bias and weak ion sheath with 10 V bias. This shows that ion sheath characteristics depends strongly on applied bias voltage and the magnetic field (0 mT and finite B). We can also observe that conditions for double layer formation, mentioned in section 6.1, gets satisfied in case-IIa (3mT, 0 V bias) and case-IIIa (7mT, 0 V bias). In both the cases, potential drop occurs in two steps, first due to DL and then due to the sheath.

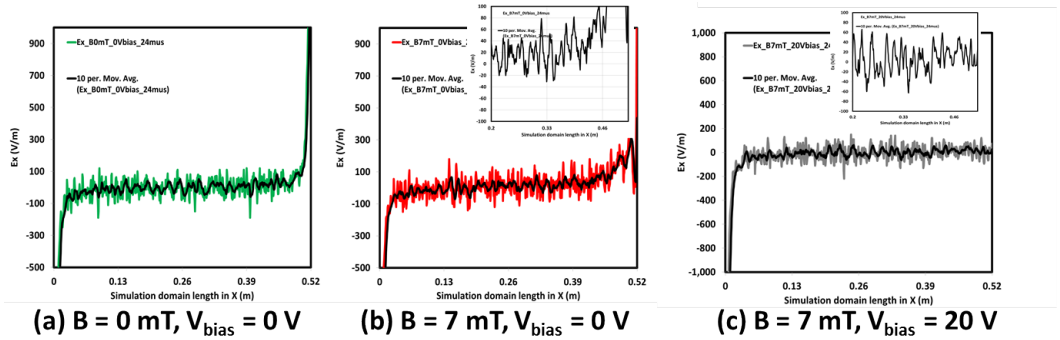

Figure 6.4: 1D profile of electric field calculated from the center of the simulation domain at Y/2 position using 2D-3V PIC-MCC simulations with a periodic boundary condition at 24 μs. Black solid line is 10 point average.

Our results confirm DL formation under specific combinations of applied bias voltage and magnetic field for the simulation setup considered in this study.

In the case-IIa, $e\phi/kT_e$ = 1.4, signifying a weak DL. In case-IIIa (7mT, 0 V bias) and case-IIIb (7mT, 10 V bias), sharp potential drops (black dotted line in Fig. (6.3-IIIa) and Fig. (6.3-IIIb)) are being visible in the magnetic filter region. These potential drops do not obey Boltzmann relation (shown by dark grey dashed line). Strong ion acceleration is visible from the green solid line in Fig. (6.3-IIIa) due to increase in the electric field as shown in Fig. (6.4-b). DL in case-IIIa (7mT, 0 V bias) has thickness of 0.26 m with potential drop of 12.5 V, with a $e\phi/kT_e$ = 4.17. We found this is the strongest DL among all the cases considered in this study. In case-IIIb (7mT, 10 V bias), potential follows three-step decrements. The first one is due to DL having $e\phi/kT_e$ = 2.52 and the last sharp drop is due to an ion sheath. This leads to a sharp increase in ion energy due to DL, and then small decrease in ion energy due to saturation in potential, as shown by the green dot dashed line in Fig. (6.3-IIIb)).

$$V_{sdrop} = \frac{T_e}{2} ln(\frac{m_i}{2\pi m_e}) \tag{6.5}$$

Cases with magnetic field and bias voltage near plasma potential : case-IIc and IIIc

In case-IIc (3 mT, 20 V bias) and case-IIIc (7 mT, 20 V bias) , there is very small potential drop at right side boundary. This is because the bias potential is assigned a value very close to plasma potential. In both the cases, the ion temperature remains very small. A little bump in the ion temperature as shown by green dot-dashed line in Fig. (6.3-IIIc)) is due to a small potential fall near the right boundary. The presence of double layer is not observed in either of these two cases.

Cases magnetic field and electron sheath : case-IId and IIId

In case-IId and case-IIId, potential is above the potential derived from Boltzmann relation and there is no DL formation. Near the boundary there is an electron sheath [84]. In case-IId, the potential follows a 2 V rise in the magnetic filter region, then a fall of 1 V, and again a rise of 5V almost at the extraction boundary. The 5 V rise near the right boundary is due to the sheath. Electron current increases with an increase in the bias potential

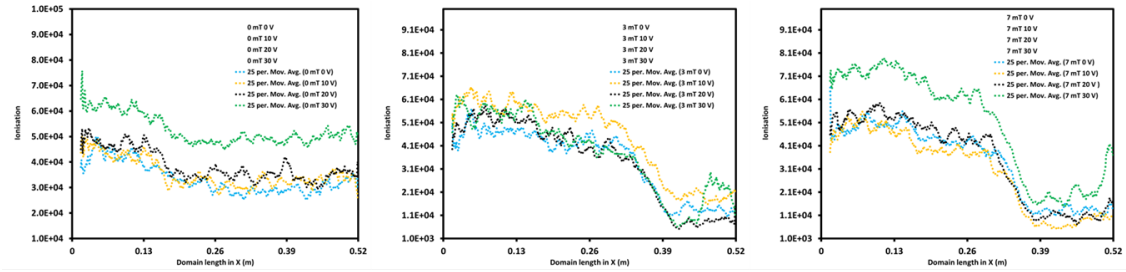

Figure 6.5: Ionisation for different cases throughout domain length in X. Different cases are: (I) 0 mT (0 V, 10 V, 20 V, and 30 V), (II) 3 mT (0 V, 10 V, 20 V, and 30 V), and (III) 7 mT (0 V, 10 V, 20 V, and 30 V). Blue, yellow, black, and green solid lines are for different bias voltages 0 V, 10 V, 20 V, and 30 V, respectively.

[23, 56]. The initial rise of 2 V in the potential accelerates electrons towards the right side and accelerates ions towards the left side. Ion acceleration towards the left side is also visible in the ion velocity plots, which have negative ion velocity V_x as shown in Fig. (6.6-IId). A bump in electron temperature shows sufficient electrons, having large energy (> 13.6 eV). High energy electrons create ionization in the magnetic filter region as shown in green dotted line in middle plot of Fig. (6.5-b) and generate positive ions. Amplification of the ion temperature near the magnetic filter region may be associated to instabilities, which needs further investigation.

Detailed investigations presented for different cases above show that the DL leads to ion acceleration near the magnetic filter region in addition to ion trapping within the instability wavelengths. We can also observe from Fig. (6.4), how the behaviour of electric field plays a significant role in increase of ion temperature. In cases, where there is no sharp variation of electric field is present, we do not observe a sudden rise in ion temperature. Average electron temperature profile shown in Fig. (6.3) helps understanding the ionization profile presented in Fig. (6.5).

6.4 Effect of Double Layer on ion velocities

As described in previous section, DLs are primarily visible in three cases: (IIa) 3 mT, 0 V; (IIIa) 7 mT, 0 V; and (IIIb) 7 mT, 10 V. DL is found to be strong in

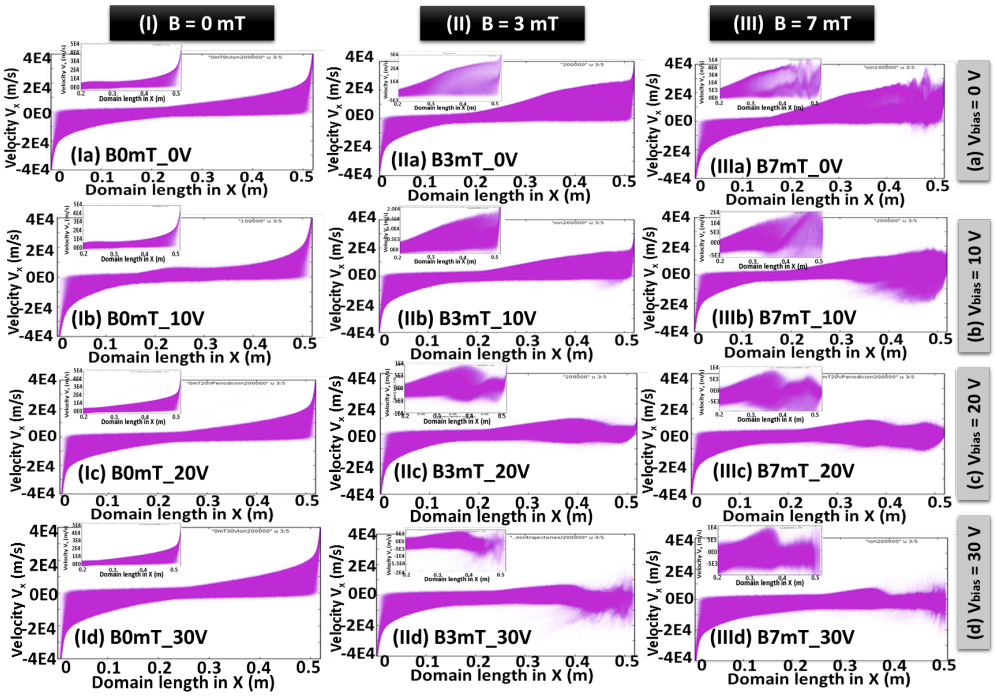

Figure 6.6: Ion velocities V_x in X-direction (m/s) Vs simulation domain length in X (m) for three different magnetic field ((I) 0 mT, (II) 3 mT, and (III) 7 mT) with four different bias voltages ((a) 0 V, (b) 10 V, (c) 20 V, and (d) 30 V) by using 2D-3V PIC-MCC simulations. Inlet plots are zoom plots from 0.2 m to 0.52 m.

case of 7 mT compared to the case with 3 mT. DL significantly effects the ion motion. Ion transport is greatly affected by variation in the potential which is either induced due to sheath, DL, or instabilities. Free ions from the high potential side face a strong electric field which accelerates ions to cross the DL barrier and reach towards the low potential side. But ions from the low potential side are reflected by strong DL due to the electric field. The low potential side has two velocity components; high velocity due to free ions from the high potential side and low velocity is due to trapped ions. The opposite effect is seen on the electrons. Due to high collision frequencies of electrons compared to ion, electron energies randomize faster. In strong DL, a split in ion velocity is visible in Fig. (6.6-IIIa). Little oscillations in ion velocities in the magnetic filter region is due to instabilities (as seen in Fig. (6.6-IIIa)) [136]. In case-IIIb, splitting of ion velocities is also visible (in Fig. (6.6-IIIb)). In case-IIa, splitting in ion velocities is not very clearly visible due to weak DL (seen in Fig. (6.6-IIa)). Very limited efforts towards understanding the effect of DL on plasma transport in the case of negative ion sources has been reported in the literature. A systematic parametric study with different values of magnetic

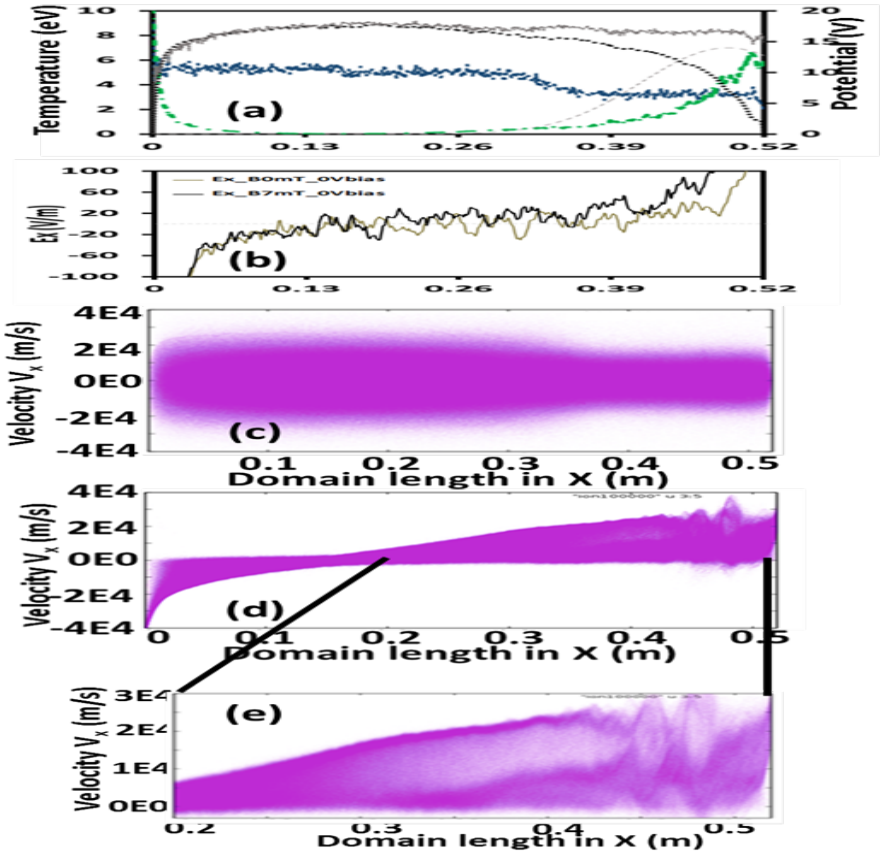

Figure 6.7: (a) 1D profiles same as shown in Fig. (6.3-IIIa) for 7 mT 0 V bias, (b) Electric field (E_x) in (V/m), where olive green solid line is for B = 0 mT, 0 V bias and black solid line is for B=7 mT, 0 V bias, (c) electron velocity in m/s in case of 7 mT, 0 V bias, (d) ion velocity in m/s in case of 7 mT, 0 V bias, and (e) zoom of ion velocity as shown in (d).

filter field and the bias voltage applied on the plasma grid carried out in the thesis clearly shows the possibility of DL formation which should be taken into account while interpreting the experimental observations.

In Fig. (6.7), a detailed picture of the physics associated with a DL observed in case-III a (B = 7 mT, 0 V bias; B shown by grey dashed line in Fig. (6.7-a)) is shown; this case shows the strongest DL among all cases considered in this study. Strong potential drop (black dotted line in Fig. (6.7-a)) is visible at the start of the magnetic filter region and it does not follow Boltzmann potential (dark grey dashed line in Fig. (6.7-a)). The sharp potential gradient leads to strong localized electric field in X-direction (the solid black line in Fig. (6.7-b))). This electric field accelerates ions towards the extraction side (free ions), but at the same time, ions from the extraction side are trapped and reflected towards the extraction side (trapped ions). This reflects in ion velocity

plots, splitting of ion velocities in two components (Fig. (6.7-d) (clearly visible in zoom figure in Fig. (6.7-d))). Small oscillations show the signature of the instabilities (Fig. (6.7-e)). Such splitting in electron velocities are not visible due to high collision frequencies of electrons ((Fig. (6.7-c)). The narrow band in the electron velocities in the magnetic filter region is decelerated due to more collisions of electrons with ions or neutrals. The ion and electron velocities profiles show that DL strongly affects ion motion compared to electrons.

6.5 Conclusions

In this chapter, DL formation is investigated in the background plasma in the context of ROBIN negative ion source using different cases with three different magnetic field values and four different bias voltages. The investigation shows that DL in such a system depends on the magnetic field, and the difference between bias voltage and plasma potential. DL does not occur when the bias voltage is more or equal to the plasma potential. Ion acceleration is found near both source and extraction boundaries either due to sheath, instabilities, or double layer. A double layer with a sheath increases the ion accelerations. DL observed in our studies can be considered as weak DL because $e\phi/kT_e < 10$ in all th cases. Due to DL, two velocities components (one due to the free ions and the other due to the trapped ions) are clearly visible. When the bias voltage is greater than plasma potential, electron sheath forms and reflects ions from extraction boundary. The little bump in electron and ion temperatures in the magnetic filter region (particularly in case IId) cab be attributed to the instabilities observed in the simulations. In this case (case-IId), there is a sharp increase in the ionization in the magnetic filter region and a rise in ionization increase the ion population in the magnetic filter region. Different behavior of electron and ion velocities suggests energy distribution functions (EDFs) for both species should be different, and a detailed investigation of ion and electron EDFs is required to get a clearer understanding of the effect of DL and instabilities on plasma transport.

CHAPTER 7

Investigation of Spatial and Temporal evolution of Energy Distribution Functions

Existing literature reveals that most of the efforts towards understanding plasma transport in negative ion sources via experiments and simulations have been made by analyzing different plasma properties such as plasma density, electron temperature, plasma potential, etc. Energy Distribution Function (EDF) measurements are challenging in such experiments due to the presence of a magnetic field, however, the PIC-MCC simulations facilitate the study of the evolution of EDF. The EEDF (electron EDF) controls these plasma properties and the rates of electron impact reactions that generate reactive species, whereas IEDF (ion EDF) is associated with surface effects. Therefore, the shape of the EDF is so important, as the rate coefficient for the electron impact processes (excitation, ionization, and dissociation) are determined by the EEDF. More importantly, drifts and instabilities are one of the causes behind DL formation [19, 20, 126] which leads to splitting of ion velocities in two components. The characteristics of the DL strongly depend on the electron and ion velocities or energy distribution functions EDFs [39, 154]. In this chapter, a detailed spatial and temporal evaluations of EDFs for both species (electrons and ions) have been presented. The simulation parameters used in this study are same as given in Chapter 4 (Fig. (4.1)). In addition to investigating the spatial and temporal evolution of EEDFs and IEDFs, we also need to understand the role of different frequencies and collision events on EDFs. Different parametric studies are reported to understand the effect of the bias voltage and magnetic field on the nature of EEDF and IEDF.

Organization of the chapter

Details related to EDF calculations in different regions of the simulation domain is presented in section 7.1. EEDF analysis and its overall nature is discussed in detail in section 7.2 followed by spatial-temporal analysis of evolution of EEDF (section 7.3) and IEDF (section 7.4). Further investigations using electron and ion phase=space plots are provided in section 7.5. Finally, section 7.6 concludes the chapter.

7.1 Energy Distribution Function (EDF)

EDF of a species (electrons or ions), defined as number of species per unit energy range, is calculated using the Eq. (7.1), takes into account all degrees of freedom associated with the species:

$$f(\varepsilon)d\varepsilon = \int_{\varepsilon_0}^{\varepsilon_f} \frac{n(\varepsilon)d\varepsilon}{N} \tag{7.1}$$

where, $f(\varepsilon)$ - energy distribution function, $n(\varepsilon)d\varepsilon$ - number of species $n(\varepsilon)$ in the energy range $d\varepsilon$ in a given region, N - total number of particles (species) in simulation, ε_0 - initial energy, and ε_f - final energy. In our case, ε_0 = 0 eV and ε_f = 100 eV. EDF is normalized by dividing EDF with maximum of all $\frac{n(\varepsilon)d\varepsilon}{N}$ in different regions of simulation domain as mentioned in section 7.2.

$$f(\varepsilon)d\varepsilon = \int_{0}^{100} \frac{n(\varepsilon)d\varepsilon}{N \cdot MAX} \tag{7.2}$$

where, MAX =$max\{(\frac{n(\varepsilon)d\varepsilon}{N})\}_{allregions}$.

In the PIC-MCC model, particle positions and velocities are calculated at each time step based on the value of EM fields and collisions. Kinetic energies of particles (species) are calculated using mean velocities, ($\varepsilon = \frac{1}{2}mv^2$). In specific regions of the simulation domain, species numbers at particular energies $n(\varepsilon)d\varepsilon$ are counted, and accordingly, a histogram is created. A histogram is a statistical representation of the data with a continuous number range. In this case, the EDF histogram is visualized as energy range (in step bar) Vs. number of species in a particular energy range. The histogram is created between 0 to

100 eV with steps of 0.1 eV. The histogram is created for different regions of the simulation domain, and only particles (species) in those regions are considered to create the histogram.

In a plasma, different kinds of EDFs can be found: Maxwellian or non-Maxwellian (Bi-Maxwellian and Druyvesteyn). The Maxwellian EDF represents the thermodynamic equilibrium state of particles among each other, and the non-Maxwellian (Bi-Maxwellian and Druyvesteyn) EDF shows the non-thermal equilibrium state of particles within the plasma. Maxwellian EDF is expressed using Eq. (7.3) and shown by blue solid line in Fig. (7.1-a) [78].

$$f(\varepsilon) = \frac{2}{\sqrt{\pi}}(kT)^{-3/2}\varepsilon^{1/2}exp\left(-\frac{1}{kT}\varepsilon\right) \tag{7.3}$$

here, ε is kinetic energy of species in eV calculated from mean velocity, $f(\varepsilon)$ is distribution function, and T is effective species temperature in kelvin. Bi-Maxwellian EDF is a sum of two Maxwellian EDFs as given in Eq. (7.4) and shown by the red solid line in Fig. (7.1-b). One of Bi-Maxwellian EDF represents low species temperature and the second of Bi-Maxwellian EDF represents high species temperature.

$$f(\varepsilon) = \frac{2}{\sqrt{\pi}}(kT_{low})^{-3/2}\varepsilon^{1/2}exp(-\frac{1}{kT_{low}}\varepsilon) + \frac{2}{\sqrt{\pi}}(kT_{high})^{-3/2}\varepsilon^{1/2}exp(-\frac{1}{kT_{high}}\varepsilon) \tag{7.4}$$

Here, T_{low} is the species temperature for low energies species group in kelvin, and T_{high} is the species temperature for high energies species group in kelvin. In Druyvesteyn distribution function (Eq. (7.5)), shown by green solid line in Fig. (7.1-a), elastic collision cross-section is considered constant [104].

$$f(\varepsilon) = C\varepsilon^{1/2}exp\left(-D\left(\frac{\varepsilon}{kT}\right)^2\right) \tag{7.5}$$

Here, $C = \frac{4[\Gamma(1/4)]^4}{\pi(12\sqrt{2}\pi eT)^{3/2}}$ and $D = \frac{[\Gamma(1/4)]^4}{72\pi^2} \sim 0.243$.

Maxwellian EDF on the semi-logarithmic scale is a straight line (as shown by blue solid line in Fig. (7.1-b)). The absolute value of the slope of this straight line is the reciprocal of the species temperature. Bi-Maxwellian EDF on a semi-logarithmic scale has two slopes (as shown by the red solid line in Fig.

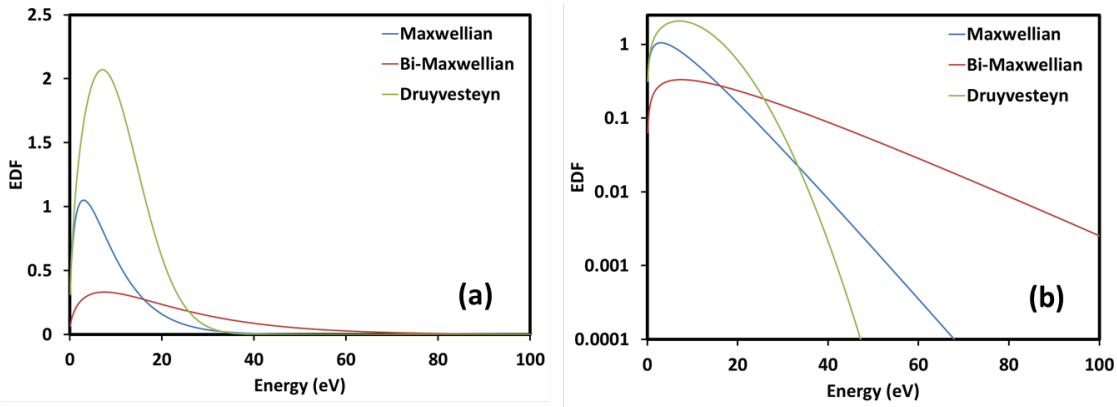

Figure 7.1: Plot shows different kinds of EDFs. Maxwellian, Bi-Maxwellian, and Druyvesteyn kinds of EDFs are shown by blue, red, and green solid lines .

(7.1-b). One slope gives species temperature for low energies species group, and the second slope gives species temperature for high energies species group.

7.2 Electron Energy Distribution Function (EEDF)

The data obtained from our 2D simulations are used to calculate electron EDFs (EEDFs) in different regions of the simulation domain. The simulation domain is divided into four distinct regions for this particular study, each of these regions represents zones where plasma transport characteristics are significantly different. First is the source region where plasma is heated at heating frequency, the second is the expansion region where plasma expands, and the other two regions are the magnetic filter regions where magnetic and electric fields influence plasma transport. Two regions near the magnetic filter are represented as "MagFilter-1" region which covers the initial slope of the Gaussian magnetic filter, and the "MagFilter-2" region is near the end of the magnetic filter. EEDF is calculated using Eq. (7.2); where MAX =max$\{(\frac{n(\varepsilon)d\varepsilon}{N})_S, (\frac{n(\varepsilon)d\varepsilon}{N})_E, (\frac{n(\varepsilon)d\varepsilon}{N})_{MagFilter\text{-}1}, (\frac{n(\varepsilon)d\varepsilon}{N})_{MagFilter\text{-}2}\}$, subscripts S, E, *MagFilter*-1, and *MagFilter*-2 are source region, expansion region, initial slope of magnetic filter between 0.38 m to 0.40 m, and near the end of the magnetic filter between 0.50 m to 0.52 m, respectively.

In our PIC-MCC simulations, initial particle EDFs are taken as a Maxwellian distribution which evolves in time and space. EDFs are modified due to collisions, drifts, and instabilities. EEDF for different regions of the simulation

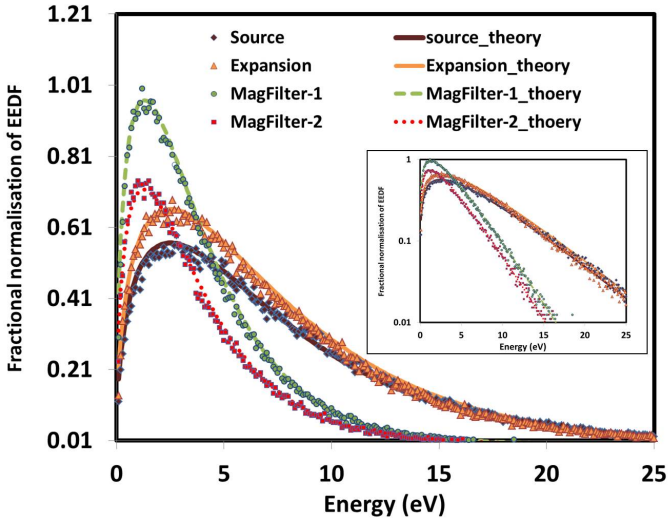

Figure 7.2: Electron energy distribution function (EEDF) calculated using 2D-3V PIC-MCC simulations for 10 % power and 7 mT magnetic field shown by markers. Theoretical Maxwellian fit is shown by lines following the same colour convention. Dimension of different regions are as follows: source- 0.10 m to 0.12 m, expansion- 0.20 m to 0.22 m, MagFilter-1- 0.38 m to 0.40 m, MagFilter-2- 0.50 m to 0.52 m. Inset figure is on a logarithmic scale.

domain at 50 μs are shown in Fig. (7.2), and simulated EEDFs (markers) are fitted with theoretical Maxwellian function (lines). EEDFs are Maxwellian in nature, which is in agreement with similar kinds of low-temperature plasma experiments involving magnetic filter [1, 76]. EEDF in the source region shows a broader width with a longer tail, showing more energetic electrons. As electrons travel from the source region to the MagFilter-2 (near extraction) region, the width becomes narrower with a shorter tail, and the peak gets shifted towards lower energy. It indicates the presence of cold electrons. The possibility of inelastic collisions is negligible in MagFilter-1 and MagFilter-2 regions due to the insignificant presence of energetic electrons ($>$ 15 eV energy).

7.3 Spatio-temporal evolution of EEDFs

As discussed in the previous section 7.2, EEDFs change abruptly in the magnetic filter region. There is a significant difference between two EEDFs in the magnetic filter region (MagFilter-1 and MagFilter-2 in Fig. (7.2)). To get a clear understanding of the role of magnetic filter in modifying the EEDF, we need to perform a fine-grained spatial analysis. Therefore, the magnetic

filter region is divided into five regions (MF-1, MF-2, MF-3, MF-4, and MF-5) and EDFs are computed in each of these regions separately. Figure (7.3) shows simulation domain with regions marked in different colors used to calculate EDFs.

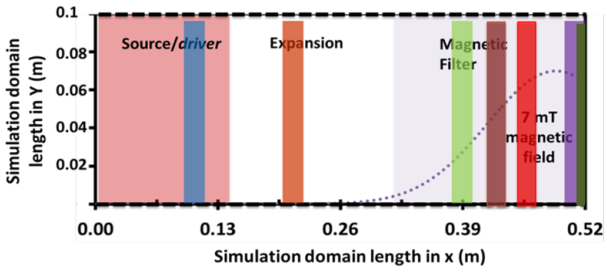

Region	Dimension
Source	0.10 m to 0.12 m
Expansion	0.20 m to 0.22 m
MF-1	0.38 m to 0.40 m
MF-2	0.42 m to 0.44 m
MF-3	0.45 m to 0.47 m
MF-4	0.49 m to 0.51 m
MF-5	0.51 m to 0.52 m

Figure 7.3: The simulation domain with different colored lines is shown in the figure. Different color lines are showing regions where EDFs are calculated. The table on the sideshows region with dimensions.

In [137], we have reported that EEDF is Maxwellian throughout the simulation domain however it will be interesting to analyze the temporal evolution of EDFs. If some interesting phenomena are happening at particular frequencies then they can be captured in the temporal evolution of EDFs. Fig. (7.4) shows EEDFs at different times 0 μs, 0.6 μs, 1.2 μs, 6 μs, 12 μs, 15 μs, 18 μs, 21 μs, 24 μs, 27 μs, and 30 μs for three different magnetic field values and in different regions of the simulation domain. As seen in Fig. (7.4), generally EEDFs become narrow as time progresses throughout the domain because electrons lose their energies through collisions. The stability of simulation results depends on low-frequency events. Ion has a residence time in the order of a few μs because ion cyclotron frequency is in order of 10^6 Hz and this decides the stability condition. In case-II and case-III (Fig. (7.4)), EEDFs become stable after 6 μs, that is larger than the ion cyclotron time. From our simulations, we find that EEDFs remain Maxwellian due to high collision frequencies and are not so sensitive to the bias voltages and magnetic field values. This observation is also consistent with some of the experimental observations.

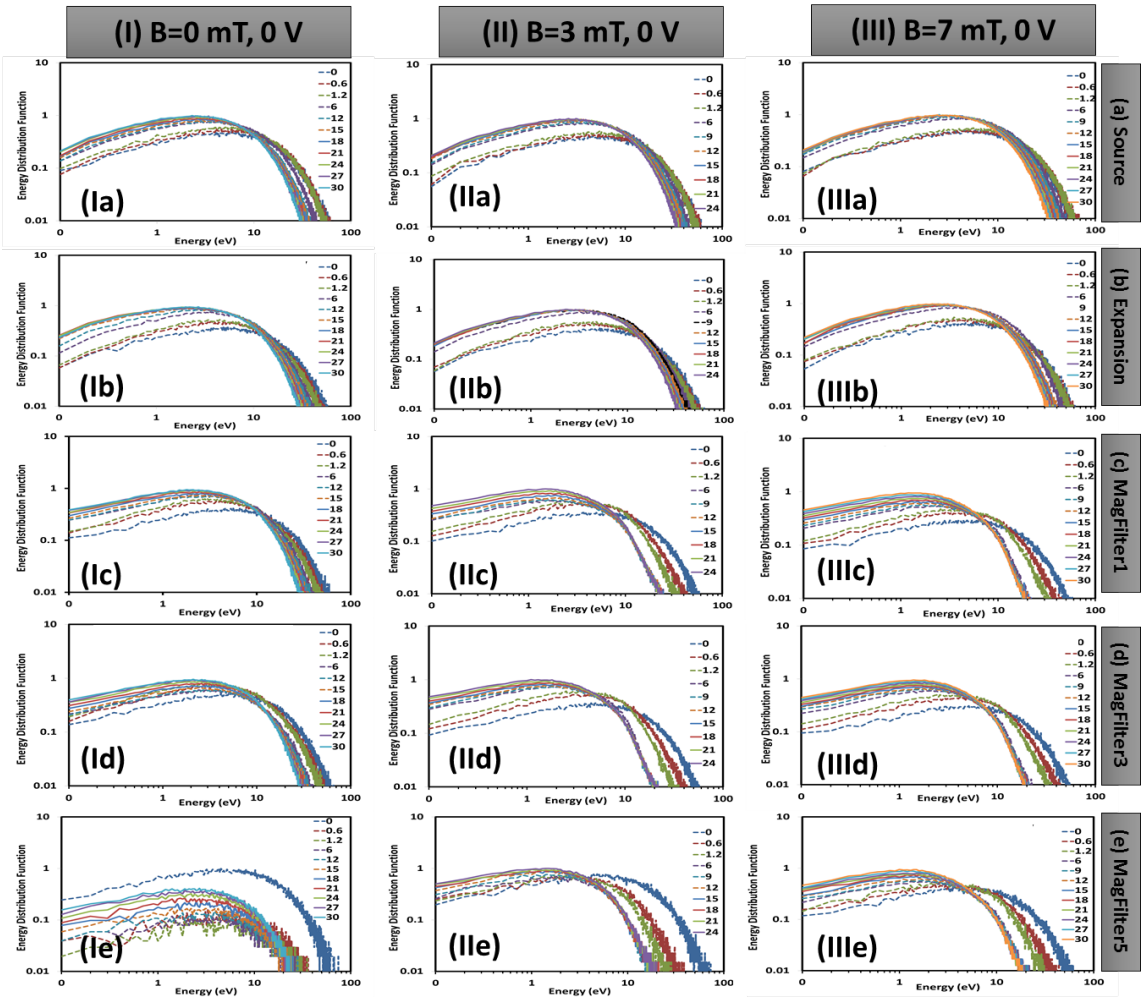

Figure 7.4: Temporal evolution of electron distribution function (EEDF) in case of three different magnetic fields: (I) 0 mT, (II) 3 mT, and (III) 7 mT. EEDFs are for different times: 0 μs, 0.6 μs, 1.2 μs, 6 μs, 12 μs, 15 μs, 18 μs, 21 μs, 24 μs, 27 μs, and 30 μs. Temporal evolution are done on different regions of the simulation domain. Different domains are (a) source (0.10 m to 0.12 m),(b) expansion (0.20 m to 0.22 m),(c) MagFilter1 (0.38 m to 0.40 m),(d) MagFilter3 (0.45 m to 0.47 m), and (e) MagFilter5 (0.51 m to 0.52 m).

7.4 Spatio-temporal evolution of IEDFs

Effect of magnetic field on IEDF with fixed 0 V bias

Temporal evolution of ion EDFs (IEDFs) are shown in Fig. (7.5). PIC simulations start with Maxwellian IEDF, and as it evolves with time, it becomes non-Maxwellian or bi-Maxwellian, and the peak moves towards the high energy side. In source and expansion regions, IEDFs are nearly Maxwellian. But as one moves towards the extraction side (i.e. MagFilter1 - 0.38 m to 0.40 m, MagFilter3 - 0.45 m to 0.47 m, and MagFilter5 - 0.51 m to 0.52 m), IEDFs become bi-Maxwellian, and the width of IEDFs becomes wide.

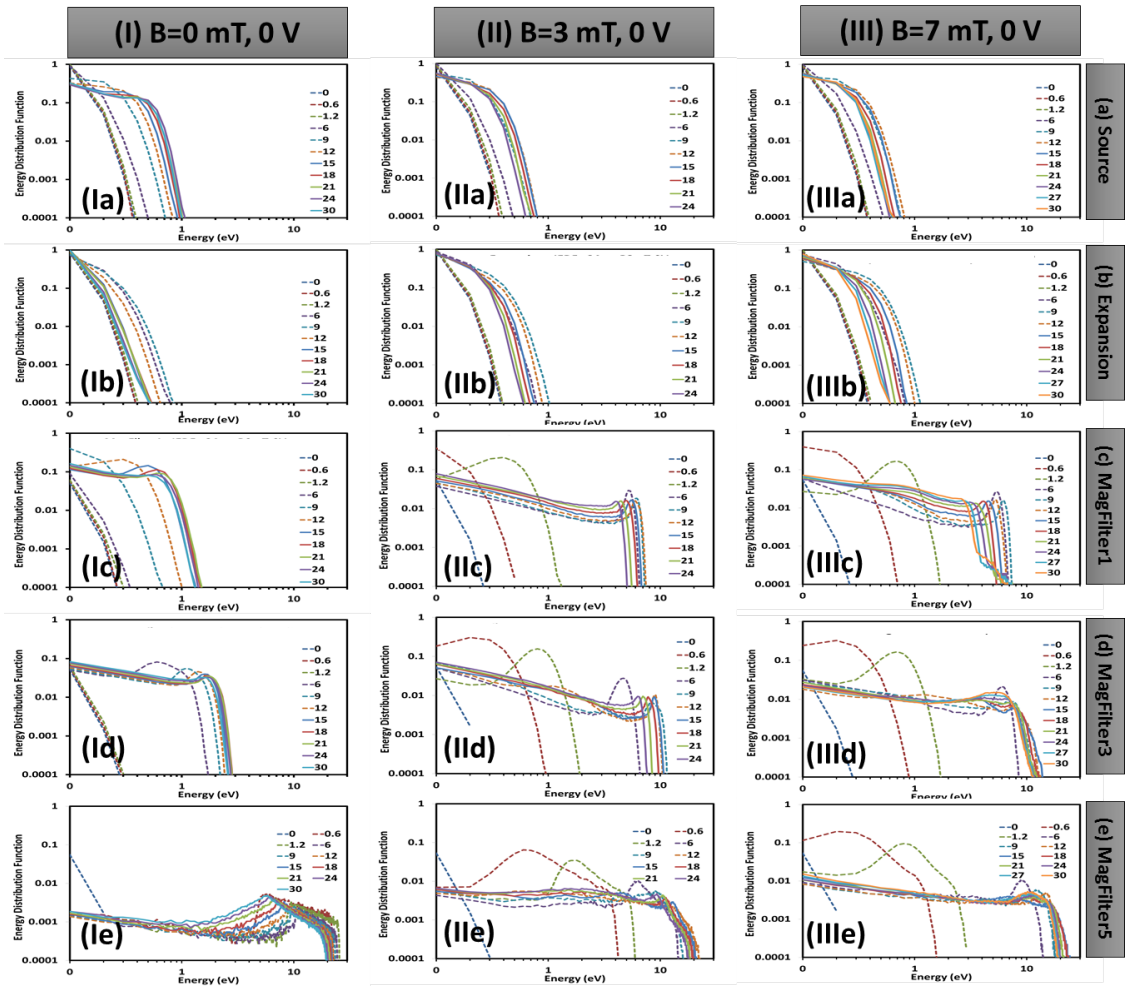

Figure 7.5: Temporal evolution of ion distribution function (IEDF) in case of three different magnetic fields: (I) 0 mT, (II) 3 mT, and (III) 7 mT. IEDFs are for different times: 0 s, 0.6 s, 1.2 s, 6 s, 12 s, 15 s, 18 s, 21 s, 24 s, 27s, and 30 s. Temporal evolution are done on different regions of the simulation domain. Different domains are (a) source (0.10 m to 0.12 m), (b) expansion (0.20 m to 0.22 m), (c) MagFilter1 (0.38 m to 0.40 m), (d) MagFilter3 (0.45 m to 0.47 m), and (e) MagFilter5 (0.51 m to 0.52 m).

IEDFs are the widest in the MagFilter5 region (the extraction boundary). Due to the sheath near the extraction boundary, ions get accelerated (gain high ion energy) due to the electric field generated by the difference between plasma potential and bias potential. Magnetic field significantly change IEDFs as shown in Fig. (7.5-IIc-e) and Fig. (7.5-IIIc-e). There are significant differences between cases without (case-I) and with magnetic fields (case-II and case-III). IEDFs become broader in case-IIc (Fig. (7.5-IIc)) and case-IIIc (Fig. (7.5-IIIc)) than case-Ic in Fig. (7.5-Ic). These changes are due to DL in the presence of the magnetic field as discussed in Chapter 6. Bi-Maxwellian IEDFs show two ion temperatures: one with cold ions and the second with accelerated ion due to

sheath or double layer. Similar to EEDFs, IEDFs also become stable after 6 μs in the case of magnetic fields.

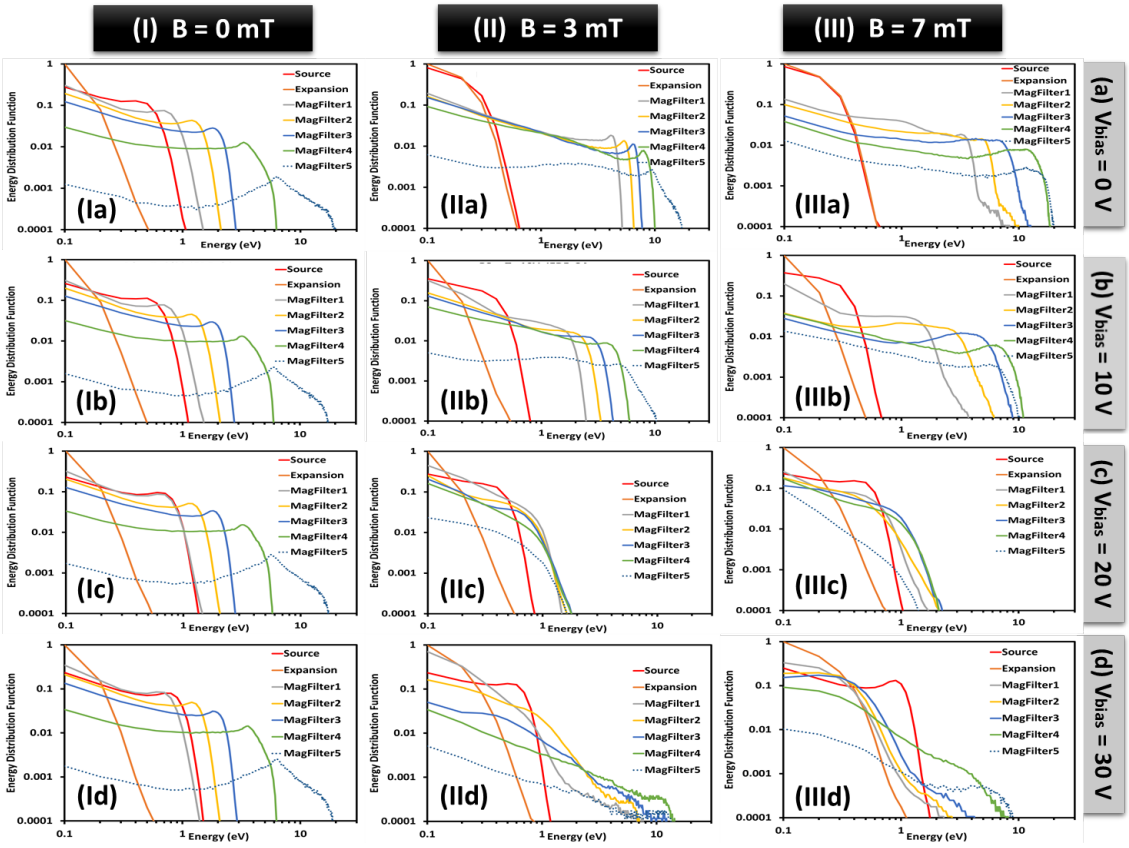

Figure 7.6: IEDFs for four different bias voltages ((a) 0 V, (b) 10 V, (c) 20 V, and (d) 30 V) and three different magnetic field ((I) 0 mT, (II) 3 mT, and (III) 7 mT).

Effect of bias voltage on IEDF

In all the cases presented above, with 0 V bias voltage at the extraction boundary, we find that EEDF does not changed much with time (as shown in Fig. (7.4)), but IEDFs change very rapidly (Fig. (7.5)). In Fig. (7.5), IEDFs have long tails, and second peaks are nearly at 10 eV, which is due to the sheath or DL. In these cases with 0 V bias, the bias voltage is lower than plasma potential and causes ion sheath, which accelerates ions [84]. However it is important to find what will happen in the absence of ion sheath. These can be achieved by changing bias potential. Therefore, a set of simulations with four different bias voltages are considered, (a) 0 V and (b) 10 V (bias voltage less than plasma potential), (c) 20 V (nearly same as plasma potential), and (d) 30 V (bias voltage more than plasma potential).

Fig. (7.6) shows IEDFs for four different bias voltages (0 V, 10 V, 20 V, and

30 V) and three different magnetic fields (0 mT, 3 mT, and 7 mT). In the cases with magnetic field (case-II and case-III), IEDFs become narrow as bias voltage increases from 0 V to 20 V (Fig. (7.6-IIa-c) and Fig. (7.6-IIIa-c)) and then become wider from 20 V to 30 V (Fig. (7.6-IIc-d) and Fig. (7.6-IIIc-d)). Without a magnetic field (0 mT), IEDFs do not change much with changing bias voltage (Fig. (7.6-I)). Contrary to the conventional perception, our simulations show that it is more important to investigate the IEDFs than EEDFs in such plasmas because IEDFs gradually become non-Maxwellian and are very sensitive to the magnitude of magnetic filter and bias voltage. The non-Maxwellian nature of the IEDFs can be attributed to the presence of instabilities and double layer formation.

7.5 Electron and ion phase space plots

In this section, electron and ion velocities are studied to understand why EDFs are Maxwellian for electrons and Bi-Maxwellian for ions. A more detailed explanation can be achieved by particle-phase velocities plots (the positions of a sample of electrons/ions in the (x, vx) phase space plane).

Electron phase velocities

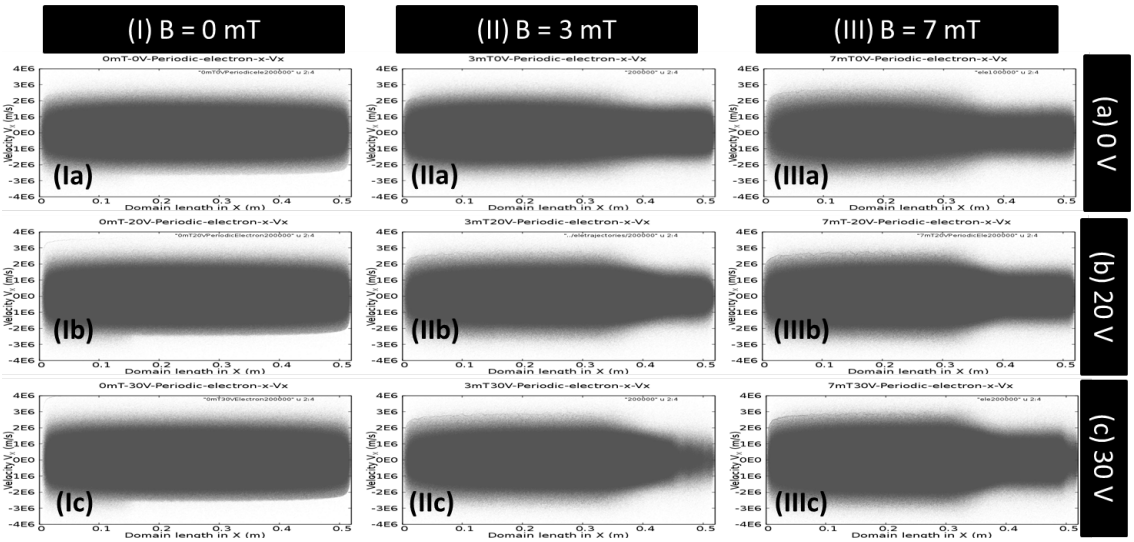

Figure 7.7: Electron velocities V_x in X-direction (m/s) Vs simulation domain length in X (m) for three different magnetic field ((I) 0 mT, (II) 3 mT, and (III) 7 mT) with three different bias voltages ((a) 0 V, (b) 20 V, and (c) 30 V) by using 2D-3V PIC-MCC simulations.

Fig. (7.7) and Fig. (7.8) show electron and ion velocities in X-direction (V_x). In

case-I (absence of magnetic field B = 0 mT), electron velocities are uniform as seen in Fig. (7.7-I). In case-II (B = 3 mT) and case-III (B = 7 mT), electrons lose energies (get decelerated) in the magnetic filter region due to more collisions with heavy ions and neutrals as seen by the narrow band in Fig. (7.7-II) and Fig. (7.7-III). One of the important observations is, electron velocities band is more narrow in case-IIc than in all other cases. It means that in case-IIc (B - 3 mT, 30 V bias), electrons lose more energies and get cooler near the extraction region. This investigation using particle-phase velocities, clearly shows that due to high collision frequencies, electron velocities become uniform and EEDF is Maxwellian.

Ion phase velocities

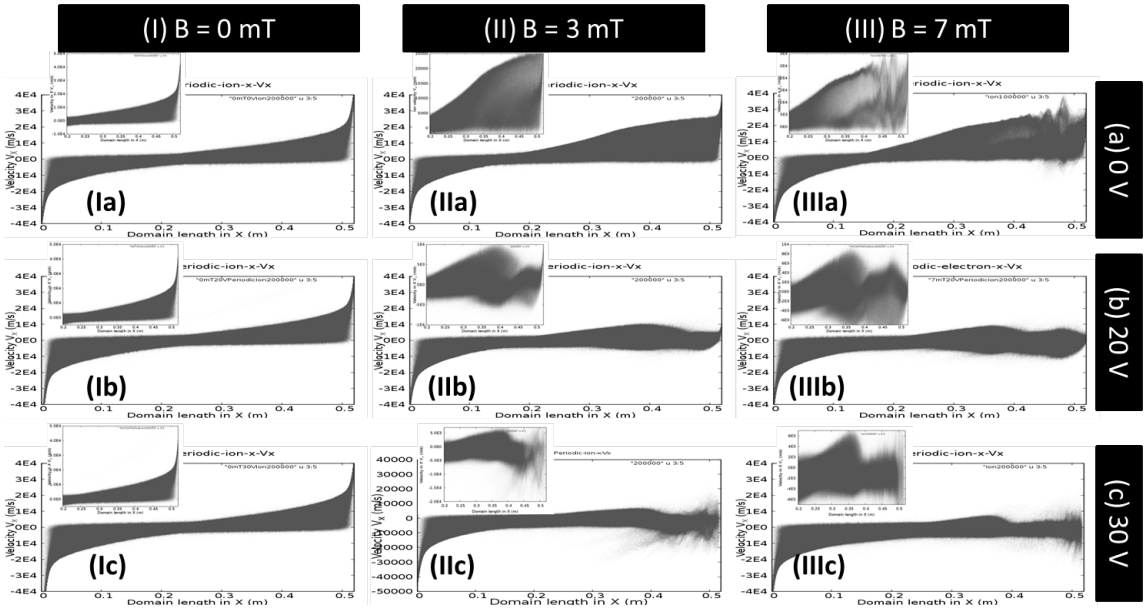

Figure 7.8: Ion velocities V_x in X-direction (m/s) Vs simulation domain length in X (m) for three different magnetic field ((I) 0 mT, (II) 3 mT, and (III) 7 mT) with three different bias voltages ((a) 0 V, (b) 20 V, and (c) 30 V) by using 2D-3V PIC-MCC simulations. Inlet plots are zoom plots from 0.2 m to 0.52 m.

Overall pattern of ion velocities as seen in Fig. (7.8) are very different compared to the electron particle-phase velocities as seen in Fig. (7.7). Due to low collision frequencies, ions do not lose energy rapidly. IEDFs are sensitive to the changes in input parameters in experiments. There is a sharp rise in ion velocities in X-direction near the source boundary in all cases with and without magnetic fields. Source boundary is kept at 0 V, therefore the sharp potential drop (difference of plasma potential and voltage on source boundary) is being observed near the source boundary, that accelerates ions towards

source boundary. Similarly, ion accelerations towards +X-direction are visible in case-I (a, b,and c) (Fig. (7.8-I)), case-IIa (Fig. (7.8-IIa)), and case-IIIa (Fig. (7.8-IIIa)). In case-IIa and case-IIIa (Fig. (7.8-IIa) and 7.8-IIIa)), the rise in ion acceleration starts with the initial rise of the Gaussian shape magnetic field. Split in ion accelerations are visible in inlet plot of Fig. (7.8). These sharp rise and splitting in ion velocities are due to DL as discussed in Chapter 6 section 6.4. In case with 20 V and 30 V bias, ions are decelerated as shown in Fig. (7.8-IIb-c) and Fig. (7.8-IIIb-c).

7.6 Conclusions

In this chapter, a detailed EDF based investigation using the 2D-3V PIC-MCC model has been presented. Simulations, considering periodic boundary conditions, has been conducted using background plasma (with electrons and ions) in the context of ROBIN negative ion source. Our analysis reveals that EEDF is Maxwellian, and IEDF is non-Maxwellian or bi-Maxwellian in nature. EEDFs become narrow with time, in the case of the magnetic filter field, due to electrons losing energies due to collisions. High collision frequencies help electrons to lose more energy, and EEDFs remain Maxwellian. Electron loses energies in the magnetic filter region as shown by a narrow band in the case with the magnetic field (case-II and case-III in Fig. (7.7)).

In source and expansion regions, IEDFs are nearly Maxwellian. But in the magnetic field regions, IEDFs become non-Maxwellian or bi-Maxwellian. In the absence of a magnetic field, IEDFs are also non-Maxwellian or bi-Maxwellian due to sheath effects that are nearly similar to cases with the magnetic field. Considering the case of 0 V bias, the second peak of IEDFs varies from 1 eV to 3 eV in MagFilter1 and MagFilter3 regions. The second peak of IEDF is at 10 eV near the extraction region. Ions got accelerated due to sharp potential gradients near boundaries. In the case of the magnetic field, the second peak of IEDF varies from 8 eV to 11 eV in the magnetic filter region (MagFilter1, MagFilter3, and MagFilter5). Ions get accelerated at the start of the magnetic filter region. Acceleration is due to double layers or instabilities. Bias voltage strongly affects the IEDFs. IEDF tends to become

Maxwellian as bias potential goes near the plasma potential. IEDF has a wide tail if the difference between bias potential and plasma potential increases. High potential difference generates an electric field that accelerates ions. Ion velocities in X-direction shows two kinds of velocities. Ions accelerate in the -X direction near-source boundary, whereas ions accelerate in +X direction near extraction boundary. The splitting of ion velocities, observed in some specific cases, is due to double-layer formation and it may also be attributed to resonance or instabilities. We can summarise that IEDF is more sensitive to the changes in input parameters compared to the EEDF. Due to high collision frequencies, electrons randomize energies uniformly all over the domain through collisions and keep EEDF Maxwellian. IEDF captures minor variations due to input parameters, drifts, instabilities etc. and in future investigations of LTP experiments with similar setup it would be interesting to conduct well though-out IEDF diagnostics which may reveal very interesting physics associated with plasma transport across magnetic field.

CHAPTER 8

Conclusion and future scope

8.1 Introduction

Plasma transport across a transverse magnetic field (known as, magnetic filter) due to diffusion mechanism in several low pressure, low temperature plasma (LTP) experiments in different contexts, have reported Bohm diffusion $\frac{1}{B}$ or anomalous diffusion instead of classical $\frac{1}{B^2}$ diffusion. In low pressure low temperature plasma, the plasma transport through Bohm diffusion or anomalous diffusion is significantly larger than that of classical one. It is argued that different plasma drifts and micro-instabilities are responsible for enhanced transport.

This thesis is aimed at understanding the physics of anomalous transport of the background plasma in the presence of magnetic filter using a PIC-MCC based kinetic approach. The investigations performed in this thesis are inspired by the RF driver based negative ion source (ROBIN) phase I experiments. One of the major contributions of the work is the development of a 2D PIC-MCC model, its parallel implementation on high performance computing (HPC) systems and finally validation against experimental observations using real experimental parameters as inputs in the computer model. Unlike most of the previous works in this area, our 2D simulations have been performed considering real ion source dimensions and also by following all the strict numerical constraints recommended by Garrigues et. al. [66] leading to a desirable accuracy. Although it increased the computational cost but it helped in gaining confidence towards performing a direct comparison with experimental observations.

The thesis presents a detailed computational characterization of plasma transport across magnetic filter suitable for a negative ion source, ROBIN. The FFT analysis of plasma parameters estimated by the PIC-MCC model helped in the identification of two kinds of instabilities at different frequencies. A comprehensive study with different magnetic fields and bias voltages aided in establishing the parameter space when these instabilities can play a significant role on plasma transport. To the best of our knowledge, for the first time, we report about the ion acceleration due to the presence of potential gradient, in the form of a double layer generated self-consistently due to the electron-ion charge separation in the magnetic filter and sheath region at some specific values of magnetic field and bias voltage. Charge separation takes place due to the fact that electrons are magnetized but ions are unmagnetized. Simulation shows that instabilities and double layers play an important role in the spatio-temporal evolution of energy distribution functions (EDFs) of electrons and ions. EDF analysis from particle data shows electron energy distribution function (EEDF) is Maxwellian in nature however ion energy distribution function (IEDF) is non-Maxwellian or bi-Maxwellian in some conditions. Results show that, contrary to conventional expectation, IEDF is more sensitive to changes in input conditions such as different B-field profiles and bias voltages. This highlights that ion kinetics study is very important to understand the overall physics of plasma transport across the magnetic filter. Several case-studies presented in the thesis shows that magnetic filter field configuration significantly affects the plasma cross-field diffusion. The study of changing B-field configuration such as changing Gaussian width, the magnitude of B-field, and the peak of Gaussian field, give switching mechanism to the plasma profiles in the negative ion source. The flexible magnetic field profile can be realized in those negative ion sources where filter filed is created by passing strong current through plasma grid (TWIN ion source [8], BATMAN-U ion source [80], ELISE ion source [79], INTF ion source [139], SPIDER ion source [106]).

8.2 Summary of main results and accomplishments of the thesis

- Development of PIC-MCC based kinetic numerical model and its implementation for a detailed analysis of plasma transport across the magnetic field in the context to the LTP based negative ion source (involving electrons and H_2^+ ions).
- Studies using 1D model, comparison with experiments and highlighting the necessity for a 2D model to accurately capture drifts and instabilities.
- Development of hybrid (thread as well as node level) parallel 2D-3V PIC-MCC code and its execution on HPC cluster for computationally expensive problems thereby reducing the simulation to two to three days instead of few weeks. This enabled to satisfy all the recently recommended numerical constraints such as use of small grid size in mm to resolve Debye length, small-time steps of the order of ns to capture all the important physical time scales and a large number of simulation particles (tens of millions).
- 2D simulation results validated with experimental data from ROBIN negative ion source using actual physical dimensions. Plasma profiles from the simulation show similar trends (quantitative as well as qualitative) as observed in experimental results (such as decrements in electron temperature and high plasma density in the magnetic filter region). Some strip structures observed in the plasma density, which points towards the presence of drifts or instabilities.
- FFT analysis of potential shows the presence of two types of instabilities in the background plasma in the magnetic filter region. One instability corresponding to 10^5 Hz is recognized as a E$\times$B drift instability.
- During analysis of plasma profiles, the sharp potential gradient is observed in the magnetic filter field region as well as high ion temperature is observed in phase space plots. Detail systematic investigation of plasma parameters shows the presence of a Double

Layer (DL) in the magnetic filter region, in cases with strong E×B field.

- A detailed spatial and temporal analysis of the energy distribution function (EDF) performed for different cases. Maxwellian electron energy distribution function (EEDF) and bi-Maxwellian or non-Maxwellian ion energy distribution function (IEDF) have been observed. High collision frequencies of electrons are responsible for the Maxwellian nature of EEDF. Low collision frequencies of ions do not allow them to lose energy faster. In addition, double layer influence the ion distribution. These are the probable reasons for non-Maxwellian or bi-Maxwellian IEDF. We find IEDF is much more sensitive than the EEDF with changes in input physical parameters (such as magnetic field and bias potential) of the LTP source. However, more investigations is need to understand IEDF behaviour.

- Validation of PIC-MCC model with ROBIN experimental results gives the confidence to perform different case studies and give feedbacks to the experimentalists. We have done case studies by changing magnetic field configuration (by changing position, peak, and width of the Gaussian shape magnetic filter). Our case studies show that under ROBIN experimental conditions [12], the lower magnetic field near the extraction side gives low electron temperature at the extraction region compared to higher magnetic field values. While comparing different Gaussian widths, the narrow width of the Gaussian magnetic filter reduces more electron temperature than the broader width. As the magnetic filter shifts towards the *driver* region, effective trapping results in lower electron temperature compared to the filter near the extraction region. From these different sets of case studies, we can conclude that the magnitude, the Gaussian width, and the position of the magnetic filter will play an important role in obtaining the desired plasma profiles for efficient negative ion production.

8.3 Utility of work

The work presented in this thesis concerns background plasma transport in the presence of a magnetic filter using 2D-3V PIC-MCC kinetic simulation. The effect of different bias voltage applied on a surface equivalent to plasma grid in a negative ion source and transverse magnetic filter field on the plasma transport are studied.

The model described in the thesis is to understand only background plasma transport across the magnetic field. This model has not considered negative ions plasma chemistry, complex geometry, and walls. Negative ion beam extraction is also not considered. The question comes, how this model helps in better understanding of the physics of the negative ion source. The survival length of negative ions is few cm due to different destruction processes [10, 51, 145]. The extracted negative ion current produced by volume processes is only a $\sim$ 10% to 20% of the total ion current; mostly ions originating from the surface produced negative ions near the extraction region when source is operated with caesium catalyst [145]. Negative ion chemistry without Cs does not affect much to the plasma profiles. Understanding background plasma (electrons and ions) with drifts and instabilities initially resolved many anomalous diffusion issues. One by one, introducing obstacles on plasma transports such as walls, negative ions, one can understand the individual effects. Therefore, the complex problem is split into a set of simple problems: 1) Understand background plasma transport without negative ions - analysis of drifts and instabilities, 2) introduce volume mode negative ions - understand plasma transport with negative ions and 3) introducing surface produced negative ions near the extraction region - understand briefly negative ion beam transport. The step-wise approach explains the physics of drifts and instabilities in a more streamlined way, such as the role of collisions of electrons and ions, sink and source for instabilities; how the instabilities propagates in the plasma; and the possibility of any resonance effect and its role on the evolution of the instabilities.

The second stage of introducing the negative hydrogen ion through volume processes can be done by coupling this 2D-3V PIC-MCC model with the

second model. Bandyopadhyay had developed a 3D Monte Carlo code for negative ion production by volume process and its transport. The plasma profiles from this 2D-3V PIC-MCC model can be used as input of the model given in [7, 10]. The second model developed by Bandyopadhyay has three different sections of codes; 1) neutral transport code, 2) negative hydrogen ion production code, and 3) negative hydrogen ion transport code. The density of vibrationally excited H_2 molecules and the spectrum of those excited H_2 molecules are estimated using the neutral transport code. The negative hydrogen ion production code calculates the production and distribution of H^- ion density. H^- ion trajectories inside the source and H^- ion surviving probabilities are calculated in the negative hydrogen ion transport code. Experimental data on electron density n_e, electron temperature T_e, gas temperature T_g, and pressure profiles are used as inputs in the second model. If the outputs in terms of all these above plasma parameters from the present 2D-3V PIC-MCC model are given as input to the second model, a *self-consistent* integrated model can be developed for negative ion source.

8.4 Future scope

- **Extension of PIC-MCC model**: More detailed hydrogen chemistry and complex geometry of the source with walls (non-periodic boundaries) needs to be introduced in the model to acquire more accurate simulation results.

- **With negative ions**: The thesis considers background plasma with only electrons and positive ions. The extraction of the negative ions from the negative ion source and effects of instabilities in the plasma on the beam can be studied only when the negative ions are also introduced in the model to study the plasma transport across transverse magnetic filter field inside the ion source.

- **Identification of 10^6 Hz instability**: The FFT analysis shows the presence of two instabilities $10^5 Hz$ and $10^6 Hz$. We have recognized $10^5 Hz$ instability as E×B instability. Instability associated with $10^6 Hz$ needs further investigations. The role of the source walls and of the

instability/turbulence in the deconfinement of electrons needs to be investigated further.

- **Identification of resonant event**: During the study of plasma parameters, in some conditions, we have found amplification in plasma parameters associated with some particular frequencies. Such amplification indicates resonant events with those particular frequencies. This needs more investigations.
- **3D PIC-MCC model**: The study can be extended to more detailed simulations using 3D models with real 3D magnetic field topology. However, this is only possible with better state of the art powerful supercomputing facilities. 3D simulation for transverse magnetic filter effect and wall effect (plasma sheath, secondary electron, desorption, surface production of negative ions etc.) taking account of the large scale and non-local topology of the magnetic field line. 3D analysis of the EEDF in the 3D real geometry and real magnetic field configuration

List of Publications

Journal:

1. Miral Shah, Bhaskar Chaudhury, Mainak Bandyopadhyay, Arun Chakraborty, Computational characterization of plasma transport across magnetic filter in ROBIN using PIC-MCC simulation, *Fusion Engineering and design*, vol. 151, page no- 111402, 2020.

To be submitted

2. Miral Shah, Bhaskar Chaudhury, Mainak Bandyopadhyay, Arun Chakraborty, Observation of double layers near magnetic filter region in negative ion sources and its role in ion acceleration.
3. Miral Shah, Bhaskar Chaudhury, Mainak Bandyopadhyay, Arun Chakraborty, Investigation of Spatial and Temporal evolution of Energy Distribution Functions and its role in the plasma transport across magnetic filter in negative ion sources.

Book Chapters/ Conference Proceedings:

1. Miral Shah, Bhaskar Chaudhury, Mainak Bandyopadhyay, Arun Chakraborty. 1D-3v PIC-MCC Based Modeling and Simulation of Magnetized Low-Temperature Plasmas. Proceedings of the Sixth International Conference on Mathematics and Computing. *Advances in Intelligent Systems and Computing*, vol 1262. Springer, Singapore,2021.
2. Bhaskar Chaudhury , Mihir Shah, Unnati Parekh, Hasnain Gandhi, Paramjeet Desai, Keval Shah, Anusha Phadnis, Miral Shah, Mainak Bandyopadhyay, Arun Chakraborty, Hybrid Parallelization of Particle in Cell Monte Carlo Collision (PIC-MCC) algorithm for simulation of Low temperature Plasmas, Software Challenges to Exascale Computing (SCEC 2018), *Communications in Computer and Information Science*, Springer, Singapore, vol. 964, page no – 32, 13-14 Dec, 2018.

Full length conference papers:

1. Miral Shah, Bhaskar Chaudhury, Mainak Bandyopadhyay, Arun Chakraborty, 2D-3V PIC-MCC based simulations of plasma transport across magnetic filter: Instabilities

and double layer formation, *36th National Symposium on Plasma Science & Technology (PLASMA 2021)*, BIT Mesra, Jaipur Campus, Rajasthan, page no-288, 13-15 Dec., 2021.

2. Miral Shah, Bhaskar Chaudhury, Mainak Bandyopadhyay, Arun Chakraborty, The feasibility of resonance induced instabilities in the magnetic filter region of low temperature plasma based negative ion sources, *American Institute of Physics (AIP) Proceeding*, The 7th International symposium on Negative Ions, Beams and Sources (NIBS'20), 01-11 Sept, 2020.
3. Harshil Shah, Siddharth Kamaria, Riddhesh Markandya, Miral Shah, Bhaskar Chaudhury, A novel implication of 2D3V PIC algorithm for Kepler GPU architectures, *Proceedings of 24th IEEE International conference of high performance computing, data, and analytics (HIPC-2017)*, India, page no-378, 18-21 Dec, 2017.

Abstracts:

1. Miral Shah, Bhaskar Chaudhury, Mainak Bandyopadhyay, Arun Chakraborty, Study of plasma transport across magnetic filter in low temperature plasmas using 2D-3v PIC-MCC kinetic model, in *4th Asia Pacific Conference on Plasma Physics*, South Korea, 26-31 Oct, 2020.
2. Miral Shah, Bhaskar Chaudhury, Mainak Bandyopadhyay, Arun Chakraborty, More realistic 2D-3v PIC-MCC kinetic model based plasma diffusion study across the magnetic filter, in *34th National Symposium on Plasma Science & Technology (PLASMA 2019)*, Chennai, India, 3-6 Dec, 2019.
3. Miral Shah, Bhaskar Chaudhury, Mainak Bandyopadhyay, Arun Chakraborty, 2D-3V PIC-MCC Simulation of Negative Ion Sources: Insights from Energy Distribution Functions, *12th International Conference on Plasma Science & Applications (ICPSA-2019)* , Lucknow, India, 11-14 Nov, 2019.
4. Bhaskar Chaudhury, Miral Shah, Mainak Bandyopadhyay, Arun Chakraborty, Quantifying Plasma transport in ROBIN negative ion source: PIC-MCC Simulations vs. Experiments, *72nd Annual Gaseous Electronics Conference (GEC 2019)* , The American Physical Society, Texas, 28 Oct–1 Nov, 2019.
5. Miral Shah, Bhaskar Chaudhury, Mainak Bandyopadhyay, Arun Chakraborty, Study of Plasma Transport across Magnetic field using 2D-3V PIC-MCC kinetic model, *7th PSSI-Plasma Scholars Colloquium (PSC-2019)*, Gandhinagar, page no- 28, 8-10 Aug, 2019.
6. Bhaskar Chaudhury, Miral Shah, Mainak Bandyopadhyay, Arun Chakraborty, 2D PIC-MCC simulations of plasma dynamics across magnetic field lines: application to ROBIN negative ion source, *71st Annual Gaseous Electronics Conference (GEC 2018)*, The American Physical Society, Portland, Oregon, 5-9 Nov, 2018.
7. Miral Shah, Bhaskar Chaudhury, Mainak Bandyopadhyay, Arun Chakraborty, 2D-3V PIC-MCC simulation based study of electron energy distribution function (EEDF) for

understanding plasma transport across magnetic filter, *33rd National symposium on Plasma science and technology (PLASMA2018)*, Delhi, India, page no – 366, 4-7 Dec, 2018.

8. Miral Shah, Bhaskar Chaudhury, Mainak Bandyopadhyay, Arun Chakraborty, Computational studies of Plasma transport across magnetic filter for ROBIN negative ion source using 1D and 2D-3V PIC-MCC simulations, *32nd National symposium on Plasma science* & *technology (PLASMA2017)*, IPR, Gandhinagar, India, page no – 126, 7-10 Nov, 2017.

9. Miral Shah, Bhaskar Chaudhury, Mainak Bandyopadhyay, Arun Chakraborty, Computational studies of plasma transport across magnetic filter for ROBIN negative ion sources using 1D PIC-MCC simulation, *31st National symposium on Plasma science* & *technology (PLASMA2016)*, Coimbatore, India, 6-9 Dec.

10. Keval Shah, Anusha Phadnis, Miral Shah, Bhaskar Chaudhury, Parallelization of the Particle-In-Cell Monte Carlo Collision (PIC-MCC) Algorithm for Plasma Simulation on Intel MIC Xeon Phi Architecture, *Proc. Int. Conf. High Perform. Comput. Networking, Storage Anal. (SC2017)*, Colorado, Denver, USA, vol. 23, no. 10, p. 2012, 2017., 2016.

References

[1] A. Aanesland, J. Bredin, P. Chabert, and V. Godyak. Electron energy distribution function and plasma parameters across magnetic filters. *Applied Physics Letters*, 100:1–4, 2012.

[2] A. Al-Jibouri, A. J. Holmes, and W. G. Graham. Comparison of plasma transport theory with measurements in a H- discharge. *Plasma Sources Science and Technology*, 5:401–411, 1996.

[3] M. Bacal. Volume Production of Hydrogen Negative Ions. *Nuclear Instruments and Methods in Physics Research*, B37/38:28–32, 1989.

[4] M. Bacal, A. M. Bruneteau, and M. Nachman. Negative ion production in hydrogen plasmas confined by a multicusp magnetic field. *Journal of Applied Physics*, 55:15–24, 1984.

[5] M. Bacal and M. Wada. Negative hydrogen ion production mechanisms. *Applied Physics Reviews*, 2:021305, 2015.

[6] M. Bacal and M. Wada. Negative ion source operation with deuterium. *Plasma Sources Sci. Technology*, 29(3):1–63, 2020.

[7] M. Bandyopadhyay. *Studies of an inductively coupled negative hydrogen ion radio frequency source through simulations and experiments Studies of an inductively coupled negative hydrogen ion radio frequency source through simulations and experiments*. PhD thesis, TECHNISCHE UNIVERSITÄT MÜNCHEN FAKULTÄT FÜR PHYSIK Max-Planck-Institut für Plasmaphysik, Garching, Germany, 2004.

[8] M. Bandyopadhyay, M. J. Singh, G. Bansal, A. Gahlaut, K. Pandya, K. G. Parmar, J. Soni, I. Ahmed, G. Roopesh, C. Rotti, S. Shah, A. Phukan, R. K. Yadav, and A. K. Chakraborty. Two-RF-driver-based negative ion source

for fusion R&D. *IEEE Transactions on Plasma Science*, 40(10):2767–2772, 2012.

[9] M. Bandyopadhyay, A. Tanga, H. D. Falter, P. Franzen, B. Heinemann, and D. Holtum. Analysis of plasma dynamics of a negative ion source based on probe measurements. *Journal of Applied Physics*, 96(8):4107–4113, 2004.

[10] M. Bandyopadhyay and R. Wilhelm. Simulation of negative hydrogen ion production and transport. *Review of Scientific Instruments*, 75(5):1720–1722, 2004.

[11] J. Y. Bang and C. W. Chung. Experimental investigation of the Boltzmann relation for a bi-Maxwellian distribution in inductively coupled plasmas. *Physics of Plasmas*, 16:093502, 2009.

[12] G. Bansal, A. Gahlaut, J. Soni, K. Pandya, K. G. Parmar, R. Pandey, M. Vuppugalla, B. Prajapati, A. Patel, H. Mistery, A. Chakraborty, M. Bandyopadhyay, M. J. Singh, A. Phukan, R. K. Yadav, and D. Parmar. Negative ion beam extraction in ROBIN. *Fusion Engineering and Design*, 88:778–782, 2013.

[13] G. Bansal, K. Pandya, M. Bandyopadhyay, A. Chakraborty, M. J. Singh, J. Soni, A. Gahlaut, and K. G. Parmar. Cesium delivery system for negative ion source at IPR. *AIP Conference Proceedings*, 1390:614–623, 2011.

[14] G. Bansal, K. Pandya, J. Soni, A. Gahlaut, H. Tyagi, M. Bandyopadhyay, R. K. Yadav, K. G. Parmar, M. Vuppugalla, H. Mistri, B. Prajapati, and A. Chakraborty. Plasma Characterization in RF based Negative Ion Source , ROBIN , at IPR. In *Asia Plasma and Fusion Association (APFA 2013)*, pages 1–29, Korea, 2013.

[15] K. H. Berkner, R. V. Pyle, and J. W. Stearns. Intense, Mixed-Energy Hydrogen Beams for CTR Injection. *Nuclear Fusion*, 15:249–254, 1975.

[16] C. K. Birdsall and L. Fellow. Particle-in-Cell charged-particle simulations, Plus Monte Carlo collision with neutral atom, PIC-MCC. *IEEE Transactions on Plasma Science*, 19(2):65–85, 1991.

[17] C. K. Birdsall and A. B. Langdon. *Plasma Physics via Computer simulations*. IOP Publishing Ltd., 1991.

[18] J. A. Bittencourt. *Fundamentals of Plasma Physics*. Springer-Verlag New York, springer edition, 2004.

[19] L. P. Block. DOUBLE LAYERS. In *Nobel Symposium on the Physics of the Hot plasma in the Magnetosphere*, Geophysical Institute in Kiruna, Sweden, 1975.

[20] L. P. Block. A Double Layer Review. *Astrophysics And Space Science*, 55:59–83, 1978.

[21] J. P. Boeuf. Rotating structures in low temperature magnetized plasmas—insight from particle simulations. *Frontiers in Physics*, 2(74):1–17, 2014.

[22] J.-P. Boeuf. Tutorial: Physics and modeling of Hall thrusters. *Journal of Applied Physics*, 121:011101, 2017.

[23] J. P. Boeuf, B. Chaudhury, and L. Garrigues. Physics of a magnetic filter for negative ion sources. I. Collisional transport across the filter in an ideal, 1D filter. *Physics of Plasmas*, 19:113509, 2012.

[24] J. P. Boeuf, J. Claustre, B. Chaudhury, and G. Fubiani. Physics of a magnetic filter for negative ion sources. II. E$\times$B drift through the filter in a real geometry. *Physics of Plasmas*, 19:113510, 2012.

[25] J. P. Boeuf, G. Fubiani, and L. Garrigues. Issues in the understanding of negative ion extraction for fusion. *Plasma Sources Science and Technology*, 25, 2016.

[26] J. P. Boeuf and L. Garrigues. E$\times$B electron drift instability in Hall thrusters: Particle-in-cell simulations vs. theory. *Physics of Plasmas*, 25:061204, 2018.

[27] J. P. Boeuf, G. J. M. Hagelaar, P. Sarraillh, G. Fubiani, and N. Kohen. Model of an inductively coupled negative ion source: II. Application to an ITER type source. *Plasma Sources Science and Technology*, 20:015001, 2011.

[28] J. P. Boris. Relativistic Plasma Simulation—Optimization of a Hybrid Code. In *Proceedings of the conference on the Numerical Solution of Plasmas (4th)*, page 3, Naval Research Laboratory, Washington, D. C., 1971.

[29] K. Bowers. Accelerating a particle-in-cell simulation using a hybrid counting sort. *Journal of Computational Physics*, 173, 2001.

[30] W. B. Bridges, A. N. Chester, A. S. Halsted, and J. V. Parker. Ion Laser Plasmas. *Proceedings of the IEEE*, 59(5):724–737, 1971.

[31] J. D. Callen. *Fundamental of plasma physics*. M.I.T., Cambridge, MA, 1967.

[32] M. Capitelli and C. Gorse. Open problems in the physics of volume H-/D- sources. *IEEE Transactions on Plasma Science*, 33(6):1832–1844, 2005.

[33] E. Carbone, W. Graef, G. Hagelaar, D. Boer, M. M. Hopkins, J. C. Stephens, B. T. Yee, S. Pancheshnyi, J. Van Dijk, and L. Pitchford. Data needs for modeling low-temperature non-equilibrium plasmas: The LXCat project, history, perspectives and a tutorial. *Atoms*, 9(16):1–40, 2021.

[34] C. Chan, M. H. Cho, N. Hershkowitz, and T. Intrator. Laboratory Evidence for Ion-Acoustic-Type Double Layers. *Physical Review Letters*, 52(20):1782, 1984.

[35] C. Charles. A review of recent laboratory double layer experiments. *Plasma Sources Science and Technology*, 16:R1–R25, 2007.

[36] B. Chaudhury, M. Shah, U. Parekh, H. Gandhi, P. Desai, K. Shah, A. Phadnis, M. Shah, M. Bandyopadhyay, and A. Chakraborty. Hybrid Parallelization of Particle in Cell Monte Carlo Collision (PIC-MCC) Algorithm for Simulation of Low Temperature Plasmas. In *Communications in Computer and Information Science book series*, pages 32–53. Springer, Singapore, 2018.

[37] F. F. Chen. *Introduction to plasma physics and controlled fusion*. A Division of Plenum Publishing Corporation, 1984.

[38] J. Claustre, B. Chaudhury, G. Fubiani, M. Paulin, and J. P. Boeuf. Particle-in-cell monte carlo collision model on GPU-application to a low-temperature magnetized plasma. *IEEE Transactions on Plasma Science*, 41(2):391–399, 2013.

[39] P. Coakley, N. Hershkowitz, R. Hubbard, and G. Joyce. Experimental observations of strong double layers. *Physical Review Letters*, 40(4):230–233, 1978.

[40] D. Curreli and F. F. Chen. Cross-field diffusion in low-temperature plasma discharges of finite length. *Plasma Sources Science and Technology*, 23:064001, 2014.

[41] B. K. Das, M. Bandyopadhyay, K. Patel, K. Pandya, H. Tyagi, R. Yadav, M. Bhuyan, J. Bhagora, A. Gahlaut, and A. Chakraborty. Time resolved analysis algorithm for ramped Langmuir probe to study temporal evolution of plasma parameters in ROBIN. *Fusion Engineering and Design*, 130:122–130, 2018.

[42] B. K. Das, P. Hazarika, M. Chakraborty, and M. Bandyopadhyay. Improvement of charged particles transport across a transverse magnetic filter field by electrostatic trapping of magnetized electrons. *Physics of Plasmas*, 21:072118, 2014.

[43] J. M. Dawson. Particle simulation of plasmas. *Reviews of Modern Physics*, 55(2):403–447, 1983.

[44] V. K. Decyk and T. V. Singh. Particle-in-Cell algorithms for emerging computer architectures. *Computer Physics Communications*, 185(3):708–719, 2014.

[45] J. Demouth. Kepler's SHUFFLE (SHFL): Tips and Tricks | GTC 2013.

[46] J. Derouillat, A. Beck, F. Pérez, T. Vinci, M. Chiaramello, A. Grassi, M. Flé, G. Bouchard, I. Plotnikov, N. Aunai, J. Dargent, C. Riconda, and M. Grech. SMILEI : A collaborative, open-source, multi-purpose particle-in-cell code for plasma simulation. *Computer Physics Communications*, 222:351–373, 2018.

[47] P. Devynck, M. Bacal, J. Bruneteau, F. Hillion, P. Devynck, M. Bacal, J. Bruneteau, and F. H. Spatial. Spatial variation of negative ion density in a volume H- ion source. *Revue de physique Appliquee*, 22(8):753–759, 1987.

[48] I. Djermanov, S. Kolev, S. Lishev, A. Shivarova, and T. Tsankov. Plasma behaviour affected by a magnetic filter. *Journal of Physics: Conference Series*, 63:012021, 2007.

[49] H. J. Doucet, W. D. Jones, and I. Aiexeff. Linear ion acoustic waves in a density gradient. *Physics of Fluids*, 17:1738–1743, 1974.

[50] M. T. Fang, D. A. Fraser, and J. E. Allen. The d.c. properties of an alkali plasma diode. *Journal of Physics D: Applied Physics*, 2(2):229–240, 1969.

[51] U. Fantz, H. Falter, P. Franzen, D. Wünderlich, M. Berger, A. Lorenz, W. Kraus, P. McNeely, R. Riedl, and E. Speth. Spectroscopy - A powerful diagnostic tool in source development. *Nuclear Fusion*, 46(6):1–15, 2006.

[52] U. Fantz, P. Franzen, W. Kraus, M. Berger, S. Christ-Koch, M. Fröschle, R. Gutser, B. Heinemann, C. Martens, P. McNeely, R. Riedl, E. Speth, and D. Wünderlich. Negative ion RF sources for ITER NBI: status of the development and recent achievements. *Plasma Physics and Controlled Fusion*, 49:B563–B580, 2007.

[53] U. Fantz, P. Franzen, W. Kraus, H. D. Falter, M. Berger, S. Christ-Koch, M. Fröschle, R. Gutser, B. Heinemann, C. Martens, P. McNeely, R. Riedl, E. Speth, and D. Wünderlich. Low pressure and high power rf sources for negative hydrogen ions for fusion applications (ITER neutral beam injection) (invited). *Review of Scientific Instruments*, 79:02A511, 2008.

[54] U. Fantz, L. Schiesko, and D. Wünderlich. Plasma expansion across a transverse magnetic field in a negative hydrogen ion source for fusion. *Plasma Sources Science and Technology*, 23:044002, 2014.

[55] H. Fehske, R. Schneider, and A. Weibe. Computational Many-Particle Physics. In *Lecture Notes in Physics*, volume 739. Springer, Berlin Heodelberg, 2008.

[56] P. Franzen, H. Falter, U. Fantz, W. Kraus, M. Berger, S. Christ-Koch, M. Fröschle, R. Gutser, B. Heinemann, S. Hilbert, S. Leyer, C. Martens, P. McNeely, R. Riedl, E. Speth, and D. Wünderlich. Progress of the development of the IPP RF negative ion source for the ITER neutral beam system. *Nuclear Fusion*, 47:264–270, 2007.

[57] P. Franzen, R. Gutser, U. Fantz, W. Kraus, H. Falter, and M. Fr. Performance of multi-aperture grid extraction systems for an ITER-relevant RF-driven negative hydrogen ion source. *Nuclear Fusion*, 51:073035(13pp), 2011.

[58] G. Fubiani, R. Agnello, I. Furno, L. Garrigues, P. Guittienne, G. Hagelaar, A. Howling, R. Jacquier, B. Reman, A. Simonin, and F. Taccogna. Negative hydrogen ion dynamics inside the plasma volume of a linear device: Estimates from particle-in-cell calculations. *Physics of Plasmas*, 28:063503, 2021.

[59] G. Fubiani and J. P. Boeuf. Role of positive ions on the surface production of negative ions in a fusion plasma reactor type negative ion source - Insights from a 3D Particle-In-Cell Monte Carlo Collisions model. *Physics of Plasmas*, 20:113511, 2013.

[60] G. Fubiani and J. P. Boeuf. Plasma asymmetry due to the magnetic filter in fusion-type negative ion sources: Comparisons between two and three-dimensional particle-in-cell simulations. *Physics of Plasmas*, 21:073512, 2014.

[61] G. Fubiani, L. Garrigues, G. Hagelaar, N. Kohen, and J. P. Boeuf. Modeling of plasma transport and negative ion extraction in a magnetized radio-frequency plasma source. *New Journal of Physics*, 19:015002, 2017.

[62] G. Fubiani, G. J. M. Hagelaar, J. P. Boeuf, and S. Kolev. Modeling a high power fusion plasma reactor-type ion source: Applicability of particle methods. *Physics of Plasmas*, 19:043506, 2012.

[63] O. Fukumasa, H. Naitou, and S. Sakiyama. Control of reactive plasmas in a multicusp plasma source equipped with a movable magnetic filter.

Journal of Applied Physics, 74(2):848, 1993.

[64] O. Fukumasa and R. Nishida. Modelling of negative ion transport in caesium-seeded volume negative ion sources. *Nuclear Fusion*, 46(6):1–7, 2006.

[65] F. Gaboriau, R. Baude, and G. J. M. Hagelaar. Experimental evidence of the increased transport due to the wall bounded magnetic drift in low temperature plasma. *Applied Physics Letters*, 104:214107, 2014.

[66] L. Garrigues, G. Fubiani, and J. P. Boeuf. Appropriate use of the particle-in-cell method in low temperature plasmas: Application to the simulation of negative ion extraction. *Journal of Applied Physics*, 120:213303, 2016.

[67] R. Gobin, P. Auvray, M. Bacal, J. Breton, O. Delferrière, F. Harrault, A. A. Ivanov, P. Svarnas, and O. Tuske. Two approaches for H- ion production with 2.45 GHz ion sources. *Nuclear Fusion*, 46:S281–S286, 2006.

[68] D. M. Goebel and I. Katz. *Fundamentals of Electric Propulsion: Ion and Hall Thrustes*. Jet Propulsion Laboratory, 2008.

[69] E. W. Gonzalez Clua and M. P. Zamith. Programming in CUDA for Kepler and Maxwell Architecture. *Revista de Informática Teórica e Aplicada*, 22(2):233, 2015.

[70] F. A. Haas, L. M. Lea, and A. J. T. Holmes. A 'hydrodynamic' model of the negative-ion source. *Journal of Physics D: Applied Physics*, 24:1541–1550, 1991.

[71] G. J. M. Hagelaar, G. Fubiani, and J. P. Boeuf. Model of an inductively coupled negative ion source: I. General model description. *Plasma Sources Science and Technology*, 20:015001, 2011.

[72] G. J. M. Hagelaar and N. Oudini. Plasma transport across magnetic field lines in low-temperature plasma sources. *Plasma Physics and Controlled Fusion*, 53:124032, 2011.

[73] F. Hariri, T. M. Tran, A. Jocksch, E. Lanti, J. Progsch, P. Messmer, S. Brunner, C. Gheller, and L. Villard. A portable platform for accelerated

PIC codes and its application to GPUs using OpenACC. *Computer Physics Communications*, 207:69–82, 2016.

[74] A. Hatayama. Progress in modeling and numerical simulation of negative hydrogen ion sources (invited). *Review of Scientific Instruments*, 79:02B901, 2008.

[75] A. Hatayama, T. Matsumiya, T. Sakurabayashi, and M. Bacal. Particle-in-cell modeling of negative-ion transport and extraction processes in a hydrogen negative-ion source. *Review of Scientific Instruments*, 77:03A530, 2006.

[76] A. Hatayama, S. Nishioka, K. Nishida, S. Mattei, J. Lettry, K. Miyamoto, T. Shibata, M. Onai, S. Abe, S. Fujita, S. Yamada, and A. Fukano. Present status of numerical modeling of hydrogen negative ion source plasmas and its comparison with experiments: Japanese activities and their collaboration with experimental groups. *New Journal of Physics*, 20:065001, 2018.

[77] P. Hazarika, M. Chakraborty, B. K. Das, and M. Bandyopadhyay. A technique to control cross-field diffusion of plasma across a transverse magnetic field. *Physics of Plasmas*, 23:122105, 2016.

[78] J. He and Q. Zhang. Averaged collision strength of Carbon II ion of Druyvesteyn distribution in plasma. *Modern Physics Letters B*, 32(26):1–6, 2018.

[79] B. Heinemann, H. Falter, U. Fantz, P. Franzen, M. Fröschle, R. Gutser, W. Kraus, R. Nocentini, R. Riedl, E. Speth, A. Stäbler, D. Wünderlich, P. Agostinetti, and T. Jiang. Design of the "half-size" ITER neutral beam source for the test facility ELISE. *Fusion Engineering and Design*, 84:915–922, 2009.

[80] B. Heinemann, M. Fröschle, H. D. Falter, U. Fantz, P. Franzen, W. Kraus, R. Nocentini, R. Riedl, and B. Ruf. Upgrade of the BATMAN test facility for H - source development. *AIP Conference Proceedings*, 1655:060003, 2015.

[81] R. S. Hemsworth and T. Inoue. Positive and negative ion sources for magnetic fusion. *IEEE Transaction on Plasma Science*, 33(6):1799–1813, 2005.

[82] R. S. Hemsworth, A. Tanga, and V. Antoni. Status of the ITER neutral beam injection system (invited). *Review of Scientific Instruments*, 79:02C109, 2008.

[83] N. Hershkowitz. Review of Recent Laboratory Double Layer Experiments. *Space Science Reviews*, 41:351–391, 1985.

[84] N. Hershkowitz. Sheaths: More complicated than you think. *Physics of Plasmas*, 12:055502, 2005.

[85] R. W. Hockney and J. W. Eastwood. *Computer Simulation Using Particles*. IOP Publishing, 1988.

[86] Hoefler Torsten and Belli Roberto. Scientific benchmarking of parallel computing systems: twelve ways to tell the masses when reporting performance results. *Proceedings of the International Conference for High Performance Computing, Networking, Storage and Analysis*, page 73, 2015.

[87] A. J. Holmes. Electron flow through transverse magnetic fields in magnetic multipole arc discharges. *Review of Scientific Instruments*, 53:1517–1522, 1982.

[88] A. J. Holmes. A one-dimensional model of a negative ion source. *Plasma Sources Science and Technology*, 5(3):453–473, 1996.

[89] C. Huang and L. Li. Magnetic confinement fusion : a brief review. *Frontiers in Energy*, 12:305–313, 2018.

[90] J. D. Huba. *NRL Plasma Formulary*. Naval Research Laboratory, Washington, 2011.

[91] J. D. Huba and S. L. Ossakow. Physical mechanism of the lower-hybrid-drift instability in a collisional plasma. *Journal of Atmospheric and Terrestrial Physics*, 43(8):775–778, 1981.

[92] F. Iza, S. H. Lee, and J. K. Lee. *Computer modeling of low-temperature plasmas*, volume 661. Transworld Research Network (2007), 2007.

[93] C. Jacobsen and P. Carlqvist. Solar Flares Caused by Circuit Interruptions. *ICARUS*, 3(3):270–272, 1964.

[94] Justin Luitjens. Faster Parallel Reductions on Kepler, 2014.

[95] H. R. Kaufman, R. S. Robinson, and R. I. Seddon. End-Hall ion source. *Journal of Vacuum Science & Technology A: Vacuum, Surfaces, and Films*, 5(4):2081–2084, 1987.

[96] E. Kawamura, A. J. Lichtenberg, and M. A. Lieberman. Two-dimensional particle-in-cell simulations of transport in a magnetized electronegative plasma. *Journal of Applied Physics*, 108:103305, 2010.

[97] G. Knorr and C. K. Goertz. Existence and stability of strong potential double layers. *Astrophysics And Space Science*, 31:209–223, 1974.

[98] S. Kolev, G. J. Hagelaar, G. Fubiani, and J. P. Boeuf. Physics of a magnetic barrier in low-temperature bounded plasmas: Insight from particle-in-cell simulations. *Plasma Sources Science and Technology*, 21:025002, 2012.

[99] S. Kolev, G. J. M. Hagelaar, and J. P. Boeuf. Particle-in-cell with Monte Carlo collision modeling of the electron and negative hydrogen ion transport across a localized transverse magnetic field. *Physics of Plasmas*, 16:042318, 2009.

[100] S. Kolev, S. Lishev, A. Shivarova, K. Tarnev, and R. Wilhelm. Magnetic filter operation in hydrogen plasmas. *Plasma Physics and Controlled Fusion*, 49:1349–1369, 2007.

[101] S. Kuppel, D. Matsushita, A. Hatayama, and M. Bacal. Numerical analysis of electronegative plasma in the extraction region of negative hydrogen ion sources. *Journal of Applied Physics*, 109, 2011.

[102] I. Langmuir. The interaction of electron and positive ion space charges in cathode sheaths. *Physical Review*, 33, 1929.

[103] K. N. Leung, K. W. Ehlers, and M. Bacal. Extraction of volume-produced H- ions from a multicusp source. *Review of Scientific Instruments*, 54:56–61, 1983.

[104] M. Li, S. K. Dew, and M. J. Brett. Effects of electron distribution functions on the floating potential of particles in the plasma: thin plasma sheaths. *Journal of Physics D: Applied Physics*, 32:2056–2059, 1999.

[105] D. Lundin, U. Helmersson, S. Kirkpatrick, S. Rohde, and N. Brenning. Anomalous electron transport in high power impulse magnetron sputtering. *Plasma Sources Science and Technology*, 17:025007, 2008.

[106] D. Marcuzzi, M. D. Palma, M. Pavei, B. Heinemann, W. Kraus, and R. Riedl. Detailed design of the RF source for the 1 MV neutral beam test facility. *Fusion Engineering and Design*, 84:1253–1258, 2009.

[107] K. Miyamoto, S. Okuda, and A. Hatayama. Meniscus and beam halo formation in a tandem-type negative ion source with surface production. *Applied Physics Letters*, 100:233507, 2012.

[108] K. Miyamoto, S. Okuda, A. Hatayama, M. Hanada, and A. Kojima. Study of beam optics and beam halo by integrated modeling of negative ion beams from plasma meniscus formation to beam acceleration. *Applied Physics Letters*, 102:023512, 2013.

[109] S. Mochalskyy. *Modeling of the negative ion extraction from a hydrogen plasma source . Application to ITER Neutral Beam Injector*. PhD thesis, Laboratoire de Physique Des Gaz et Des Plasmas, 2011.

[110] S. Mochalskyy, U. Fantz, D. Wünderlich, and T. Minea. Comparison of ONIX simulation results with experimental data from the BATMAN testbed for the study of negative ion extraction. *Nuclear Fusion*, 56:106025, 2016.

[111] S. Mochalskyy, A. F. Lifschitz, and T. Minea. Extracted current saturation in negative ion sources. *Journal of Applied Physics*, 111:113303, 2012.

[112] S. Mochalskyy, D. Wünderlich, U. Fantz, P. Franzen, and T. Minea. Towards a realistic 3D simulation of the extraction region in ITER NBI relevant ion source. *Nuclear Fusion*, 55:033011, 2015.

[113] S. Mochalskyy, D. Wünderlich, B. Ruf, U. Fantz, P. Franzen, and T. Minea. On the meniscus formation and the negative hydrogen ion

extraction from ITER neutral beam injection relevant ion source. *Plasma Physics and Controlled Fusion*, 56:105001, 2014.

[114] A. Mohri, K. Narihara, Y. Tomita, T. Tsuzuki, Z. Kabeya, K. Akaishi, and A. Miyamara. High Power Ion-Irradiation Test for CTR First Walls. *Japanese Journal of Applied Physics*, 19, 1980.

[115] D. D. Monahan and M. M. Turner. Global models of electronegative discharges: Critical evaluation and practical recommendations. *Plasma Sources Science and Technology*, 17:045003, 2008.

[116] I. M. Montellano, D. Wünderlich, S. Mochalskyy, and U. Fantz. 3D-PIC Modelling of a low temperature plasma sheath with wall emission of negative particles and its application to NBI sources. *Journal of Physics D: Applied Physics*, 52, 2019.

[117] F. Mozer, U. California, M. Hudson, R. B. Torberrt, B. Parady, and J. Yetteau. Observations of Paired Electrostatic Shocks in the Polar Magnetosphere. *Physical Review Letters*, 38(6):292, 1977.

[118] K. Nanbu. Theory of cumulative small-angle collisions in plasmas. *Physical Review E*, 55(4):4642–4652, 1997.

[119] J. Ongena, R. Koch, R. Wolf, and H. Zohm. Magnetic-confinement fusion. *Nature Physics*, 12:398–410, 2016.

[120] A. Pandey, M. Bandyopadhyay, D. Sudhir, and A. Chakraborty. Performance evaluation of a permanent ring magnet based helicon plasma source for negative ion source research. *Review of Scientific Instruments*, 88:103509, 2017.

[121] K. Pandya, A. Gahlaut, R. K. Yadav, M. Bhuyan, M. Bandyopadhyay, B. K. Das, P. Bharathi, M. Vupugalla, K. G. Parmar, H. Tyagi, K. Patel, J. Bhagora, H. Mistri, B. Prajapati, R. Pandey, and A. K. Chakraborty. First results from negative ion beam extraction in ROBIN in surface mode. *AIP Conference Proceedings*, 1869:030009, 2017.

[122] C. G. Petra, O. Schenk, and M. Anitescu. Real-time stochastic optimization of complex energy systems on high-performance

computers. *IEEE Computing in Science & Engineering*, 16(5):32–42, 2014.

[123] C. G. Petra, O. Schenk, M. Lubin, and K. Gärtner. An augmented incomplete factorization approach for computing the Schur complement in stochastic optimization. *SIAM Journal on Scientific Computing*, 36(2):C139–C162, 2014.

[124] Phelps. http://www.lxcat.laplace.univ-tlse.fr.

[125] L. C. Pitchford, L. L. Alves, K. Bartschat, S. F. Biagi, M.-C. Bordage, I. Bray, C. E. Brion, M. J. Brunger, L. Campbell, A. Chachereau, B. Chaudhury, L. G. Christophorou, E. Carbone, N. A. Dyatko, C. M. Franck, D. V. Fursa, R. K. Gangwar, V. Guerra, P. Haefliger, G. J. M. Hagelaar, A. Hoesl, Y. Itikawa, I. V. Kochetov, R. P. McEachran, W. L. Morgan, A. P. Napartovich, V. Puech, M. Rabie, L. Sharma, R. Srivastava, A. D. Stauffer, J. Tennyson, Jonathande Urquijo, J. van Dijk, L. A. Viehland, M. C. Zammit, O. Zatsarinny, and S. Pancheshnyi. LXCat: an Open-Access, Web-Based Platform for Data Needed for Modeling Low Temperature Plasmas. *Plasma Processes and Polymers*, 14:1600098, 2017.

[126] M. A. Raadu. The Physics of Double Layers and Their Role in Astrophysics. *Physics Reports (Review section of Physics Letters)*, 178(2):25–97, 1989.

[127] R. Rabenseifner. Hybrid Parallel Programming on HPC Platforms. *Fifth European Workshop on OpenMP, EWOMP '03, Aachen, Germany, Sept. 22-26, 2003*, 2003.

[128] T. A. Santhosh Kumar, S. K. Mattoo, and R. Jha. Plasma diffusion across inhomogeneous magnetic fields. *Physics of Plasmas*, 9(7):2946, 2002.

[129] N. Sato, G. Popa, E. Märk, E. Mravlag, and R. Schrittwieser. Instability as a source for traveling ion waves. *Physics of Fluids*, 19(1):70, 1976.

[130] T. Sato and H. Okuda. Numerical simulation on Ion Acoustic Double layers. *Journal of Geophysical Research*, 86(A5):3357–3368, 1981.

[131] O. Schenk and K. Gartner. Solving unsymmetric sparse systems of linear equations with PARDISO. *Future Generation Computer Systems*, 20(3):475–487, 2004.

[132] L. Schiesko, P. McNeely, P. Franzen, U. Fantz, and the NNBI Team. Magnetic field dependence of the plasma properties in a negative hydrogen ion source for fusion. *Plasma Physics and Controlled Fusion*, 54:105002, 2012.

[133] H. Shah, S. Kamaria, R. Markandeya, M. Shah, and B. Chaudhury. A Novel Implementation of 2D-3V Particle-In-Cell (PIC) Algorithm for Kepler GPU Architecture. In *Proceedings of 24th International conference High Performance Computing, Data and Analytics (HIPC 2017)*, pages 1–10, 2017.

[134] K. Shah, A. Phadnis, M. Shah, and B. Chaudhury. Parallelization of the Particle-In-Cell Monte Carlo Collision (PIC-MCC) Algorithm for Plasma Simulation on Intel MIC Xeon Phi Architecture. In *proceedings of nternational Conference for High Performance Computing, Networking, Storage and Analysis (SC17)*. IEEE, 2017.

[135] M. Shah, B. Chaudhury, and M. Bandyopadhyay. 1D-3V PIC-MCC based modelling and simulation of magnetized low temperature plasmas. In *Proceedings of the Sixth International Conference on Mathematics and Computing, Advances in Intelligent Systems and Computing*, volume 1262, pages 407–418. Springer International Publishing, 2020.

[136] M. Shah, B. Chaudhury, M. Bandyopadhyay, and A. Chakraborty. The Feasibility of Resonance Induced Instabilities in the Magnetic Filter Region of Low Temperature Plasma Based Negative Ion Sources. *AIP Conference Proceedings*, 2373(Nibs 2020):080003, 2020.

[137] M. Shah, B. Chaudhury, M. Bandyopadhyay, and A. K. Chakraborty. Computational characteristics of plasma transport across magnetic filter in ROBIN using PIC-MCC simulation. *Fusion Engineering and Design*, 151:111402, 2020.

[138] M. Sharma, A. D. Patel, Z. Shaikh, N. Ramasubramanian, R. Ganesh,

P. K. Chattopadhayay, and Y. C. Saxena. Evidence for neutrals carrying ion-acoustic wave momentum in a partially ionized plasma. *Physics of Plasmas*, 27, 2020.

[139] M. J. Singh, M. Bandyopadhyay, C. Rotti, N. P. Singh, S. Shah, G. Bansal, A. Gahlaut, J. Soni, H. Lakdawala, H. Waghela, I. Ahmed, G. Roopesh, U. K. Baruah, and A. K. Chakraborty. An Indian test facility to characterise diagnostic neutral beam for ITER. *Fusion Engineering and Design*, 86(6-8):732–735, 2011.

[140] M. J. Singh, A. K. Chakraborty, M. Bandyopadhyay, J. Joshi, H. Patel, K. Pandya, S. Shah, A. Gahlaut, A. Yadav, D. Parmar, D. Sharma, D. Singh, H. Tyagi, K. Joshi, M. V. Nagaraju, M. Bhuyan, M. Patel, R. Yadav, S. Pillai, D. Boilson, J. Chareyre, B. Schunke, and C. Rotti. R&D status of the Indian test facility for ITER diagnostic neutral beam characterization. *Nuclear Fusion*, 59(9), 2019.

[141] N. Singh. Current-free double layers : A review Current-free double layers : A review. *Physics of Plasmas*, 18:122105, 2011.

[142] E. Sintorn and U. Assarsson. Fast parallel GPU-sorting using a hybrid algorithm. *Journal of Parallel and Distributed Computing*, 68(10):1381–1388, 2008.

[143] A. I. Smolyakov, O. Chapurin, W. Frias, O. Koshkarov, I. Romadanov, T. Tang, M. Umansky, Y. Raitses, I. D. Kaganovich, and V. P. Lakhin. Fluid theory and simulations of instabilities, turbulent transport and coherent structures in partially-magnetized plasmas of ExB discharges. *Plasma Physics and Controlled Fusion*, 59:014041, 2017.

[144] A. Sodani, R. Gramunt, J. Corbal, H.-S. Kim, K. Vinod, S. Chinthamani, S. Hutsell, R. Agarwal, and Y.-C. Liu. Knights landing: Second-generation intel xeon phi product. *Ieee micro*, 36(2):34–46, 2016.

[145] E. Speth, H. D. Falter, P. Franzen, U. Fantz, M. Bandyopadhyay, S. Christ, A. Encheva, M. Fröschle, D. Holtum, B. Heinemann, W. Kraus, A. Lorenz, C. Martens, P. McNeely, S. Obermayer, R. Riedl, R. Süss,

A. Tanga, R. Wilhelm, and D. Wünderlich. Overview of the RF source development programme at IPP Garching. *Nuclear Fusion*, 46:S220–S238, 2006.

[146] M. Surendra, D. B. Graves, and G. M. Jellum. Self-consistent model of a direct-current glow discharge: Treatment of fast electrons. *Physical Review A*, 41(2):1112, 1990.

[147] T. Tabata and T. Shirai. Analytic Cross Sections for Collisions of H+, H2+, H3+, H, H2, and H- With Hydrogen Molecules. *Atomic Data and Nuclear Data Tables*, 76:1–25, 2000.

[148] F. Taccogna, S. Longo, M. Capitelli, and R. Schneider. Negative-ion-source modeling: From expansion to extraction region. *IEEE Transactions on Plasma Science*, 36(4):1589–1599, 2008.

[149] F. Taccogna and P. Minelli. PIC modeling of negative ion sources for fusion. *New Journal of Physics*, 19:015012, 2017.

[150] F. Taccogna, P. Minelli, and Z. Asadi. Numerical studies of the ExB electron drift instability in Hall thrusters Numerical studies of the ExB electron drift instability in Hall thrusters. *Plasma Sources Sci. Technol.*, 28:064002, 2019.

[151] F. Taccogna, P. Minelli, S. Longo, M. Capitelli, and R. Schneider. Modeling of a negative ion source. III. Two-dimensional structure of the extraction region. *Physics of Plasmas*, 17:063502, 2010.

[152] F. Taccogna, R. Schneider, S. Longo, and M. Capitelli. Modeling of a negative ion source. I. Gas kinetics and dynamics in the expansion region. *Physics of Plasmas*, 14:073503, 2007.

[153] F. Taccogna, R. Schneider, S. Longo, and M. Capitelli. Modeling of a negative ion source. II. Plasma-gas coupling in the extraction region. *Physics of Plasmas*, 15:103502, 2008.

[154] K. Takahashi, C. Charles, R. W. Boswell, and T. Fujiwara. Electron energy distribution of a current-free double layer: Druyvesteyn theory and experiments. *Physical Review Letters*, 107:035002, 2011.

[155] H. Tawara, Y. Itikawa, H. Nishimura, and M. Yoshino. Cross Sections and Related Data for Electron Collisions with Hydrogen Molecules and Molecular Ions. *Journal of Physical Chemistry Ref. Data*, 19(3):617, 1990.

[156] D. Tskhakaya, K. Matyash, R. Schneider, and F. Taccogna. The particle-in-cell method. *Contributions to Plasma Physics*, 47(8-9):563–594, 2007.

[157] M. M. Turner, R. A. Doyle, and M. B. Hopkins. Measured and simulated electron energy distribution functions in a low-pressure radio frequency discharge in argon. *Applied Physics Letters*, 62(25):3247–3249, 1993.

[158] V. Vahedi and M. Surendra. A Monte Carlo collision model for the particle-in-cell method: applications to argon and oxygen discharges. *Computer Physics Communications*, 87:179–198, 1995.

[159] D. Wünderlich, S. Mochalskyy, U. Fantz, and P. Franzen. Modelling the ion source for ITER NBI: from the generation of negative hydrogen ions to their extraction. *Plasma Sources Science and Technology*, 23:015008, 2014.

[160] D. Wünderlich, S. Mochalskyy, I. M. Montellano, and A. Revel. Review of particle-in-cell modeling for the extraction region of large negative hydrogen ion sources for fusion. *Review of Scientific Instruments*, 89:052001, 2018.

[161] H. Xu, Z. ming Sheng, X. mu Kong, F. fang Su, H. Xu, Z. ming Sheng, X. mu Kong, and F. fang Su. Effects of ion motion on linear landau damping. *Physics of Plasmas*, 24:022101, 2017.

[162] R. Zorat and D. Vender. Global model for an rf hydrogen inductive plasma discharge in the deuterium negative ion source experiment including negative ions. *Journal of Physics D: Applied Physics*, 33:1728–1735, 2000.

[163] R. Zorat and D. Vender. Global model for an rf hydrogen inductive plasma discharge in the deuterium negative ion source experiment including negative ions. *Journal of Physics D: Applied Physics*, 33(14):1728–1735, 2000.